1
Molecular Units

1.1
Case Studies

Living beings are "open" systems whose sustained existence requires fluxes. Since even very simple open systems such as a candle flame or a water jet form their own shape and restore it after a disturbance, one may readily accept the idea that more complex open systems are able to form and sustain more complex structures in space and time. Apparently, there are open systems involving chemical reactions with a tendency toward the formation of substances and reaction cycles with increasing complexity, ending up in the formation of life. The molecular processes of life are usually confined to enclosed (but not closed) spaces, the cells and their internal compartments. Eukaryotic cells, which are discriminated from prokaryotic cells by the presence of a nucleus harboring the vast majority of genetic information, are equipped with a variety of such functionally defined compartments, collectively summarized as organelles (Figure 1.1). This type of confinement is realized by membranes shielding the interior and controlling the flow of substances, energy, and information in and out. The information flow is facilitated by the membranes' capability of signal detection and transduction. Structural flexibility of the plasma membrane is a necessary precondition for cell motility and division. The cell is filled with cytoplasm, an assembly of functional entities and filamentous networks immersed in an aqueous solution, the cytosol.

Since there are good reasons for the assumption that all organisms have descended from a hypothetical common progenitor, their relationship has the topology of a tree and hence is usually visualized as a graph known as the phylogenetic tree of life (Figure 1.2). One can be sure that the tree of life obtained with a particular advanced technique, as the one in Figure 1.2, does not much differ from the real one and thus can serve as a basis for considerations as if it were the real one. As seen in the figure, the tree of life consists of three major domains. The vast majority of organisms are unicellular. Multicellular species are only found in a few branches of the Eukaryota, which are distinguished by the presence of a nucleus containing most of the genetic information. Autotrophic and heterotrophic organisms are present in every major domain. These terms refer to the source of the energy-rich organic substances (nutrients) required to drive the metabolism.

Bio-Nanomaterials: Designing Materials Inspired by Nature, First Edition. Wolfgang Pompe, Gerhard Rödel, Hans-Jürgen Weiss, and Michael Mertig.

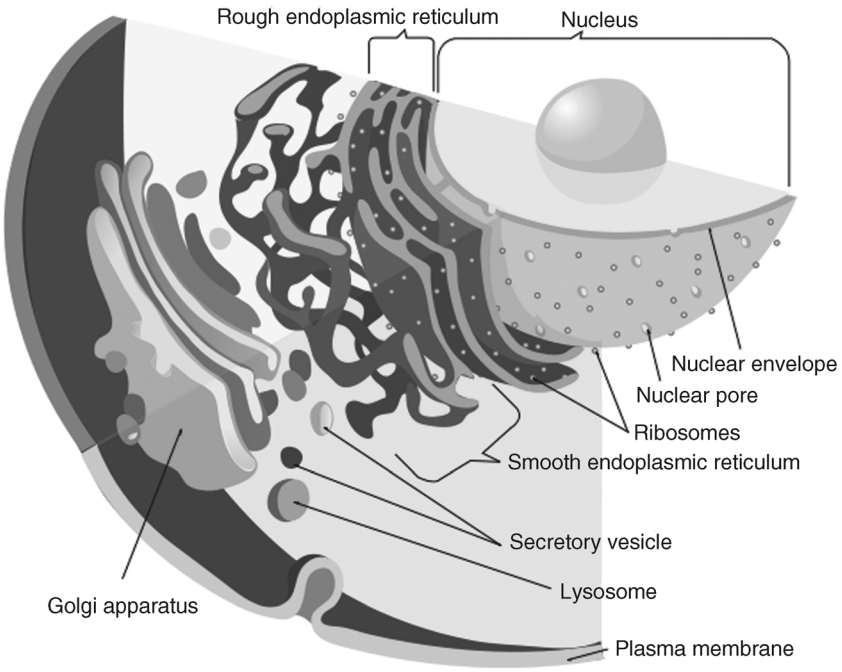

Figure 1.1 Eukaryotic cell structure with the endomembrane system. (*Source*: Wikimedia Commons; author Mariana Ruiz.)

Autotrophic organisms are able to produce the nutrients by themselves, starting from inorganic substances. In contrast, heterotrophic organisms are unable to synthesize their nutrients and hence have to acquire them by consuming organic substances. Besides the well-known photoautotrophy of plants, an alternative form of autotrophy, the so-called chemoautotrophy, is widespread among the Prokaryota. In the presence of oxygen, chemoautotrophic organisms make use of the energy released by oxidation, notably of inorganic substances, enabling them to live in extreme habitats such as salt lakes, hot springs, deep sea floors, and so on. This property makes chemoautotrophs interesting for bioengineering. Photoautotrophic cyanobacteria have recently been considered with respect to their suitability for biofuel production. Eukaryotes are especially valuable for biotechnology, bio-inspired materials development, and medical engineering. Fermentation by means of yeast, for example, has been applied for millennia. Recently, animal stem cells have been widely used in tissue engineering developments. The huge variety of organisms offers a wealth of objects with structures differing on the molecular level that may be suitable as building blocks in biotechnology and biologically inspired materials science. Today, we are still in a very early stage of exploring their potential. Our responsibility for the protection of life on Earth implies that progress in this field of research should always be complemented with adequate risk assessment.

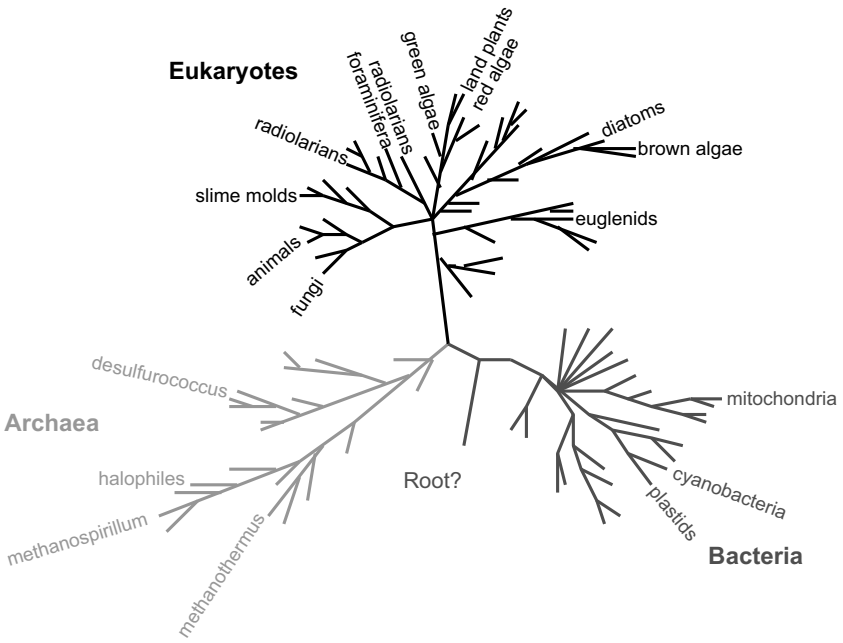

Figure 1.2 The phylogenetic tree of life based on the comparison of ribosomal RNA. (Bacteria and Archaea are also called Prokaryota. The names of most taxa are omitted here for simplicity.)

The sizes of the bimolecular structures investigated as potential building blocks range from molecular (0.2 nm) to cell size (0.1 mm) (Figure 1.3). Remarkably, organisms utilize only a small fraction of the chemical elements. Obviously, they are sufficient to form the large variety of organic compounds required for sustaining the processes of life. Let us consider the composition of the bacterium

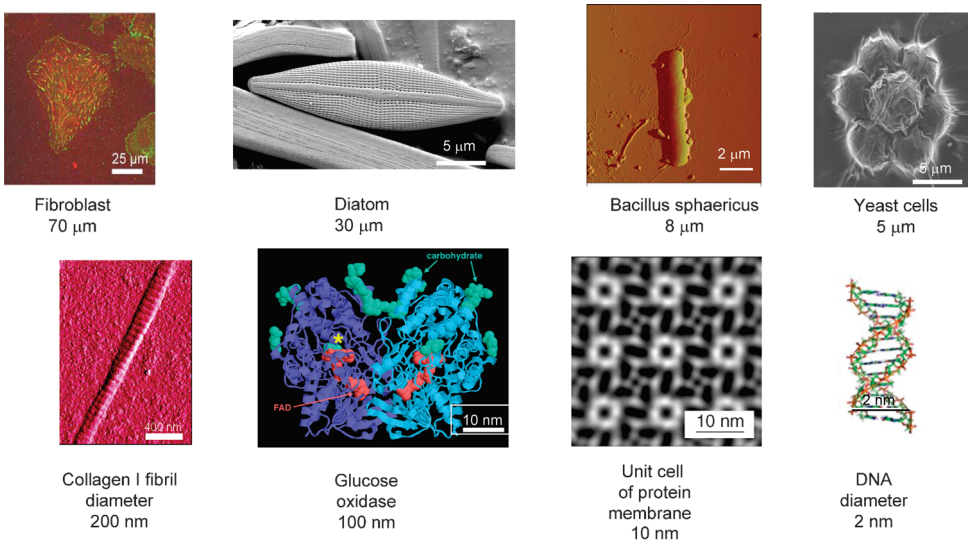

Figure 1.3 Size variation of biological components.

Table 1.1 Molecular composition of *E. coli* according to Nelson and Cox (2008).

	Percentage of total cellular weight	Approximate number of different molecular species
Water	70	1
Proteins	15	3000
Nucleic acids		
DNA	1	1–4
RNA	6	>3000
Polysaccharides	3	10
Lipids	2	20
Monomeric subunits and intermediates	2	500
Inorganic ions	1	20

Escherichia coli, with size is about 2 μm × 1 μm (Table 1.1). Its cytoplasm contains the nucleoid usually with one DNA chain, eventually a few small circular DNA molecules called plasmids, about 15 000 ribosomes (the sites of protein synthesis), 10 to several hundred copies of about 1000 different enzymes, about 1000 smaller organic compounds with a molecular weight less than 1000 (metabolites or coenzymes), and various inorganic ions. The cytoplasm is surrounded by the cell envelope, which consists of an outer and an inner membrane composed of lipid bilayers and peptidoglycans. Connected to the envelope are specific protein structures such as flagellae for cell propelling, pili providing adhesion sites, and surface layer proteins for mechanical stabilization and acting as filter and ion transport structures.

Eukaryotic cells with a size of about 5–100 μm show a higher structural complexity. The essential differences to bacteria are the presence of a nucleus, a number of membrane-enclosed organelles (e.g., mitochondria, endoplasmic reticulum, Golgi complexes, peroxisomes, and lysosomes), and the cytoskeleton, a highly structured network of protein filaments (microtubules, actin filaments, and intermediate filaments) organized by numerous proteins that regulate the assembling and disassembling of the various filaments. Characteristic components of plant cells are chloroplasts and vacuoles. A concise overview of the structure and properties of the main groups of biomolecules available for a bottom-up design of nanostructured materials – nucleic acids, proteins, carbohydrates, and lipids – is provided below.

1.1.1 Nucleic Acids

The storage, replication, and transfer of genetic information in living organisms is mediated by chain-like macromolecules called nucleic acids, the deoxyribonucleic acid (DNA) and several types of ribonucleic acid (RNA) (Figure 1.4).

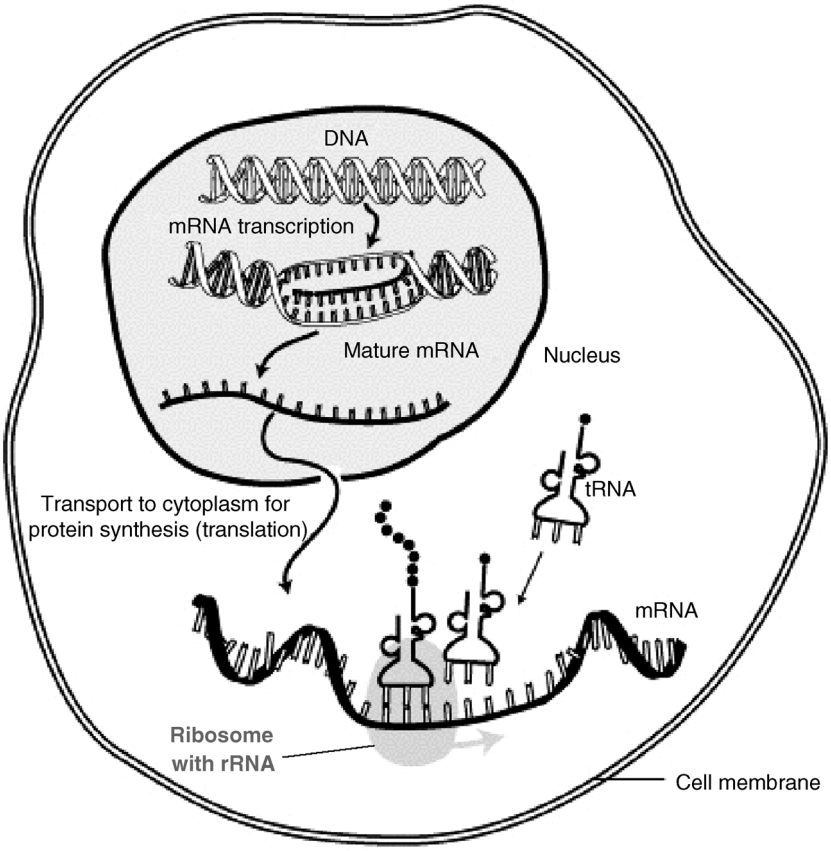

Figure 1.4 Functions of the three major types of RNA in protein synthesis: DNA serves as a template for the synthesis of messenger RNA. The respective genetic information can be translated into a specific sequence of amino acids by ribosomes that are composed of proteins and ribosomal RNA. The amino acids are provided by transfer RNA. (*Source*: Wikimedia Commons; author Sverdrup; http://www.genome.gov/Pages/Hyperion/DIR/VIP/Glossary/Illustration/mrna.shtml.)

The nucleotide sequence of the DNA encoding the genetic information is transcribed into messenger RNA (mRNA), which is released from the nucleus into the cytoplasm, where it associates with one of the ribosomes, the sites of protein synthesis. Groups of three bases of the nucleotide sequence of the mRNA serve as the codons for one of the 20 amino acids found in proteins. Transfer RNAs (tRNAs) are the carriers of the amino acids, which constitute the raw material for protein synthesis. Each tRNA carries at its 3′-end a particular amino acid that is incorporated in the growing polypeptide chain at a specific site of the ribosome, when a sequence of three bases (anticodon) of the tRNA is bound to the complementary sequence (codon). Every nucleotide of DNA and RNA consists of a phosphate group, a sugar group, and a nitrogen-containing base (Figure 1.5). Natural nucleic acid contains

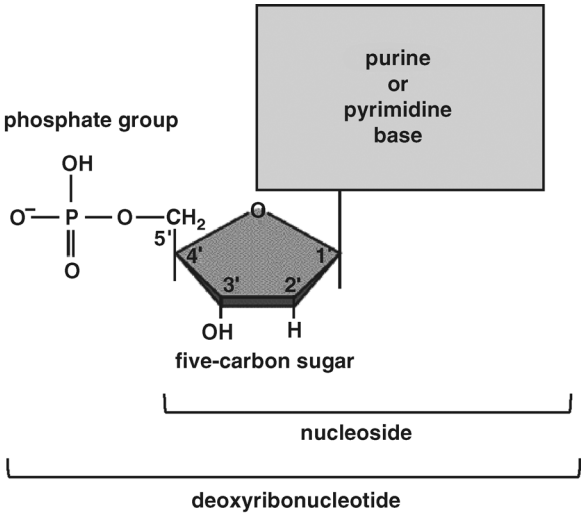

Figure 1.5 Structure of a deoxyribonucleotide. Ribonucleotides possess —OH instead of —H on the 2′-carbon of the pentose ring.

four different bases. The bases are derivatives of two compounds, purine and pyrimidine. The purine bases adenine (A) and guanine (G) and the pyrimidine base cytosine (C) are common to DNA and RNA. The pyrimidine base thymine (T) is only found in the DNA, and uracil (U) only in the RNA (Figure 1.6). The sugar units in a DNA are 2′-deoxy-D-ribose units, and in RNA D-ribose units (Figure 1.7).

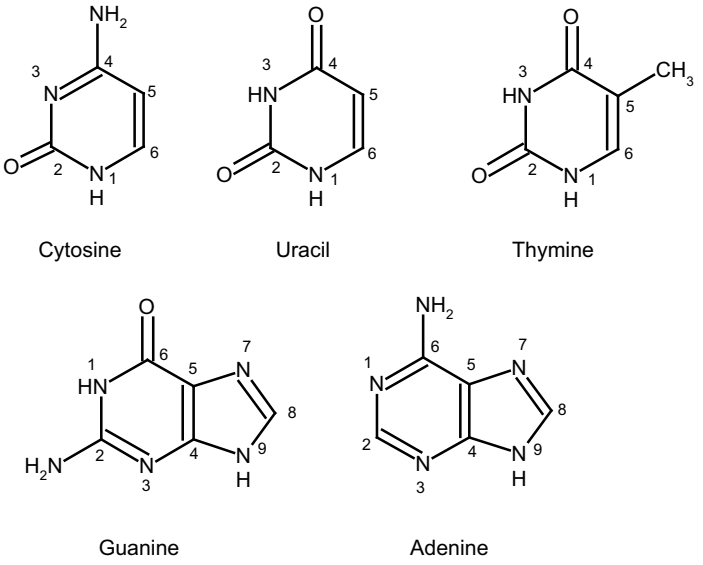

Figure 1.6 The structure-forming bases of DNA and RNA: pyrimidine bases (top) and purine bases (bottom).

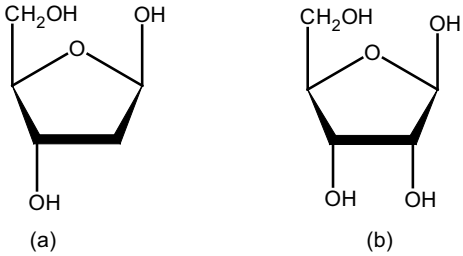

Figure 1.7 2′-Deoxy-D-ribose (a) and D-ribose (b) – the sugar building blocks in DNA and RNA, respectively.

The nucleotides of DNA and RNA are successively linked by phosphate group bridges. The phosphate groups connect the 5′-hydroxyl group of one pentose with the 3′-hydroxyl group of the pentose of the next nucleotide (Figure 1.8). The backbone of DNA and RNA consists of negatively charged phosphate and pentose residues. Like any charge, it polarizes the surrounding medium containing dipoles, such as water in this case. This is equivalent to an attraction of water by the DNA backbone; hence, it is hydrophilic. The purine and pyrimidine bases are nonpolar molecules, which implies hydrophobic behavior. In water, such

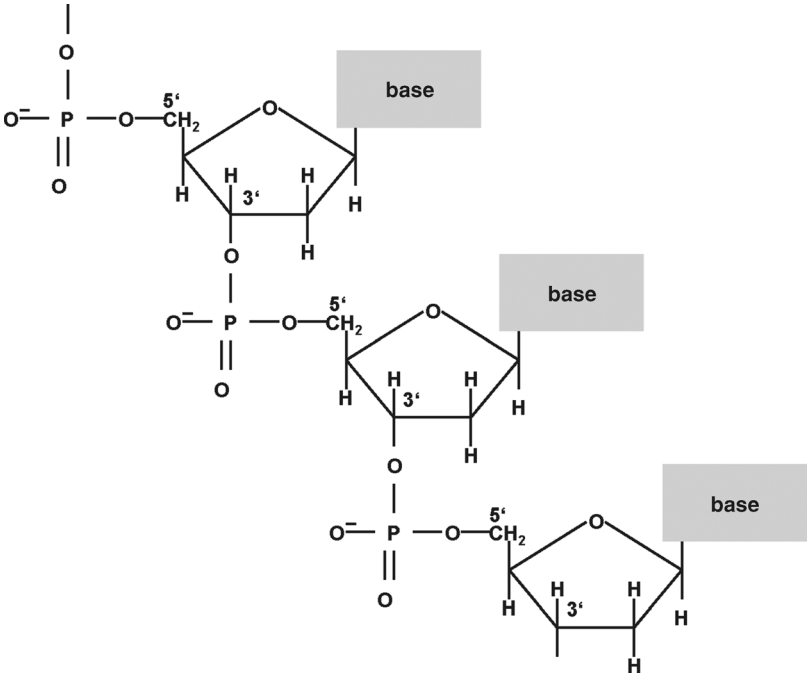

Figure 1.8 Single-stranded DNA or RNA consisting of three nucleotide units linked by phosphate groups.

behavior manifests as an effective interaction between the bases with the tendency to arrange themselves in stacks so that their contact with water is minimal. This hydrophobic base-stacking interaction also stabilizes the structure of nucleic acids. In addition to the hydrophobic interaction, there are binding sites on the bases, provided by ring nitrogens, carbonyl groups, and exocyclic amino groups. Amino and carbonyl groups enable the formation of hydrogen bonds between base stacks of two or more nucleic acids. (Artificial nucleic acids with more than two strands are relevant in biotechnology.) In their fundamental work on the molecular structure of double-stranded DNA and RNA published in 1953, Watson and Crick had revealed that these hydrogen bonds make the base pairings G–C and A–T in DNA (and G–C and A–U in RNA) (Watson and Crick, 1953) (see Figure 1.9).

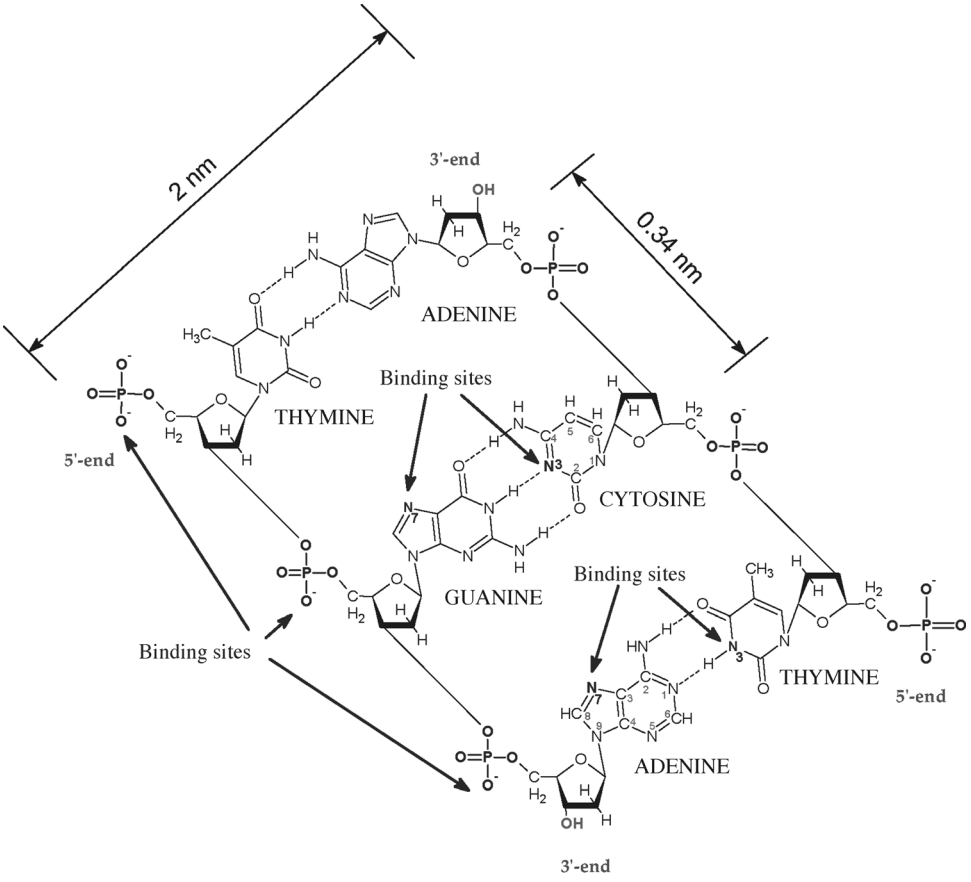

Figure 1.9 Chemical structure of a short sequence of a DNA double helix. The hydrogen bonds between the bases are indicated as dashed lines. There are two classes of binding sites of interest for DNA-templated nanowire fabrication: negatively charged phosphate groups in the backbone, N7 atoms of bases G and A, and N3 atoms of bases C and T acting as electron donors.

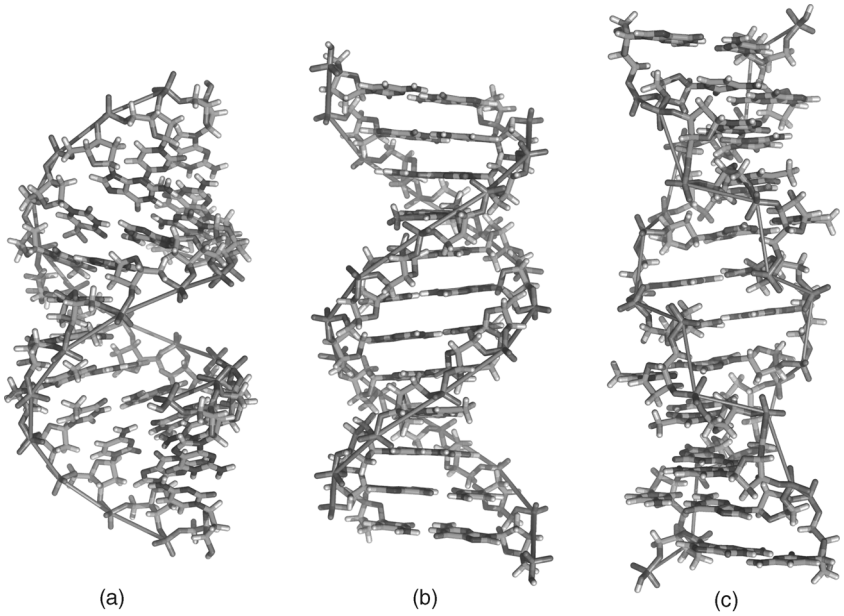

Figure 1.10 Structures of double-stranded DNA: (a) A-DNA; (b) B-DNA; (c) Z-DNA (*Source*: Wikimedia Commons; author Richard Wheeler (Zephyris).)

The double helix consisting of two DNA strands wound around a common axis, with the hydrophobic purine and pyrimidine bases arranged inside and the hydrophilic backbone of each strand facing the surrounding water, has an energetically favorable configuration. As seen in Figure 1.9, the oligonucleotides are not symmetrical with respect to reversal of direction. Note the opposite orientations of the nucleotide sequences, aligned from the end with the 5′-pentose site to the end with a 3′-pentose site. The base sequence TGA of the left strand matches the TCA sequence of the right strand only if the two are arranged in an antiparallel manner. There are three different conformations of the double helix structure. Under *physiological conditions*, the most stable form of DNA is the so-called B-form (Figure 1.10b). It is a right-handed double helix with a diameter of ∼2.0 nm and 10.5 base pairs per one helical turn. With *decreasing humidity*, the B-DNA can change its structure into A-DNA, a right-handed double helix, which is slightly more densely packed. It is not known whether the A-form DNA occurs in cells. The third conformation, the Z-DNA, is a slender left-handed double helix with a zigzag-shaped backbone. Particular nucleotide sequences, as alternating pyrimidine–purine sequences, fold preferentially into Z-DNA. Short strands of Z-DNA have been found in bacteria and eukaryotes. Characteristic parameters of the three forms are given in Table 1.2. Usually, the B-DNA is applied in bionanotechnology.

Double-stranded DNA (dsDNA) is stable under conditions near pH 7.0 and room temperature. Above 80 °C or at extreme pH, the viscosity of an aqueous solution of dsDNA is much lower than that under normal conditions, which is the result of a

Table 1.2 Characteristic geometric parameters of the DNA configurations.

	A-form	B-form	Z-form
Helical sense	Right-handed	Right-handed	Left-handed
Diameter	2.6 nm	2.0 nm	1.8 nm
Base pairs per helical turn	11	10.5	12
Helix rise per base pair	0.26 nm	0.34 nm	0.37 nm
Tilt of the bases normal to the helix axis	20°	6°	7°

reversible structural transition called *denaturation*. The denaturation consists in splitting of the double-stranded DNA into single-stranded DNA (ssDNA), which arrange themselves in random coils (Figure 1.11). The UV absorption (near 260 nm) of ssDNA is higher than that of dsDNA. By setting the conditions back to normal, the denaturation is reversed. The midpoint temperature T_m of the transition range is called the *melting point* of the DNA (Figure 1.12). It depends on the ratio of G–C and A–T base pairs. As a consequence of the higher effective binding energy of G–C pairs with three hydrogen bonds compared to the A–T pairs with two hydrogen bonds, the melting point of DNA increases with increasing G–C content.

The reversibility of the dissociation of double-stranded DNA and the association of the respective single-stranded DNA (the so-called hybridization) is the key for the replication of the genetic information in living organisms. This simple structural design in connection with the high mechanical stability of the information inscribed

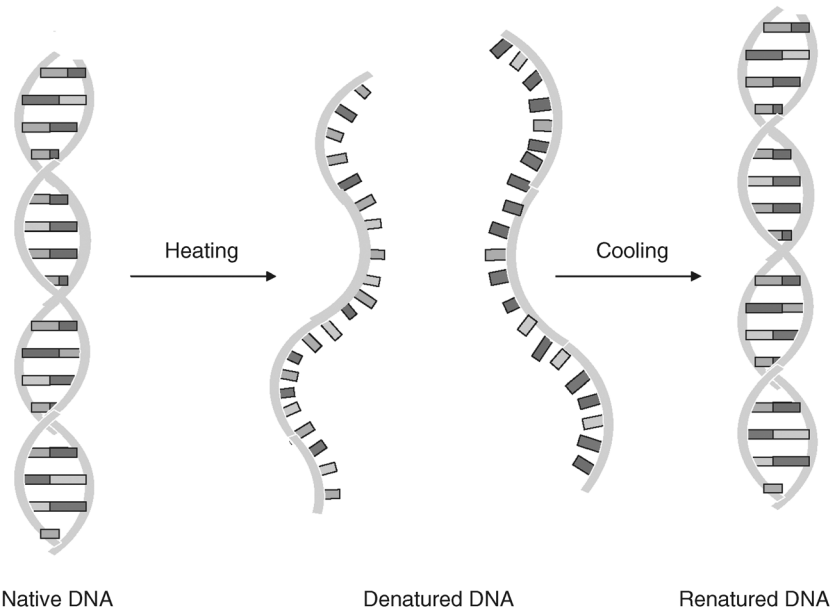

Figure 1.11 Denaturation (melting) and renaturation (hybridization) of a double-stranded DNA.

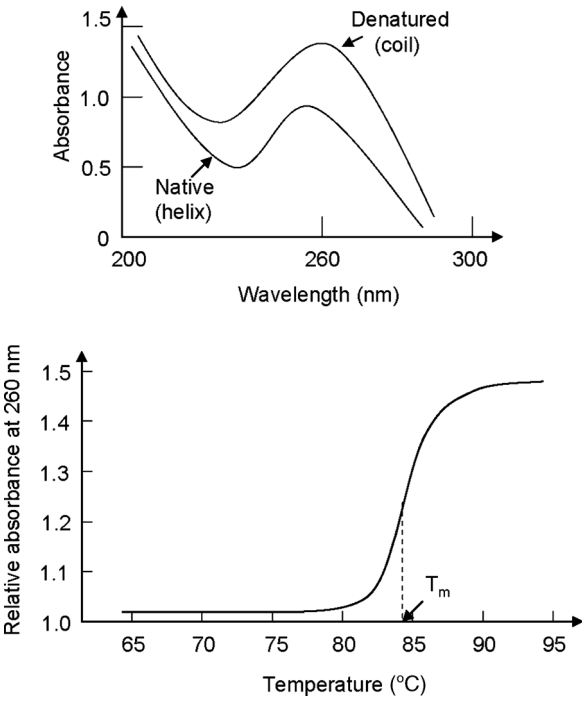

Figure 1.12 Change of the optical absorbance caused by melting of double-stranded DNA (T_m = melting temperature).

in the double-stranded chain molecule is crucial for minimizing errors in the replication process. However, rare alterations in the DNA sequence (mutations) are also stably replicated. Clearly, the molecular structure of the DNA is one essential precondition for the evolution of life with sufficient stability. At the same time, the ability to form double-stranded DNA segments by hybridization of complementary single-stranded oligomers and the possibility to reversibly disassemble the resulting double-stranded DNA into the constituent single-stranded DNA make DNA oligomers an ideal "brick" in soft nanotechnology, as we will see in the following.

1.1.2 Proteins

Proteins can be subdivided into structural and functional proteins can be. *Structural proteins* (e.g., collagen in soft and hard tissues, surface layers of many bacteria, and the cage-forming ferritin protein) are responsible for the molecular (pre)organization of structural units. *Functional proteins* (*enzymes*) catalyze the primary life processes of the organism, such as oxygen transport, sugar cycles, regulation of fuel supply for cellular machinery (e.g., synthesis of ATP and GTP), formation of the new structural proteins, transport processes via cell membrane,

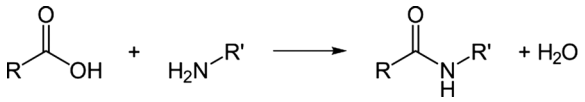

Figure 1.13 Formation of a peptide bond by condensation.

remodeling of tissue, and motion of muscles. Therefore, they can be regarded as the "functional molecules of life" (Lezon, Banavar, and Maritan, 2006).

The *primary structure* of a protein is quite simple. It is assembled as a chain of a limited number of 20 α-amino acids that differ in their side chains. These short side chains, or residues (R groups), determine the physical and chemical properties of the different amino acids, including their solubility in water. The backbone of a protein is formed by the so-called peptide bonds. They are formed by the removal of OH^- from the α-carboxyl group of one amino acid and H^+ from the α-amino group of a second amino acid. The result of this condensation reaction is a dipeptide and water (Figure 1.13).

The terminal amino acid residue with a free α-amino acid group is called the amino-terminal (or N-terminal) residue, whereas the other end with the α-terminal carboxyl group is the carboxyl-terminal (or C-terminal) residue. Peptide bonds are very stable with an average half-life of about 7 years under intracellular conditions excluding enzymatic cleavage. Condensed amino acids are called *oligopeptides* or *polypeptides*, depending on the number of amino acid residues. Polypeptides with a molecular weight higher than 10 000 are referred to as proteins. Typically, proteins are chains of few hundred up to few thousand amino acid residues. The 20 *natural amino acids* can be subdivided into seven groups of similar functionality, which they fulfill in the chain sequence of a particular protein (see Table 1.3).

Proteins usually consist of one long single polypeptide chain but there are also *multimeric proteins* consisting of two or more mostly noncovalently bonded polypeptide chains. For example, *E. coli* RNA polymerase, the enzyme that mediates the transcription of the genetic information of double-stranded DNA into RNA strands, is composed of five polypeptide chains.

Proteins often perform a specific task million-fold with high reliability. Therefore, proteins must be stable under changing conditions. However, stability alone is not the only property that accounts for the utmost importance of proteins in all living organisms (Lezon, Banavar, and Maritan, 2006). In order to realize the essential feature of living matter – cooperation – on all scales from a small organelle inside a cell up to a complex organism, the proteins exhibit properties such as high specificity of interaction and functional diversity, self-organization in higher ordered networks, and high sensitivity with respect to external signals. High specificity and diverse functionality can be realized by a combination of rigid subunits that can be arranged with high flexibility. An arrangement of the subunits in a chain is a possible solution for that. However, the variety of a longer chain must be restricted to a limited number of structures. It should be excluded that each mutation leads to a significant change of the phenotype. Otherwise, the number of phenotypes to be displayed should be large enough that evolution is not precluded when the

Table 1.3 Structure and functionality of natural amino acids classified by the R groups (for abbreviation a three-letter or one-letter code is used).

Name/short notation	Structure	Functionality
Control of protein backbone properties		
Glycine (Gly, G)	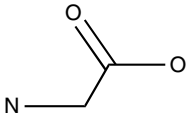	Smallest amino acid without side chain, making the protein chain more flexible
Proline (Pro, P)	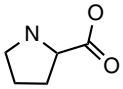	With two covalent bonds to the backbone, forming a kink in the chain
Carbon-rich side chains driving protein folding		
Leucine (Leu, L)	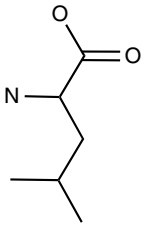	Hydrophobic domains forming closely packed clusters inside the protein
Isoleucine (Ile, I)	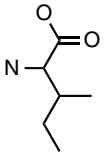	Hydrophobic domains forming closely packed clusters inside the protein
Alanine (Ala, A)	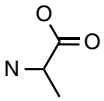	Hydrophobic domains forming closely packed clusters inside the protein
Valine (Val, V)	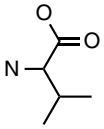	Hydrophobic domains forming closely packed clusters inside the protein
Aromatic rings driving protein folding		
Phenylalanine (Phe, F)	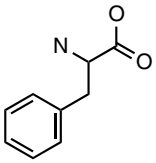	Hydrophobic domains, aromatic rings often form stacks of one upon another
Tryptophan (Trp, W)	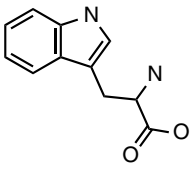	Hydrophobic domains, aromatic rings often form stacks of one upon another

(*continued*)

Table 1.3 (*Continued*)

Name/short notation	Structure	Functionality
Tyrosine (Tyr, Y)	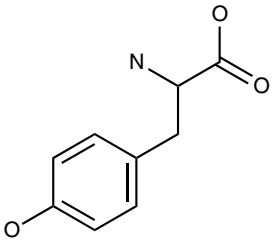	Hydrophobic domains, aromatic rings often form stacks on top of one another, hydroxyl group acts as possible binding site
Diverse hydrogen bonding groups		
Histidine (His, H)	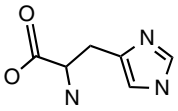	Imidazole group can be neutral or charged depending on pH, can fulfill catalytic tasks, coordinates strongly with metal ions
Serine (Ser, S)	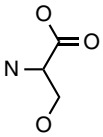	Very often at protein surfaces, offering hydrogen bonding groups
Asparagine (Asn, N)	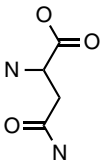	Very often at protein surfaces, offering hydrogen bonding groups
Threonine (Thr, T)	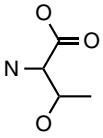	Very often at protein surfaces, offering hydrogen bonding groups
Glutamine (Gln, Q)	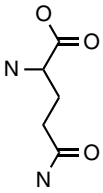	Very often at protein surfaces, offering hydrogen bonding groups
Carboxylic acid binding groups		
Aspartate (Asp, D)	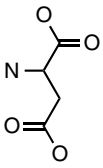	At neutral pH negatively charged; at protein surfaces, metal ion binding

Table 1.3 (*Continued*)

Name/short notation	Structure	Functionality
Glutamate (Glu, E)	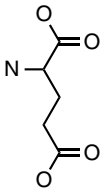	At neutral pH negatively charged; at protein surfaces, metal ion binding
Positively charged surface binding sites		
Lysine (Lys, K)	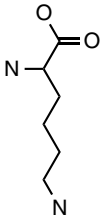	Amine end group ionized under neutral pH, carbon-rich chain plays a role in interaction with other carbon-rich molecules
Arginine (Arg, R)	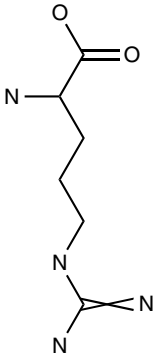	Guanidinium group ionized under neutral pH, carbon-rich chain plays a role in interaction with other carbon-rich molecules
Sulfur-containing groups		
Cysteine (Cys, C)	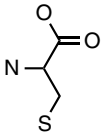	Most reactive amino acid, forms covalent disulfide cross-links, coordinates strongly with metal ions
Methionine (Met, M)	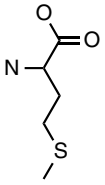	Has a hydrophobic sulfur atom, promotes protein folding, sulfur atom coordinates with metal ions

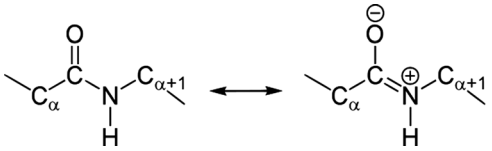

Figure 1.14 Peptide bond. It exists in two resonance forms, an uncharged (about 60%) and a charged (about 40%) form.

environmental conditions are changing. These demands to be fulfilled by a "molecule of life" explain why we observe the folding of the protein chains into more compact structures with pronounced stability and specificity (Lezon, Banavar, and Maritan, 2006). Primary, secondary, tertiary, and quaternary structures distinguish the various structure levels of folded proteins.

The *primary structure* of a protein is determined by the sequence of amino acids. Peptide bonds and disulfide bonds link the amino acids in a polypeptide chain. The covalent bonds in the polypeptide backbone cause essential constraints on the protein structure. The peptide group forming that backbone group consists of six atoms arranged in one plane, where the oxygen atom of the carbonyl group stays in *trans* position to the hydrogen atom of the amide nitrogen (Figure 1.14). The α carbons of adjacent amino acid residues are separated by three covalent bonds, aligned as $C_\alpha—C—N—C_{\alpha+1}$. The C—N bond has a partial double bond character (about 40%). Therefore, the oxygen has a partial negative charge and the nitrogen a positive charge, which leads to a small electric dipole. These dipoles can line up into large dipoles. The regular assembly of electric dipoles of the peptide bond along the protein backbone is the basis of the observed piezoelectric behavior of proteins (Lemanov, 2000). There is an ongoing discussion whether piezoelectricity could play a role in the biomineralization of collagen (see also Section 6.3.2.1).

The *secondary structure* describes stable spatial arrangements of amino acids in a particular segment of the whole protein, without regarding the arrangement of the side chains of the amino acids or their relation to other segments. Only a few types of stable secondary protein structures are realized. Partial sequences of the backbone are often organized as α-helices or β-sheets (Figures 1.15 and 1.16). Already in the 1950s, Pauling and Corey have pointed out that the short-ranging *weak hydrogen bonds* between the amino acids are the reason for the formation of the α-helices and β-sheets (Pauling and Corey, 1951). In α-helices, the protein backbone is wound around an imaginary axis. The side groups of the amino acids are arranged outside the helix. The step height of the helix is about 0.54 nm. Each helical turn includes 3.6 amino acids. Hydrogen bonds between the hydrogen attached to the nitrogen atom of the peptide bond of the nth amino acid in the chain along the backbone and the oxygen atom of the carboxyl group of the $(n+4)$th amino acid stabilize the helix. Every peptide bond along the helix involves a hydrogen bond. The β-sheets are composed of aligned strands connected by hydrogen bonds. The strands of the β-sheets are arranged in two-stranded ribbons, multistranded sheets, or barrel-like structures. The amino-terminal to carboxyl-terminal orientations of adjoining chains can be the same (parallel β-sheets) or opposite (antiparallel β-sheets). A

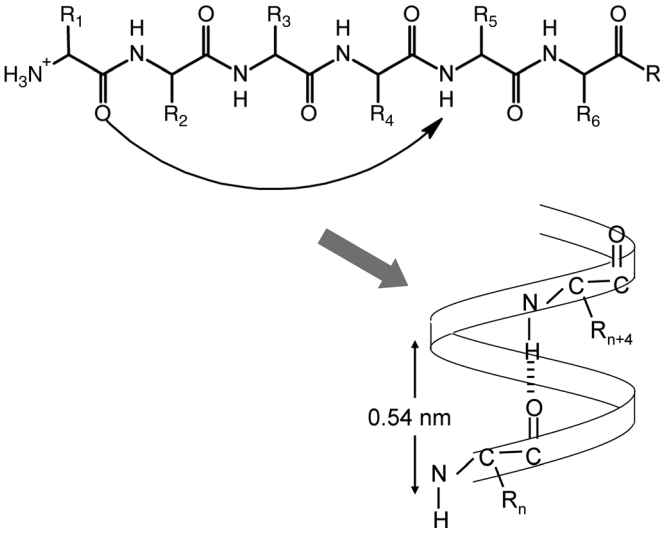

Figure 1.15 α-Helix. Each turn of the helix consists of 3.6 amino acids, which places the C=O group of amino acid *n* exactly in line with the H—N group of amino acid $n + 4$.

survey of all known natural proteins reveals that about one-third of all amino acids are found in α-helices and one-fifth in β-sheets.

The *tertiary structure* is the three-dimensional structure of a polypeptide chain, as defined by the atomic coordinates. There are filamentous and globular tertiary structures. Functional properties of proteins such as molecular recognition, catalytic activity, and preorganization of mineralized tissue are to a large extent regulated by

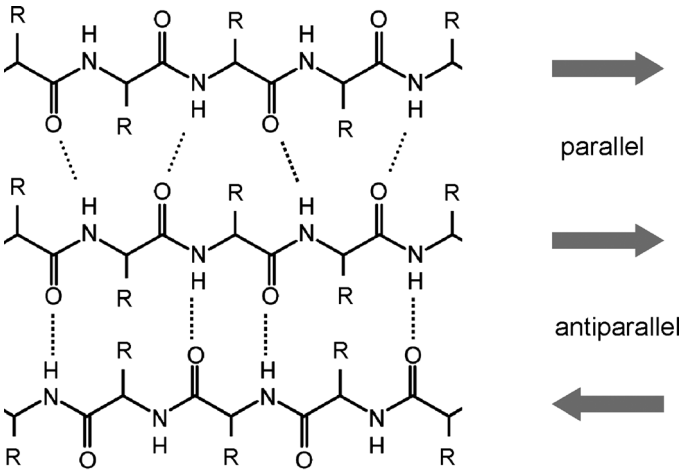

Figure 1.16 β-Sheet. Extended strands are lined up side by side, and H-bonds bridge from strand to strand. Identical or opposed strand alignments make up parallel or antiparallel β-sheets.

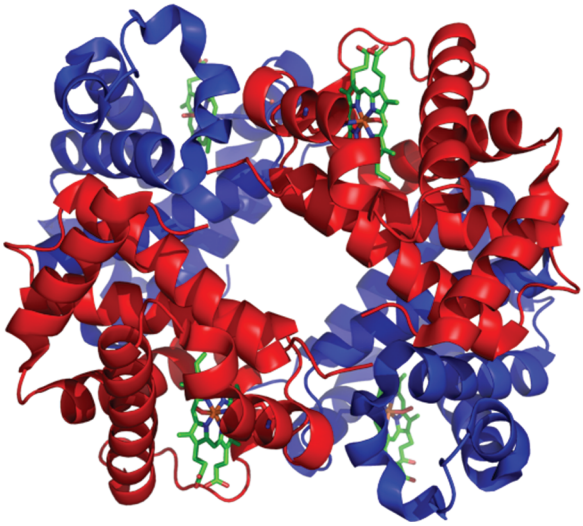

Figure 1.17 Structure of human hemoglobin. The protein α and β subunits are in red and blue and the four iron-containing heme groups in green. Binding of one oxygen molecule to one of four possible binding sites leads to a conformation change resulting in enhanced oxygen binding efficiency. (*Source*: Wikimedia Commons; author Richard Wheeler (Zephyris).)

the tertiary structure. Therefore, the successful use of proteins in biohybrid man-made materials requires that the tertiary structure of the protein is reproduced with high precision.

Quaternary structures are arrangements of multiple polypeptide subunits. Often these subunits can also fulfill regularity tasks. Binding of small molecules to subunits can cause large changes in the quaternary structure. A well-studied example is the tetrameric hemoglobin, the carrier of oxygen in the blood, which consists of four subunits (Figure 1.17). Binding of oxygen or carbon dioxide causes essential conformational changes that allow an optimized uptake and release of oxygen in the various tissues.

Another example is the iron storage protein ferritin (see also Section 6.2.6), which consists of 24 monomers. The quaternary structure, a spherical cage formed by 12 dimers, contains reaction centers for the catalytic oxidation of Fe(II) to Fe(III), and specific reaction sites for the deposition of ferrihydrite ($Fe_2O_3 \cdot nH_2O$).

Capsids Capsids are higher order protein structures constituting the shell of viruses. Their high regularity and stability make them suitable for various applications in nanobiotechnology. The capsids form a cage for the genetic material of the virus, either DNA or RNA. The coat proteins are arranged in the capsids mainly in an *icosahedral* or *helical* way. The icosahedral shape is composed of 20 equilateral triangular faces. Three examples of icosahedral viruses are shown in Figure 1.18.

The helically shaped capsids form filamentous cylinders. Capsids can consist of one or more different proteins. The filamentous capsid of bacteriophage M13, which

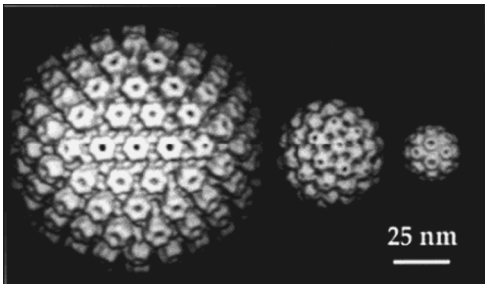

Figure 1.18 Image reconstructions of spherical (icosahedral) viruses: equine herpes virus, cauliflower mosaic virus cowpea, and chlorotic mottle virus (left to right). (Reproduced with permission from Douglas and Young (1999). Copyright 1999, Wiley-VCH Verlag GmbH.)

is often used in bioengineering, is a flexible rod of about 1 μm length. It consists of five different proteins: the major protein gp8 with about 2700 copies per phage, 5 copies of the minor proteins gp3 and gp6 that are placed at one end of the rod, and 5 copies of the proteins gp7 and gp9 at the other end (Figure 1.19).

The tobacco mosaic virus (TMV) is a very stable filamentous virus. The capsid is 300 nm long with 18 nm outer and 4 nm inner diameter (see Figure 1.20). A RNA is

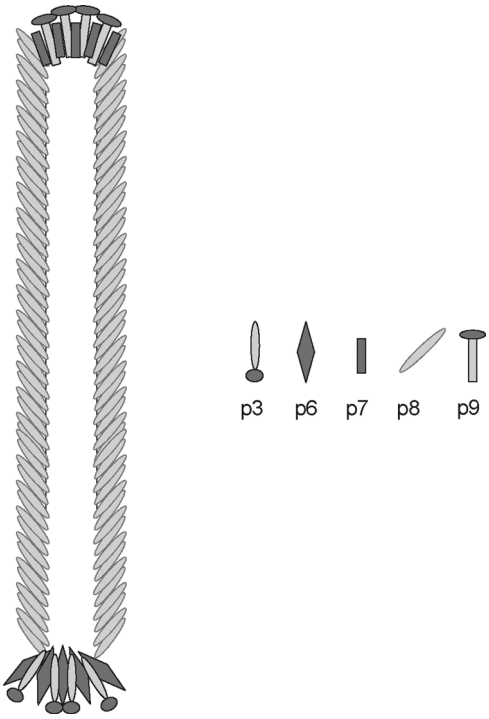

Figure 1.19 Structure of the filamentous M13 phage.

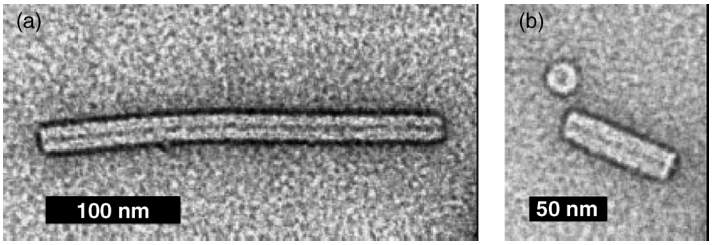

Figure 1.20 Transmission electron microscopy (TEM) images of TMV at 400 kV. (a) Intact virus, stained with uranyl acetate. The central channel and the exterior surface appear black, that is, uranium-rich. (b) Virus fragments: the circular shape is a very short fragment standing upright on the substrate. (Reproduced with permission from Knez *et al.* (2004). Copyright 2004, Wiley-VCH Verlag GmbH.)

surrounded by a helical assembly of 2130 coat proteins. The TMV exhibits a surprising stability at temperatures up to 90 °C and pH values from 3.5 up to 9. These properties make TMV a useful template in bionanotechnology.

Some virus capsids can undergo structural transitions induced by chemical switching, a property of interest for potential applications in bionanotechnology. The plant virus cowpea chlorotic mottle virus (CCMV), for example, shows a pH-dependent structural change (Douglas and Young, 1999). Its capsid is composed of 180 identical coat protein subunits assembled to an empty cage with an outer diameter of 26 nm and an inner diameter of about 20 nm. CCMV shows a reversible swelling of 10% at pH >6.5. This increase in diameter is connected with the formation of 60 pores in the protein shell (diameter 2 nm). At pH <6.5, the pores are closed. Thus, the reversible shape transition enables a pH-dependent switching of entrapment and release of substances.

The so-called bacteriophages (or phages), members of the group of viruses that infect bacteria, are of major interest in nanotechnology. The above-mentioned M13 virus and tobacco mosaic virus are examples. Bacteriophages are assumed to be the most abundant entities in the biosphere. About 10^9 phages per milliliter are found at the surface of biofilms. The fast replication cycles of phages in the bacterial host cells are an essential advantage for potential nanotechnological applications. The virus attaches to receptors on the surface of the bacterium and injects genetic material through the cell wall, whereupon the bacterium interrupts its normal synthesis processes and churns out virus components. Within a few minutes, new phages are assembled and released via cell lysis or budding. Filamentous phages can also be released continuously. These are rapid processes that enable phage libraries with typically 10^9 or more phages to be set up rather quickly (see also Section 2.3).

1.1.3
Carbohydrates

The term "carbohydrates" indicates that this large group of organic compounds can be formally regarded as hydrates of carbon, as they seem to be mainly composed of a

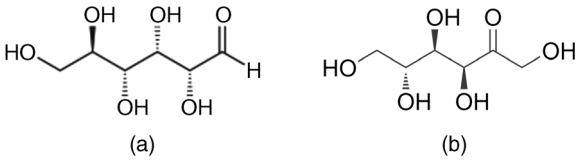

Figure 1.21 Chain structure of D-glucose (a) and D-fructose (b).

backbone of carbon to which hydroxyl groups and hydrogen atoms are attached. Carbohydrates such as cellulose, sugar, or starch are the biomolecules with largest abundance on Earth. The photosynthesis is the unlimited process for production of cellulose in plant cells. Sugar and starch are important energy deposits in biological structures. According to the number of combined monosaccharide units, carbohydrates are usually subdivided into the following: monosaccharides, disaccharides, oligosaccharides, polysaccharides, and glycoconjugates.

Monosaccharides have an unbranched backbone. The backbone can be an open chain or a cyclic structure. They exhibit two or more hydroxyl groups. In the open chain, one of the carbons is double bonded to one oxygen atom to form a carbonyl group. This carbonyl group can be either at the end of the open chain (*aldose*) or at any other position of the chain (*ketose*). Hydroxyl groups are attached to all other carbon atoms. The aldohexose D-glucose and the ketohexose D-fructose are the most frequent natural monosaccharides (Figure 1.21). The carbonyl group can be oxidized to a carboxyl group, which implies that glucose and other sugars of similar structure are reducing molecules. The carbonyl group can form a covalent bond with a hydroxyl group further down the chain resulting in a cyclic structure (Figure 1.22). In aqueous solution, saccharides with four or more carbon atoms form preferentially cyclic structures.

Disaccharides (e.g., maltose, lactose, and sucrose) consist of two monosaccharides covalently joined by an O-glycosidic bond. This bond can be hydrolyzed under acidic conditions (Figure 1.23).

Oligosaccharides are short chains of n monosaccharides ($3 \leq n \leq 20$) joined by glycosidic bonds. Oligosaccharides are often joined to lipids or proteins forming the so-called glycoconjugates. *Polysaccharides* containing only one carbohydrate species are called *homopolysaccharides*, while *heteropolysaccharides* are composed of different carbohydrates. Examples of homopolysaccharides are starch (Figure 1.24) and glycogen (animal starch), the storage forms of monosaccharides,

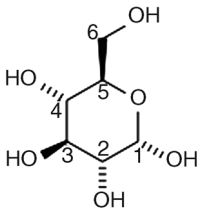

Figure 1.22 Cyclic structure of D-glucose.

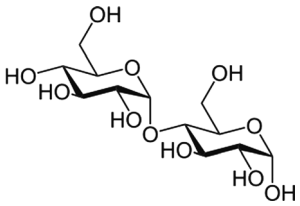

Figure 1.23 Structure of the disaccharide maltose, which consists of two D-glucose units.

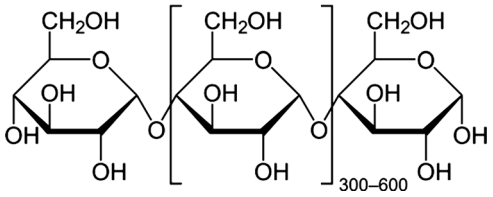

Figure 1.24 Starch or amylose consists of a large number of α-D-glucose units joined together by glycosidic bonds. It is produced by green plants as energy store.

and structure-forming molecules such as cellulose (Figure 1.25), chitin, and chitosan (Figure 1.26). Examples for structural heteropolysaccharides that are of interest for the development of bio-inspired materials are hyaluronic acid (or hyaluronan) and alginate (Figures 1.27 and 1.28).

Glycoconjugates are hybrid structures of polysaccharides and proteins or lipids (see Table 1.4 and Figure 1.29). They are signal carriers for the intramolecular assembling of biomolecules. Usually, oligosaccharides are covalently linked with proteins or lipids to form glycoconjugates, which are subdivided into proteoglycans, glycoproteins, and glycolipids.

Oligo- and polysaccharides can be important information carriers, for example, in the communication between cells and the surrounding media. Examples are recognition sites on the cell surfaces. Often a thick layer of oligosaccharides, the glycocalyx, covers the plasma membrane of eukaryotic cells. This layer contains molecular information inscribed in the carbohydrates. Oligosaccharides and polysaccharides offer multiple binding sites for amino acids and

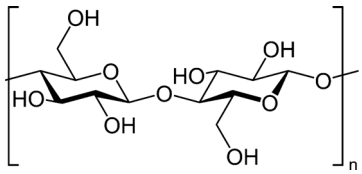

Figure 1.25 Cellulose consisting of a linear chain of several hundred to more than 10 000 β-D-glucose units. Cellulose is the structural component of the primary cell wall of green plants, many forms of algae, and oomycetes. Some bacteria secrete it to form biofilms.

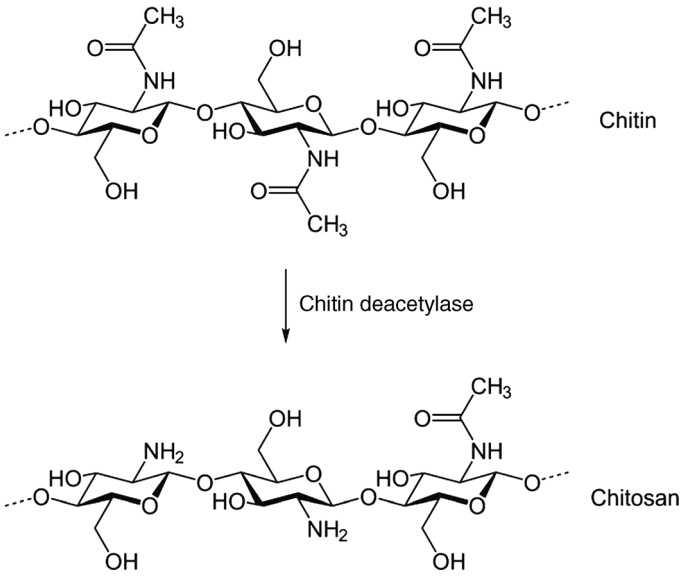

Figure 1.26 Chitin and chitosan. Chitin, a chain polymer of *N*-acetylglucosamine, is the main component of cell walls of fungi, the exoskeletons of arthropods (crustaceans and insects), or the radula of mollusks. Chitosan is produced by deacetylation of chitin. It is composed of randomly distributed glucosamine (deacetylated unit) and *N*-acetylglucosamine (acetylated unit). The biocompatible chitosan is an interesting scaffold material for tissue engineering.

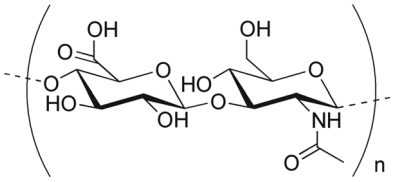

Figure 1.27 Hyaluronic acid, an anionic glycosaminoglycan, is composed of D-glucuronic acid and D-*N*-acetylglucosamine. It is one of the main components of the extracellular matrix distributed widely throughout connective, epithelial, and neural tissues.

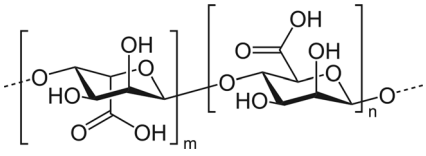

Figure 1.28 Alginate, an anionic polysaccharide, is widely distributed in the cell walls of brown algae. It is a linear copolymer with homopolymeric blocks of β-D-mannuronic acid (right block in the figure) and α-L-guluronic acid residues (left block in the figure).

Table 1.4 Subgroups of glycoconjugates.

Glycoconjugates	Structures
Proteoglycans	The basic unit is a core protein. One or more glycosaminoglycan chains are covalently joined to membrane proteins or proteins of the extracellular matrix. The glycosaminoglycan chain can bind via electrostatic interaction to extracellular proteins. Proteoglycans organize the extracellular matrix or are integrated in the cellular membrane.
Glycoproteins	One or more oligosaccharides (glycans) are covalently joined to a protein outside or inside cells. The glycans are smaller and more branched than the glycosaminoglycans of proteoglycans. By the binding of negatively charged oligosaccharides, the polarity and solubility of the proteins can be changed. This can lead to rod-like structures. Furthermore, it can protect the proteins from the attack of proteolytic enzymes. Glycoproteins form highly specific recognition sites, for example, for lectins.
Glycolipids	The head groups of some membrane lipids can be complex oligosaccharides. Thus, the outer membrane of Gram-negative bacteria such as *E. coli* and *Salmonella typhimurium* is composed of lipopolysaccharides (Figure 1.29). These structures are targets of antibodies produced by the immune system in response to bacterial infection.

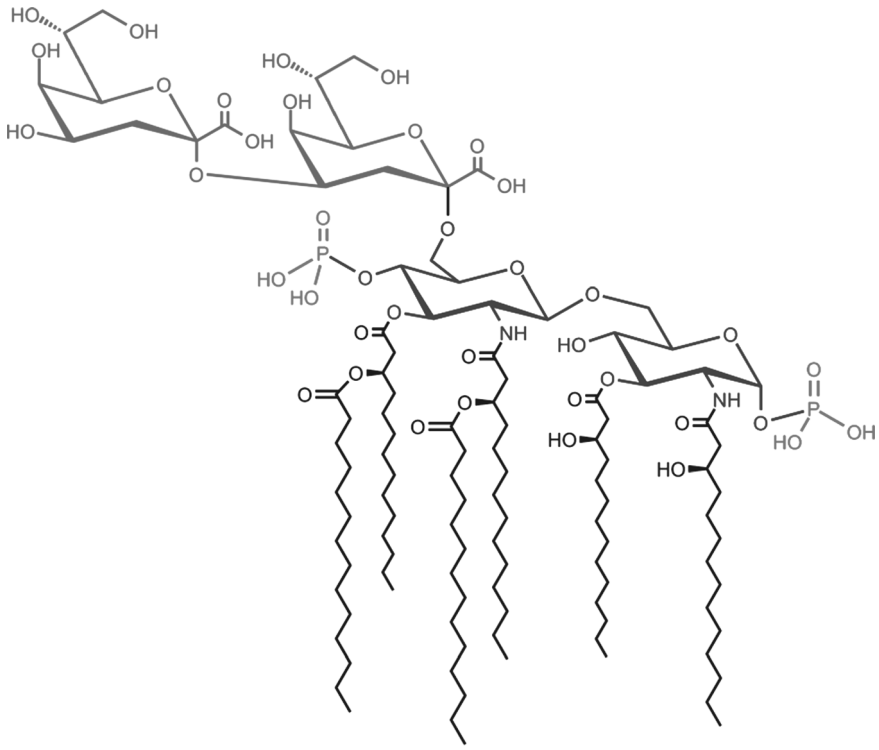

Figure 1.29 Structures of a bacterial lipopolysaccharide, the (3-deoxy-D-manno-octulosonic acid)$_2$–lipid A endotoxin from *E. coli* K-12. (*Source*: Wikimedia Commons; author Tim Vickers.)

nucleotides. To get an impression of the enormous wealth of information, we can make a rough estimate of the number of combinations of a hexameric oligosaccharide with the various amino acids or nucleotides. For conjugations with the 20 natural amino acids, we get 20^6 possibilities, whereas there are 4^6 possibilities for linkages with nucleotides. Despite stereochemical restrictions that will reduce these numbers, the estimate demonstrates the enormous information density that could be realized in glycoconjugates. Lectins, a ubiquitous group of proteins, bind with high specificity to carbohydrates. Lectins are found in plants (e.g., concanavalin A), animals (e.g., galectin-1 and mannose binding protein A), viruses (e.g., hemagglutinin), and bacteria (enterotoxin). It is reasonable to expect that further progress in glycobiology will significantly increase the relevance of the *sugar code* for application in bionanotechnology.

1.1.4 Lipids

Lipids are a large group of insoluble biomolecules with diverse functions. The insolubility in water is the group defining property. Depending on the functions, three subgroups of lipids are distinguished: storage lipids (fats and oils) acting as energy reservoirs, structural lipids (mainly phospholipids and sterols) constituting the major structural components of membranes, and a larger group of functional lipids such as cofactors, electron carriers, light absorbing pigments, chaperones, and emulsifying agents. Compared to nucleic acids or proteins, lipids are small molecules. With a charged head group and a carbon–hydrogen tail they are amphiphilic, which means they combine the hydrophilicity of the polar head and hydrophobicity of carbon–hydrogen tail in one molecule. As we will discuss in Chapter 7, this combination provides the ability of forming self-organized structures of a particular type. The chemical diversity of the head groups permits the realization of a large variety of different functions in biological structures. Several structural characteristics of the three subgroups are compiled in Table 1.5 (see Figures 1.30–1.32).

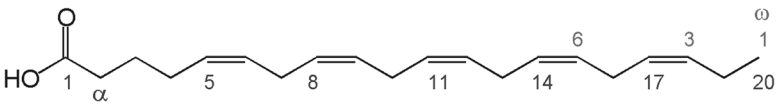

Figure 1.30 Example of a polyunsaturated fatty acid: 20:5($\Delta^{5,8,11,14,17}$) eicosapentaenoic acid (EPA), an omega-3 fatty acid. Two nomenclatures are used for fatty acids. In the standard version, the number 1 denotes the carboxyl carbon (C-1), and α the carbon next to it. The positions of double bonds are assigned by Δ followed by numbers indicating the lower numbered carbons in the double bonds. In an alternative version, the carbons are numbered in the opposite direction: number 1 is the methyl carbon at the end of the chain (ω carbon). The positions of double bonds are indicated relative to the ω carbon.

Table 1.5 Classification and structural characteristics of lipids.

Lipids	Structures
Fatty acids	Fatty acids are carboxylic acids with hydrocarbon chains with saturated (single) and unsaturated (double) carbon bonds (number of carbons in the chain n_{Carbon} from 4 to 36). The fatty acids exhibit a very low oxidation state. Therefore, they are particularly suited for energy storage. The melting point is higher for longer hydrocarbon chains and smaller number of unsaturated carbon bonds (unsaturated fatty acids). Example: see Figure 1.30
Structural lipids	Double layers of structural lipids constitute the main structural element of biological membranes. Their general structure with a polar head group (hydrophilic) and hydrophobic tails (fatty acids) explains the amphiphatic character of membrane lipids. Depending on the head groups, five general types of membrane lipids are distinguished: • glycerophospholipids • galactolipids and sulfolipids • archaeal tetraether lipids • sphingolipids • sterols. Example: see Figure 1.31
Functional lipids	Functional lipids are essential components of the cell metabolism. They can act as signal molecules (e.g., hormones and growth factors), enzyme cofactors (e.g., for electron-transfer reactions in chloroplasts and mitochondria), light absorbing pigments, or volatile lipids in plant communication. Example: see Figure 1.32

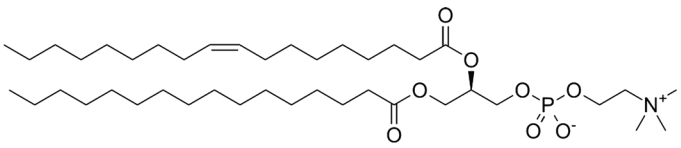

Figure 1.31 Chemical structure of the glycerophospholipid 1-palmitoyl-2-oleoylphosphatidylcholine (POPC).

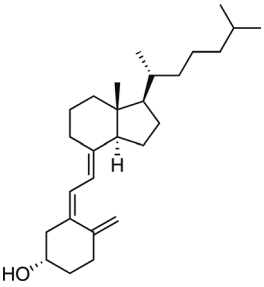

Figure 1.32 Structure of cholecalciferol (vitamin D_3). This hormone regulates the Ca^{2+} metabolism in kidney, intestine, and bone.

1.2
Basic Principles

In this chapter, a number of principles is explained which are the reasons for more general structure–property relations observed with biomolecules. They are also important for the understanding of the following chapters. While some properties result from the polymer structure, others reflect unique features directly connected with the particular biochemical properties of the molecules.

1.2.1
The Persistence Lengths of Biopolymer Chains

It is a typical structural characteristic of many biomolecules that their basic chemical entities are arranged in a chain structure. Obviously, the chain is the geometrically best solution to inscribe the information needed for a specific function in a molecular structure. In addition, the arrangement of the chain in the space offers ideal options for controlling readout processes of the information. Therefore, a more detailed geometrical characterization of deformed biomolecular chains is of high interest. Phenomenologically, a deformed molecular chain can be described in a continuum model. Let us consider a long thin biopolymer such as a double-stranded DNA or an actin filament, one of the main components of the cytoskeleton. To describe a point at the nondeformed chain, we introduce the distance s from one end along the chain. When the chain is deformed, this point is shifted to the position with the distance $s' = s + \Delta s$ from the chain end, where Δs denotes the displacement of the position s. The complete biopolymer can be described as a chain of small elastic rods of length ds with a tangential vector $\vec{t}(s)$ (see Figure 1.33). Due to the deformation, the length of the small elastic rod is changed to $ds' = ds + d\Delta s \equiv ds(1 + u(s))$. Here $u(s) = d\Delta s/ds$ denotes the tensile

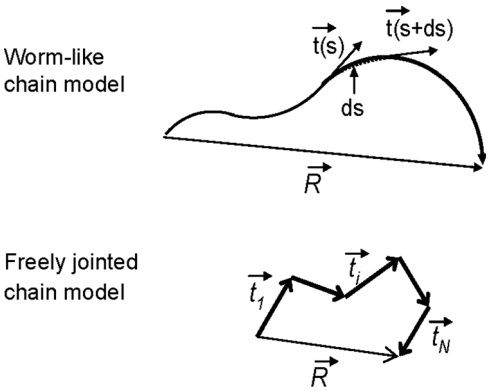

Figure 1.33 Description of a bent polymer chain in the worm-like chain model and in the freely jointed chain model. $\vec{R}$ denotes a vector pointing from the initial to the end point of the chain.

strain of the chain at the position s. For simplicity, we assume that the non-deformed polymer is a straight rod of length L. The change of the contour length ΔL of the deformed chain now can be expressed by $\Delta L = \int_0^L \mathrm{d}\Delta s = \int_0^L u(s)\mathrm{d}s$. For a complete description of the deformation of the chain, we have to introduce two more deformations: the curvature or bending deformation $\vec{\beta}\,(s) = \mathrm{d}\vec{t}\,/\mathrm{d}s$, where $\vec{t}\,(s)$ is the unit tangent vector changing along the chain, and the torsional deformation or twist density $\omega(s) = \mathrm{d}\Phi/\mathrm{d}s$, with $\Phi(s)$ as the twist angle. The total twist $\Delta\Phi$ is given by $\Delta\Phi = \int_0^{L_{\mathrm{tot}}} \omega(s)\mathrm{d}s$. If all deformations are elastic, the energy $\mathrm{d}W_{\mathrm{el}}(s)$ stored in the segment $\mathrm{d}s$ can be approximated by a quadratic dependence on the deformations $\vec{\beta}$, u, and ω:

$$\mathrm{d}W_{\mathrm{el}} = \frac{1}{2} k_{\mathrm{B}} T (A\vec{\beta}^{\,2} + Bu^2 + C\omega^2 + Du\omega)\mathrm{d}s. \tag{1.1}$$

As the energy is a scalar, mixed terms including the vector of the bending deformation do not contribute to the energy. We scale the energy coefficients in units of the thermal vibration energy per degree of freedom, $(1/2)k_{\mathrm{B}}T$, with k_B as the Boltzmann constant. $k_{\mathrm{B}}TA$, $k_{\mathrm{B}}TB$, and $k_{\mathrm{B}}TC$ are denoted as bending stiffness, stretch stiffness, and twist stiffness of the chain, respectively, whereas $k_{\mathrm{B}}TD$ is called twist–stretch coupling. A dimensional analysis shows that A and C have the dimension of a length [L], B has the dimension [L^{-1}], and D is dimensionless. A and C are termed as *bend persistence length* and *twist persistence length*, respectively. A stiff biomolecule is characterized by large persistence lengths. In the case of nearly free rotation of the monomers in the chain, the contributions of twist to the energy can be neglected so that C and D can be set equal to zero. In the often realized case where the chain is easily bent by applied forces f so small that the related strain u is negligible, the constant B, too, can be set equal to zero (see also Task 1.1). Thus, the model is reduced to a one-parameter description of the deformation, the so-called *simplified elastic rod model*, among the polymer community also known as the *worm-like chain model* (WLC) or *Kratky–Porod model*:

$$W_{\mathrm{el}} = \frac{1}{2} k_{\mathrm{B}} T \int_0^{L_{\mathrm{tot}}} A\vec{\beta}^{\,2}\,\mathrm{d}s. \tag{1.2}$$

Let us consider a short straight molecule of length l that has been bent with a radius of curvature R (Figure 1.34).

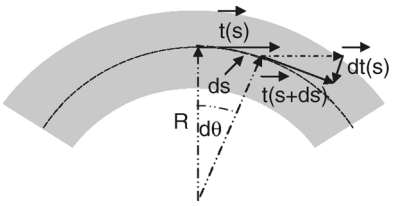

Figure 1.34 Definition of geometric parameters describing a bent polymer chain. R denotes the local radius of curvature.

Table 1.6 Examples of bend persistence lengths of biopolymers.

Biopolymer	Filament radius	Bend persistence length
Double-stranded DNA	$r = 1$ nm	50 nm
Amyloid protofibril		
With 100% ordered β-sheets	$r = 0.7$–1.8 nm	4 μm
With 50% ordered β-sheets	$r = 1.8$–2.5 nm	0.1 μm
Actin filament	Ellipse: $r_{max} = 3$ nm; $r_{min} = 2$ nm	15 μm
Microtubule	Tube: $r_{out} = 14.2$ nm; $r_{in} = 11.5$ nm	6 mm

From Eq. (1.2) for the elastic energy of a thin bent fiber follows $W_{el} = (1/2)k_B T(Al/R^2)$ (see also Task 1.2). Bending into a quarter of a circle, for example, which means $R = 2l/\pi$, requires the energy

$$W_{el}(\pi/2) = \left(\frac{\pi A}{4R}\right) k_B T. \tag{1.3}$$

Obviously, the ratio of bend persistence length, A, and radius of curvature, R, governs the elastic energy in a bent molecule. For small A/R, which means thermal energy fluctuations exceeding the elastic energy required for bending, the average conformation of the polymer is governed by entropy. Then the orientations of distant segments on the chain are not correlated but random. Indeed, biomolecules with lengths $L \gg A$ appear as a random tangle. In other words, the persistence length A is a measure for the length of the statistically independent segments, L_{seg}. This result leads to a second simplified model, in which the overall chain shape is modeled as a freely jointed chain of segments. In this so-called freely jointed chain (FJC) model, the segment length L_{seg} is a phenomenological parameter in the size range of the bend persistence length (for more details see the following section). Several examples of bend persistence lengths are given in Table 1.6. In comparison to these values, common polymers such as polyethylene can be described with persistence lengths of less than 1 nm. Therefore, the stiffer biopolymers such as DNA or fibrous proteins of the cytoskeleton are also called *semiflexible polymers*. The high persistence length of these biopolymers is one essential advantage for their application as building blocks for manufacturing microscopic machine systems or as templates for electronic circuitries.

The bend persistence length provides also a measure for Young's modulus E of the polymer chain. When we describe the polymer chain as a continuous isotropic elastic material, the bend persistence length can be expressed as

$$A = \frac{EI}{k_B T}. \tag{1.4}$$

As derived in Appendix B, here I is the second moment of inertia of the cross section,

$$I = \iint_{\text{cross section}} y^2 \, \mathrm{d}x\mathrm{d}y, \tag{1.5}$$

where y is the distance perpendicular to the neutral axis and $dxdy$ is an area element of the cross section. For a cylindrical wire with radius r, we get $I_{\text{cylinder}} = (\pi/4)r^4$ (for other shapes see solution of Task 1.3). Equation (1.4) shows that the bend persistence length decreases with decreasing fiber radius and increasing temperature.

1.2.2
Equilibrium Shape of a Semiflexible Polymer Chain

Let us now address in more detail the problem of the equilibrium shape of a biopolymer chain under the influence of thermal fluctuations in a solution. We are interested in a mesoscopic description of the polymer geometry. The contour length L should be much larger than the bend persistence length. Thus, we can idealize the polymer as a chain of perfectly straight segments of length L_{seg} connected by perfectly free links (FJC model). The segments, whose number is L/L_{seg}, are assumed to be randomly arranged along the chain. In the freely jointed chain model, the orientation of the segment i does not depend on the orientation of segments $i-1$ and $i+1$. As expected, like the path of a random walker, the polymer shows a coiled equilibrium shape for large numbers of segments. The diameter of the coil can be defined as the average end-to-end distance of the chain (see Figure 1.33).

For the FJC model, we can express the mean square value of that distance as

$$\begin{aligned}\langle \vec{R}\cdot\vec{R}\rangle = \sum_{i,j=1}^{N}\langle L_{\text{seg}}\vec{t}_i \cdot L_{\text{seg}}\vec{t}_j\rangle &= L_{\text{seg}}^2\left(\sum_{i=1}^{N}\vec{t}_i^{\,2} + 2\sum_{i<j=1}^{N}\vec{t}_i\cdot\vec{t}_j\right) = N(L_{\text{seg}}^2)\\ &= L_{\text{seg}}L_{\text{tot}}. \end{aligned} \tag{1.6}$$

The coil diameter of the semiflexible biopolymer D_{coil} scales with the square root of its length:

$$D_{\text{coil}} \approx L_{\text{seg}}^{1/2}L_{\text{tot}}^{1/2}. \tag{1.7}$$

The value for the segment length can be related to the bend persistence length by comparing the result of the FJC model with calculations using the WLC model. For the worm-like chain model, the mean square distance is given as

$$\langle \vec{R}\cdot\vec{R}\rangle = \left\langle \int_0^{L_{\text{tot}}}\vec{t}(s)\mathrm{d}s\int_0^{L_{\text{tot}}}\vec{t}(s')\mathrm{d}s'\right\rangle = \int_0^{L_{\text{tot}}}\mathrm{d}s\int_0^{L_{\text{tot}}}\mathrm{d}s'\langle\vec{t}(s)\vec{t}(s')\rangle, \tag{1.8}$$

where the correlation function $\langle\vec{t}(s_1)\vec{t}(s_2)\rangle \equiv f(s_1,s_2)$ is governed by the elastic interaction of neighboring segments. For positions well away from the ends of the chain, the orientation correlation function depends only on the distance along the contour of the chain, $\Delta s_{12} = |s_1 - s_2|$; hence, $\langle\vec{t}(s_1)\vec{t}(s_2)\rangle = f(\Delta s_{12})$. The function $f(\Delta s_{12})$ has to fulfill two conditions describing the strong correlation for short distance, $f(\Delta s_{12}) \to 1$ with $\Delta s_{12} \to 0$, and the missing of any correlation for very

large distances, $f(\Delta s_{12}) \to 0$ with $\Delta s_{12} \to \infty$. The orientation changes along different segments of the polymer chain due to thermal fluctuations are statistically independent. When we consider a sequence of three points on the chain, 1, 2, and 3, with $\Delta s_{13} = \Delta s_{12} + \Delta s_{23}$, then the free enthalpy change connected with the orientation change along the segment, Δs_{12}, is not involved in the free enthalpy change of the following segment. This means that the thermal average of the orientation correlation can be written as

$$f(\Delta s_{1s} + \Delta s_{23}) = f(\Delta s_{12}) f(\Delta s_{23}). \tag{1.9}$$

The only function that fulfils this relation is $f(\Delta s) = \exp(q\Delta s)$. The unknown parameter q can be determined evaluating the elastic energy of a chain segment with help of the principle of equipartition of energy in thermal equilibrium (Nelson, 2008). It leads to an exponential decay of the correlation function

$$\langle \vec{t}\,(s)\vec{t}\,(0)\rangle_{\mathrm{WLC}} = \exp(-|s|/A), \tag{1.10}$$

where the decay length is given by the persistence length A.

Evaluation of the integral in Eq. (1.8) now gives for large polymer length $L_{\mathrm{tot}}/A \gg 1$:

$$\langle \vec{R} \cdot \vec{R} \rangle = \int_0^{L_{\mathrm{tot}}} \mathrm{d}s \int_0^{L_{\mathrm{tot}}} \mathrm{d}s' \exp(-|s - s'|/A) = 2 \int_0^{L_{\mathrm{tot}}} \mathrm{d}s \int_s^{L_{\mathrm{tot}}} \mathrm{d}s' \exp(-(s' - s)/A) \cong 2AL_{\mathrm{tot}}. \tag{1.11}$$

This means, the diameter D_{coil} of the coiled molecule can be expressed as

$$D_{\mathrm{coil}} \approx (2A)^{1/2} L_{\mathrm{tot}}^{1/2}. \tag{1.12}$$

By comparing the results of the freely jointed chain model and the worm-like chain model, it appears that they coincide if the effective segment length is chosen twice the bending persistence length: $L_{\mathrm{seg}} = 2A$.

1.2.3
The Load–Extension Diagram of a Semiflexible Polymer Chain

Basic Phenomena As explained in the previous section, the equilibrium shape of a long semiflexible biopolymer chain is a random coil. Therefore, untangling a DNA coil by stretching it with the aim to deposit it on a substrate as a long straight molecule would require an external force, f, pulling at the ends. One has to overcome the elastic entropic force caused by the thermal motion of the molecule. Force–displacement measurements on individual DNA molecules can be measured by means of subtle experimental setups (Smith *et al.*, 1992; Cluzel *et al.*, 1996; Clausen-Schaumann *et al.*, 2000; Bockelmann *et al.*, 2002; Günther *et al.*, 2010). Soft microneedles, atomic force microscopes (AFMs), and optical and magnetic tweezers have been used for this purpose. In optical or magnetic tweezers, one end of the molecule is bound at a dielectric or a superparamagnetic microbead, whereas the other end is fixed on a substrate. The load needed to characterize the deformation

behavior of a single DNA covers a wide range, from the sub-pN regime of entropic forces acting in coiled molecules up to the rupture force of overstretched molecules in the range of about 600–800 pN. A high stiffness of loading device (relatively to the base pair stiffness) and high load resolution are needed. For instance, in measurements of unzipping a single double-stranded DNA molecule, the molecular stiffness is in the range of $k_{\mathrm{dsDNA}} = 0.01\,\mathrm{pN/nm}$. The stiffness of soft microneedles is typically in the range of $k_{\mathrm{microneedle}} = 0.001 - 0.002\,\mathrm{pN/nm}$, whereas in an optical trap for silica beads of 1 μm diameter in H_2O with a laser power $P = 700\,\mathrm{mW}$, a stiffness $k_{\mathrm{trap}} = 0.25\,\mathrm{pN/nm}$ has been measured (Bockelmann *et al.*, 2002). Spring constants of atomic force microscopes are about of 1000–10 000 times higher than those of optical tweezers. This means the compliances of optical traps or AFMs are almost negligible compared to the molecular compliance.

In an optical tweezers system, the force caused by the displacement of the dielectric bead in a highly localized electric field of a focused laser beam increases with increasing field gradient (increasing laser power). Therefore, a broad force range can be realized. The system allows a full 3D manipulation during loading. Compared to magnetic tweezers, one restriction is given by the missing option of torque application. Another limitation follows from possible radiation damage of the biomolecule at higher laser power.

In magnetic tweezers, the superparamagnetic bead is pulled by an external magnetic field. As the loading system can act in parallel on many molecules, parallel single-molecule experiments can be performed. One interesting feature of magnetic tweezers is the magnetic polarization anisotropy of the microspheres. Therefore, by rotation of the external magnetic field with respect to the substrate, in addition to a stretching force also a torque is caused. Thus, in addition to the stretching elasticity, the torsional stiffness of molecules can be measured (Kauert *et al.*, 2011). However, the missing option of a true 3D manipulation causes a limited applicability for magnetic tweezers.

In Figure 1.35, an experimental setup of force–displacement measurement using magnetic tweezers is shown schematically. The loading system allows covering of a large force range with high resolution. One example for a sensitive load–displacement measurement at low force is shown in Figure 1.35a. Günther *et al.* (2010) addressed the question, how much the mechanical and structural properties of DNA are changed by staining with YOYO-1, a widely used fluorescent dye for DNA. In the figure, the influence of the binding of YOYO-1 on the force–extension curve of DNA is shown. From fits of the experimental data to the WLC model, it was concluded that the persistence length of DNA remains constant independent of the amount of bound YOYO-1. Furthermore, the size of YOYO binding sites at the DNA (3.2 ± 0.6 bp/dye) and the elongation of the DNA per intercalated YOYO-1 molecule (1.6 ± 0.4 bp/dye) were derived from the experimental data. Upon binding of one YOYO molecule, the DNA untwisting is found to be $24^\circ \pm 8^\circ$. This is in line with values for other intercalators such as ethidium bromide, for which a value of 26° has been reported. These results demonstrate the manifold information that can be derived from mechanical single-molecule experiments for characterization of molecular interactions. In Figure 1.35b, another example is

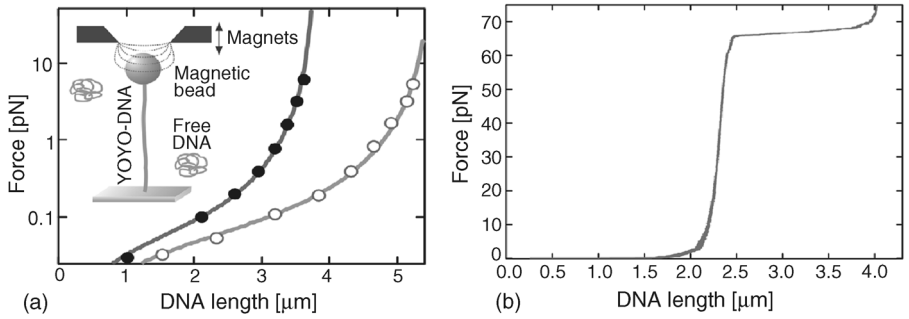

Figure 1.35 Force–extension measurements on double-stranded DNA by magnetic tweezers. (a) Force–extension curves of native DNA (filled circles) and YOYO–DNA (empty circles) at 1.4 dye/bp with fits to the WLC model (solid lines) providing persistence lengths of 54 ± 3 and 56 ± 3 nm and contour lengths of $3.82 \pm 0.01\,\mu m$ and $5.56 \pm 0.02\,\mu m$, respectively. *Inset*: Sketch of the experimental setup (Günther, Mertig, and Seidel, 2010). (b) Overstretching of a 6.6 kb long DNA. (Courtesy of Daniel Klaue and Ralf Seidel.)

given showing the overstretching of a double-stranded DNA (6.6 kb long) at a high tensile load.

From the above-mentioned extensive studies of the mechanical behavior of single DNA molecules, the general structure of the force–displacement curves of double-stranded DNA has been derived as shown in Figure 1.36. At very low stretching forces of 2–3 pN, the double-stranded DNA is stretched to about 90% of its contour length in the B-form. This range is governed by the entropy change from the random coiled shape to a nearly straight molecule. The higher tensile stiffness of the nearly

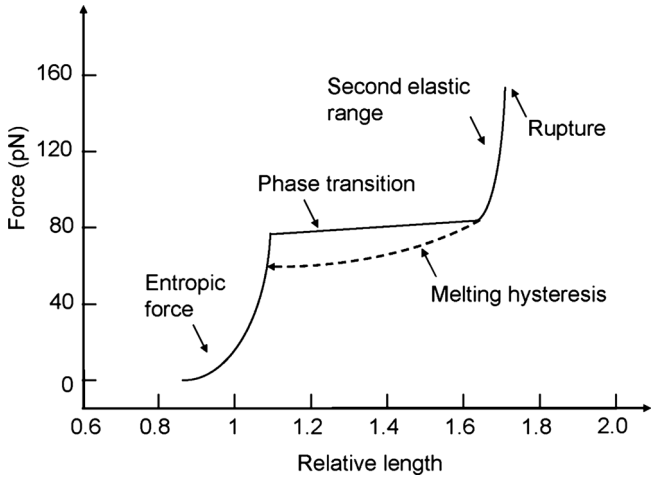

Figure 1.36 Characteristic ranges of the force–displacement diagram of λ-DNA molecules loaded with pulling velocities of about 1–10 μm/s. The displacement is plotted as the relative length normalized to the contour length of 16.3 μm. The first 10 μm of the displacement is not shown because it is indistinguishable from background noise.

straight molecule is represented by the steep slope. At about 65 pN, a remarkable increase of length is observed to about 1.6 of the contour length. Originally, this jump was explained by a reversible transition from the B-form DNA to an S-form DNA. Molecular modeling studies have shown that the DNA can form an overstretched ladder-like structure, the S-form. The S-form can be stretched elastically until rupture. Additional information can be obtained by recording the response to unloading by reversal of the extension rate. Hysteresis loops, as the one schematically indicated in Figure 1.36, bear witness to the presence of nonelastic components in the stress–strain behavior of the molecule.

A possible explanation of the hysteresis loop has been given by Smith *et al.*, (1996). It has to be assumed that along a double-stranded DNA there can be point-like defects, so-called nicks, at one of the two strands (Figure 1.37). These are overstressed regions under tensile load. At some critical tension, dsDNA undergoes an overstretching transition connected with partial melting. Recently, Bosaeus *et al.* (2012) have shown by experiments with small 60–64 bp DNA that, if the AT content is high (about 70%), an irreversible rupture including hysteresis is observed. However, GC-rich sequences (about 60%) undergo a reversible overstretching transition into the S-form. Furthermore, the transition depends on salt concentration. Low salt concentration (5 mM NaCl) lowers the stability of dsDNA and favors the irreversible transition. If the overstretched dsDNA remains in low-salt buffer for

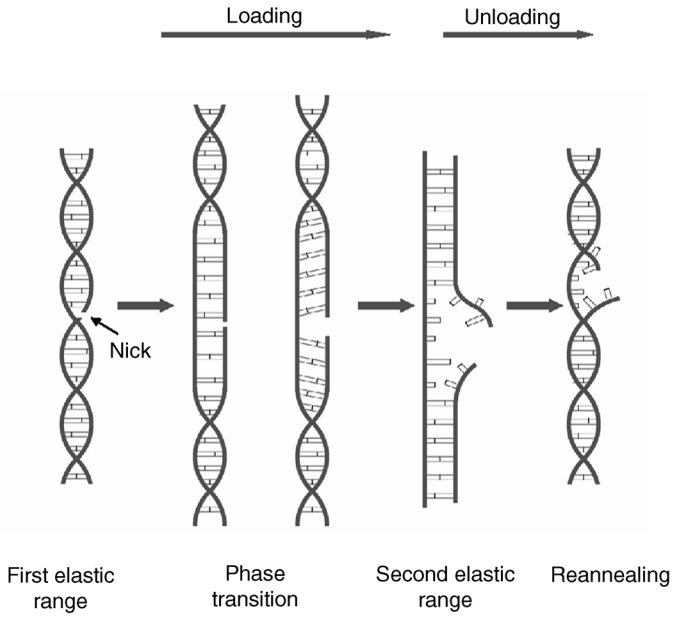

Figure 1.37 While yielding under tensile load, dsDNA may get into an overstretched state with a "skewed ladder" pattern in the presence of a nick in one of the strands. After unloading, the regions that have remained base paired rapidly contract to B-DNA but the frayed regions take several minutes to reanneal. (Adapted from Smith *et al.* (1996).)

more than a few seconds, then a nicked strand melts and frays back from both sides of the nick. When the tension is released, the regions that have remained base paired rapidly contract to B-DNA but the frayed regions take several minutes to reanneal, perhaps due to secondary structure in the frayed strands. As shown by Clausen-Schaumann *et al.* (2000), melting can also be observed in a defect-free S-DNA. With further stretching of the S-DNA, the double helix melts into single strands. These parallelly arranged strands can be loaded without fracture up to 800 pN. With subsequent unloading, the double helix is restored. Whereas the cooperative B–S transition is not rate-dependent, melting and reannealing are. The observed transition rate of reannealing in the unloaded state is about $(10–20) \times 10^3$ bp/s. The rate-dependence of melting and reannealing reveals itself as a rate-dependent hysteresis.

Basic Models The extension of a coiled molecule under the action of an external force f can be described in the simplest approximation with a one-dimensional FJC model (Nelson, 2008). In order to extend the force-free model discussed in the previous section, we first consider a one-dimensional version that will be generalized subsequently for 3D. We describe the molecule as a chain of N segments of length $L_{\text{seg}} = 2A$. Let an external force f act in the x-direction on a coiled molecule. One end of the chain is fixed at $x = 0$. The mechanical work required for a displacement Δx of the other end of the molecule is $\Delta A_{\text{ext}} = f\Delta x$. It contributes to a decrease of the free enthalpy $\Delta G^{\dagger}$ of the molecule with loading system by $\Delta G^{\dagger} = -T\Delta S - \Delta A_{\text{ext}}$. Every segment i of the chain can be displaced by thermal fluctuations with a certain probability forward or backward, denoted here by a two-state variable, $\sigma_i = +1$ and $\sigma_i = -1$, respectively. The resulting shift of the free end is given by

$$x = L_{seg} \sum_{i=1}^{N} \sigma_i. \tag{1.13}$$

One set of state variables $\{\sigma_1, \ldots, \sigma_N\}$ describes a particular realization of the stretched chain due to the thermal fluctuations. Its probability in the presence of an external force f is given by

$$p(\sigma_1, \ldots, \sigma_N) = Z^{-1} \exp\left(-\left(-f L_{\text{seg}} \sum_{i=1}^{N} \sigma_i \right) / k_{\text{B}} T \right),$$

with

$$Z = \sum_{\sigma_1 = \pm 1} \cdots \sum_{\sigma_N = \pm 1} \exp\left(\left(f L_{\text{seg}} \sum_{i=1}^{N} \sigma_i \right) / k_{\text{B}} T \right). \tag{1.14}$$

The mean displacement of the free end is given by the average of Eq. (1.13) over all conformations $\{\sigma_1, \ldots, \sigma_N\}$:

$$\langle x \rangle = L_{\text{seg}} \sum_{\sigma_1 = \pm 1} \cdots \sum_{\sigma_N = \pm 1} p(\sigma_1, \ldots, \sigma_N) \sum_{i=1}^{N} \sigma_i. \tag{1.15}$$

As $p(\sigma_1, \ldots, \sigma_N)$ is a product of N identical factors, this expression can be evaluated in a straightforward way (Nelson, 2008), which leads to

$$\langle x \rangle = N L_{\text{seg}} \frac{\exp(f L_{\text{seg}}/k_{\text{B}}T) - \exp(-f L_{\text{seg}}/k_{\text{B}}T)}{\exp(f L_{\text{seg}}/k_{\text{B}}T) + \exp(-f L_{\text{seg}}/k_{\text{B}}T)} = L_{\text{tot}} \tanh(f L_{\text{seg}}/k_{\text{B}}T). \quad (1.16)$$

For small load $f L_{\text{seg}}/k_{\text{B}}T \ll 1$, we get from Eq. (1.16) a linear load–extension relation

$$f = \frac{k_{\text{B}}T}{L_{\text{seg}}} \frac{\langle x \rangle}{L_{\text{tot}}}. \quad (1.17)$$

At low extension, the polymer shows linear elasticity (Hooke's law). The so-called entropic elasticity is characterized by a temperature-dependent effective stiffness $k_{\text{B}}T/L_{\text{seg}}$. For large force or low temperature, the FJC approximation leads to a completely parallel orientation of the single elements:

$$\lim_{f \to \infty} \langle x \rangle = L_{\text{tot}}. \quad (1.18)$$

In the case of large forces where the tensile stiffness $k_{\text{B}}TB$ of the polymer segments becomes relevant, the FJC model of rigid rod segments is no more applicable. The tensile deformation u_{ten} of every element of the chain is $u_{\text{ten}} = f/k_{\text{B}}TB$. This can be simply included in Eq. (1.16):

$$\langle x \rangle = L_{\text{tot}} \left(1 + \frac{f}{k_{\text{B}}TB}\right) \tanh(f L_{\text{seg}}/k_{\text{B}}T), \quad (1.19)$$

where L_{tot} is the contour length of the unloaded polymer. Unlike Eq. (1.16), this equation does not yield a maximum extension but a continuing linear increase.

Equations (1.16) and (1.19) are rough approximations to reality. In order to obtain more realistic theoretical constructs for the overall load–extension relation, the statistic average over all possible orientations of the molecular segments in three dimensions has to be taken into account. The most serious drawback of the FJC model is the assumption of free rotation of the elements of length L_{seg} around the points at which they are assumed to be linked. It is obvious that the shape change of a coiled molecule under load depends also on the bending stiffness of the elements. This has been taken into account by a refined model, the worm-like chain model (Bustamante *et al.*, 1994; Marko and Siggia, 1995). Here, the interaction with adjoining elements has been included by adding the bending energy to the external work. As another modification, the bend persistence length A is substituted for the free parameter L_{seg} of the FJC model (Bustamante *et al.*, 1994). The comparison with experimental data shows that the FJC model describes the elastic behavior of DNA at low extension well (Smith *et al.*, 1992). For larger extension, the tensile deformation has been included in the WLC approach by Odijk (1995). A modified version of the WLC model allows a fairly good description of the load–extension behavior of the double-stranded DNA over the complete range including the elastic entropic force as well as the contributions of the bending energy and the tensile energy (Wang *et al.*, 1997). The corresponding analytical expressions of the mentioned models are compiled in Table 1.7.

Table 1.7 Load–extension models for semiflexible polymer chains.

Model	Formula	Reference
FJC; entropic/tensile strain theory	$\varepsilon = \left(\coth\left(\frac{2fA}{k_B T}\right) - \frac{k_B T}{2fA}\right)\left(1 + \frac{f}{k_B TB}\right)$	Smith *et al.* (1996)
WLC; entropic theory	$f = \left(\frac{k_B T}{A}\right)\left(\frac{1}{4(1-\varepsilon)^2} - \frac{1}{4} + \varepsilon\right)$	Marko and Siggia (1995)
WLC; entropic/ tensile strain theory	$\varepsilon = 1 - \frac{1}{2}\left(\frac{k_B T}{fA}\right)^{1/2} + \frac{f}{k_B TB}$	Odijk (1995)
WLC; entropic/ tensile strain theory	$f = \left(\frac{k_B T}{A}\right)\left(\frac{1}{4(1-\varepsilon+f/k_B TB)^2} - \frac{1}{4} + \varepsilon - \frac{f}{k_B TB}\right)$	Wang *et al.* (1997)

Adapted with permission from Wang *et al.* (1997). Copyright 1997, Elsevier.
$\varepsilon = \langle x \rangle / L_{tot}$ relative extension; $k_B TB$ = tensile stiffness.

1.2.4 Cooperativity

Cooperativity occurs in living organisms on all structural levels, beginning with cooperative configuration changes of single macromolecules. The function of hemoglobin already mentioned in Section 1.1.2 as an oxygen binding protein is an example for cooperative binding. Binding of one oxygen at a specific binding site causes the whole tetrameric protein to switch into a well-defined second conformation for binding more oxygens ($n \approx 3$). From this conformation change effected by the binding of one ligand, proteins with such property have got the designation "allosteric proteins," derived from Greek *allos* meaning "other" and *stereos* meaning "shape." Moreover, the affinity of hemoglobin to oxygen can be modulated by binding dissolved carbon dioxide: The related structure change always leads to an accelerated release of oxygen, when it is most needed. Many kinds of allosteric proteins have been formed in evolution to enable cooperative coupling mechanisms as modulating elements of life processes. Another example for cooperativity is the sudden softening of a double-stranded DNA under tensile loading when the load exceeds about 65 pN (Figure 1.36). The overstretching transition from the B-configuration to the S-configuration with an extension by 70% is the result of the cooperative change of the stacking of the base pairs along the DNA chain.

Generally, cooperativity concerns coordinated conformation changes of weakly interacting elements in biopolymers. There are cases where the interacting elements are in close vicinity, but in other cases they are far apart. Cooperative motion of distant subunits is coordinated by signal transmission. However, as we will see in other examples to be discussed later, the structure transitions can be caused also by a change of the temperature or the chemical environment (pH change, for instance). Therefore, it should be possible to describe the phenomenon cooperativity in a more

general language. For this purpose, we follow the concept of the famous Ising model of magnetism. Similar to the orientation of magnetic moments in a solid body, we assume that a single structure element i of the biopolymer can occupy discrete energy states $E_i = -\alpha k_B T \sigma_i$. In the previous section, we considered the one-dimensional FJC model with the two states $\sigma_i = \pm 1$. The noninteracting segments L_{seg} can occupy the two energy states $E_i = \pm f L_{seg}$ with their displacement parallel or antiparallel to the direction of the acting external load ($\alpha = f L_{seg}/k_B T$). Cooperativity implies the presence of an interaction energy of adjoining elements:

$$U_{int} = -\gamma k_B T \sum_{i=1}^{N-1} \sigma_i \sigma_{i+1}. \tag{1.20}$$

Hence, adjoining elements with equal orientation, $\sigma_i = \sigma_{i+1}$, contribute a negative amount of energy, $U_{int} = -\gamma k_B T$. Correspondingly, adjoining elements with unequal orientation contribute a positive amount. γ is the so-called cooperativity parameter, which expresses the coupling strength. Extending the FJC model derived above for the average displacement of a stretched one-dimensional chain by adding the interaction energy U_{int} yields a generalized version of Eq. (1.16):

$$\langle x \rangle = N L_{seg} \frac{\sinh \alpha + \left(\sinh \alpha \cosh \alpha / \sqrt{\sinh^2 \alpha + e^{-4\gamma}} \right)}{\cosh \alpha + \sqrt{\sinh^2 \alpha + e^{-4\gamma}}}, \tag{1.21}$$

with $\alpha = f L_{seg}/k_B T$ (Nelson, 2008) (see also Figure 1.38). For small values of the cooperativity parameter, $\gamma \to 0$, Eq. (1.21) reduces to the simple FJC equation (1.16), whereas for strong coupling, $\gamma \to \infty$, we get a step-like jump from $x = 0$ (coiled DNA) to a straight molecule with the load-independent contour length $\langle x \rangle = N L_{seg} = L_{tot}$. The increase of the extension with increasing cooperative interaction can also be seen when we consider the limit case of Eq. (1.21) at low external force:

$$f = \frac{k_B T}{e^{2\gamma} L_{seg}} \frac{\langle x \rangle}{L_{tot}}. \tag{1.22}$$

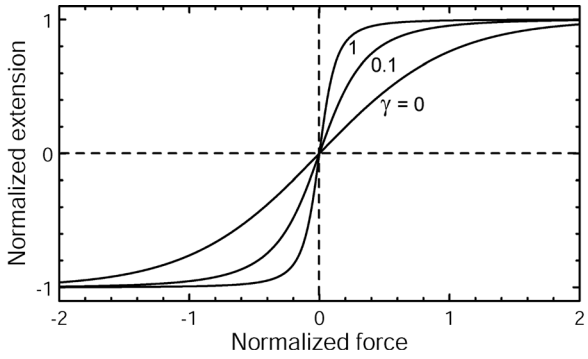

Figure 1.38 Cooperative FJC model. Change of normalized extension $\langle x \rangle / L_{tot}$ in dependence on normalized force $\alpha = f L_{seg}/k_B T$ for various values of the cooperativity parameter γ.

This means the effective "spring constant" of the coil decreases with increasing γ. For larger γ, the transition from the coiled molecule to the straight one is sharper.

1.2.5 Protein Folding

The Levinthal's Paradox and Stable Secondary Structures In order to understand the process of protein folding in more detail, we will reconsider some experimental findings. What is the characteristic timescale to create a functional protein? The time needed to form a functional protein of about 100 amino acids in *E. coli* is typically in the range of 5 s at 37 °C. If we try to explain this process as a random sequential arrangement of all the amino acids of the molecular chain, we come to a paradox first stated by Cyrus Levinthal in 1968. Let us assume that every amino acid residue can realize four different conformations. Then the number of all possible conformations of the protein is $4^{100} \approx 1.6 \times 10^{60}$. This simple rough estimate shows that the real process of protein folding must occur highly parallelly and hierarchically. Obviously, the protein folding cannot be random. Probably in the evolutionary selection process such molecular structures have dominated which developed a kind of cooperativity that favors the formation of stable subunits. From the thermodynamics point of view, folding is a competition between two forces, a driving force due to the decrease of the enthalpy caused by the increasing number of noncovalent bonds (for characteristic interaction energies see also Table 1.8) and a retarding entropic force favoring the randomly coiled chain structure.

The noncovalent weak interactions are larger than the thermal fluctuations by about a factor of 10 (see Table 1.8). Therefore, enthalpy-driven ($\Delta H < 0$) folding of proteins in small stable subunits of a few nanometers in size can occur at room temperature. The retarding contribution of entropy reduction ($T\Delta S < 0$) is about 1–2 kcal/mol for side chains of amino acids. However, this is overcompensated by the many new bonds between the large numbers of amino acids. All together, at room temperature, folding of protein leads to a decrease of the free enthalpy $\Delta G = \Delta H - T\Delta S < 0$. The decrease of the free enthalpy ΔG is in the range of about 4–10 kcal/mol. This value is so large that the folded structure is stabilized with respect to thermal fluctuations at room temperature T_r with $k_B T_r = 0.6$ kcal/mol.

Table 1.8 Interactions that stabilize proteins.

Interaction	Binding energy (kcal/mol)
Covalent bonds	>50
Dispersion forces	<1
Hydrogen bonds	1–7
Electrostatic interaction (low dielectric)	1–6
Hydrophobic interaction	2–3
Average thermal energy (37 °C)	0.6

As we have learned in Section 1.1.2 from the Pauling and Corey arguments, folding of a peptide chain yields *α-helices and β-sheets as stable secondary structures*. The further process is an ongoing compaction of the structure by interaction of the secondary structures. This produces domains of interacting α-helices and β-sheets, which finally leads to the *tertiary structure* of the protein. Up to now, there is no complete theory that can describe the whole process in all details. Folding can be explained only by the interplay of the weak, noncovalent interactions. Whereas the covalent binding along the backbone stabilizes the open-chain structure, noncovalent interactions between the side chains favor a more compact arrangement of the chain. Hydrogen bonds between the main chain groups of the amino acid residues as well as short-range interaction of the side chain groups control the final arrangement of the secondary structure. There are two alternative models explaining main features of the experimental observations. In one of the models, it is supposed that *long-range weak interactions* between the secondary structures direct the formation of the domain structures. Another model favors the assumption that *hydrophobic interactions* cause a spontaneous collapse of the open-chain structure into the so-called *molten globule state*. The existence of hydrophobic regions along the protein chain is the reason why these regions avoid the contact with the aqueous solution in the equilibrium structure. However, the molten globule state cannot be a highly compact state. The side chains of the single amino acid residues are responsible for a self-avoidance of chain segments similar to the self-avoidance of molecules in a real gas described with a finite radius of single atoms. Locally, secondary structures could be formed in the globule (collapsed) state of the protein. It has to be assumed that features of both models can be observed experimentally.

Banavar *et al*. (2004) have shown that the experimentally observed typical ternary folding structures can be simulated already under fairly general assumptions about the protein structure and interaction. They described a homopolymer chain in a continuum approach as a tube of length L and thickness Δ with a range of attractive interaction R. In a Monte Carlo simulation, the thermodynamic equilibrium at zero temperature has been calculated. Elastic bending energy, overall hydrophobic energy, and effective hydrogen bond energy of interacting chain segments have been included in the interaction modeling. A phase diagram of the tubes has been derived, representing the various phases depending on the two parameter ratios Δ/R and L/R (Figure 1.39).

In the limit of large L/R, the model provides two phases. For large Δ/R, a swollen phase with equal weight for all self-avoiding configurations of single tubes is obtained. The possible conformations are essentially equivalent with respect to energy. For large L/R and small Δ/R, a semicrystalline phase with packages of stretched parallel tubes is found. Every stack of tubes is surrounded by six other stacks parallel to each other in a hexagonal array, similar to the nematic phase of liquid crystals (see also Section 7.2.6). For small L/R and small Δ/R, a featureless phase of compact coils is obtained, whereas for thick fibers again the swollen random conformations governed by self-avoiding and elastic energy are favored. Most interesting is the existence of a *marginally compact phase* near the triple point at

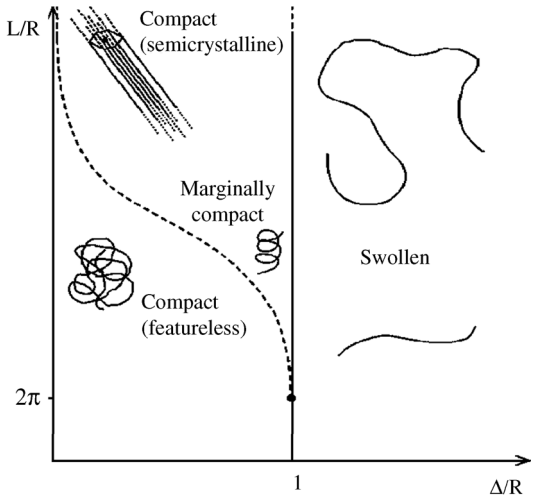

Figure 1.39 Zero-temperature phase diagram of self-attracting tubes depending on the tube length/interaction range ratio L/R and the tube thickness/interaction range ratio Δ/R. (Reprinted with permission from Banavar *et al.* (2004). Copyright 2004, the American Physical Society.)

$\Delta \approx R < L$. In this phase, a *limited number of structures of the discrete homopolymer chains* is obtained: helices, kissing hairpins, regular hairpins, and sheets, with energetic differences among them. The marginally compact phase is sensitive with respect to parameter changes. A slight increase of temperature causes a first-order transition to the featureless compact phase.

Examples of the marginally compact structures are shown in Figure 1.40. These are the results of various modeling runs with a homopolymer of 48 amino acids. The effective range of interaction R was chosen nearly equal to the tube radius, $\Delta/R \approx 1$. Depending on the initially open shape of the chain and the variation of the energy parameters, the simulation led to a limited number of equilibrium configurations.

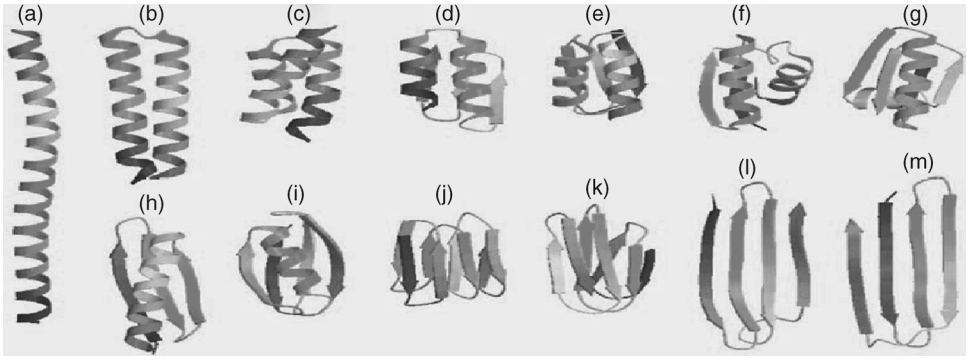

Figure 1.40 A sampling of conformations of a homopolymer modeled as a marginally compact tube of 48 residues. All structures are compositions of helices and strands. (Reprinted with permission from Hoang *et al.* (2006). Copyright 2006, IOP Publishing Ltd.)

This simulation reflects the two characteristic features of marginally compact tube structures. First, they are always composed of stacks of α-helices and β-sheets. Second, the number of different conformations is much smaller than the number of possible random arrangements of the chain. The calculated conformations show a striking similarity to experimentally observed secondary polypeptide structures. The Monte Carlo simulation time yields also reasonable estimates of the real overall folding time.

Universal Features of Protein Folding The good agreement between the results of model calculations for protein folding and the experimentally observed results leads to the conclusion that the folding of protein chains follows a few rules:

- There are common structural features of globular proteins, the marginally compact structures composed of assemblages of α-helices and β-sheets, as dominating secondary structures.
- The marginally compact structures are phases of minimum free enthalpy of nanometer-sized subunits. The proteins fold reproducibly into the marginally compact structures.
- There exist only a few thousand marginally compact states. The overall tertiary structure of a globular protein shows a pronounced stability with respect to minor changes of the amino acid sequence of the protein chain. This is a favorable precondition for a stable, so-called neutral evolution, which means that the *majority of mutations are not causing essential changes of the phenotype* (Lezon, Banavar, and Maritan, 2006). The formation of life based on the DNA–RNA–protein cycle is relatively stable with respect to mutations of the DNA.
- The folding process proceeds along a series of metastable transition states that are also characterized by assemblages of marginally compact structures of α-helices and β-sheets. The transition can be described in a conformation space as a motion on a *funnel-like energy landscape* along the steep gradient to the minimum of free enthalpy.
- As folding is a cooperative process of local formation of domains of separate α-helices and β-sheets, it proceeds in fractions of a second. Quick and reproducible folding of proteins is a necessary precondition for effective physiological function.
- The tertiary structure of the globular protein composed of well-defined domains of α-helices and β-sheets generates well-defined sites at its periphery for interaction with other proteins and other molecular entities. This is the base for *specificity* as well as *diversity*, two properties essential for the molecular processes of life. Proteins are well suited for molecular *recognition* and *selection*.

Chaperones as an Additional Tool Box for Directed Protein Folding Chaperones are proteins that interact with only partially folded polypeptides. They assist the folding in the cell in order to direct the folding evolution through the diversity of possible transition states on an optimal path toward the minimum of free enthalpy. They can create microenvironments to facilitate the folding or to correct improperly folded intermediate protein structures. Different kinds of chaperones are available:

- Small containers with hydrophobic interior, called chaperonins, create a temporary hydrophobic environment shielding the protein from contact with interfering cell components and facilitate a well-defined folding.

- The proteins of Hsp70 family (Hsp, heat shock proteins) bind temporarily to regions of unfolded polypeptides that are rich in hydrophobic residues in order to avoid inappropriate aggregation.
- The protein disulfide isomerase (PDI) breaks incorrect cross-links of cysteine amino acids that could fix the folding in an unfavored conformation.
- The peptide prolyl *cis–trans* isomerase (PPI) puts the proline into one of the two possible conformations, which allows a correct fit into the folded protein chain.

The chaperones are essential tools of the self-assembly process, directing and accelerating the whole process of folding.

As discussed above, the helical structure is distinguished among all other protein structures by its particular stability. There is a mechanism called helix–coil transition that facilitates the transition between the two conformations with changing temperature. The helical configuration is stable at low or at high temperatures in water or organic solvents, respectively. The transition can be observed by optical polarization measurements on the translucent protein solution. Circular dichroism (CD) spectroscopy enables sensitive measurements of changes of the secondary structure of proteins (for more details see Appendix C). The chirality of helical molecules affects their interaction with circularly polarized light: The refractive index, n, and the molar extinction coefficient, ε, of solutions of helical polypeptides or proteins differ for left and right circularly polarized light, which is known as circular birefringence (CB) ($n_L \neq n_R$) and circular dichroism ($\varepsilon_L(\lambda) \neq \varepsilon_R(\lambda)$). The latter transforms linearly polarized light into elliptically polarized light. The major axis of the ellipse is tilted by an angle ϕ with respect to the incident linearly polarized light. The *ellipticity* is due to differential absorbance of circularly polarized light by the chiral molecules, whereas the tilt angle ϕ is due to the differential phase velocities (for details see Appendix C). These effects are suitable for monitoring helix–coil transitions of polypeptides and proteins.

As an example, the CD spectra of short alanine-based peptides in aqueous solution at 0 °C (Scholtz *et al.*, 1991) are shown in Figure 1.41a. The molar ellipticity $[\theta]$ is a measure for the ellipse axis ratio. Peptides with the generic formula Ac-Y(AEAAKA)$_n$F-NH$_2$ (A: L-alanine; E: L-glutamic acid; K: L-lysine; flanked by an N-terminal acetyltyrsoine and a C-terminal phenylalanyl carboxamide) have been studied. The spectra correspond to chain lengths of 50, 38, 32, 26, 20, and 14 residues, reading from the lower curve at 222 nm to the upper curve. The wavelength region between 210 and 220 nm, which corresponds to the absorption band of peptide bond, yields the main information concerning the length dependence of the helix–coil transition. The measured ellipticity can be converted into fractional helicity of the peptides. This conversion requires the knowledge of $[\theta]_{222}$ for the completely helical and completely coiled configurations (Scholtz *et al.*, 1991). From the observed temperature dependence of the ellipticity, the temperature dependence of the helix–coil transition can be derived as shown in Figure 1.41b. The data show that with increasing peptide length the transition occurs at higher temperature and with a steeper slope. This indicates the increasing cooperativity of the transition with increasing peptide length.

As usual, the driving force for the conformation change is the loss of free enthalpy in the process: $\Delta G = G_{\text{helix}} - G_{\text{coil}} = \Delta H_{\text{bond}} - T\Delta S_{\text{tot}}$, where ΔH_{bond}

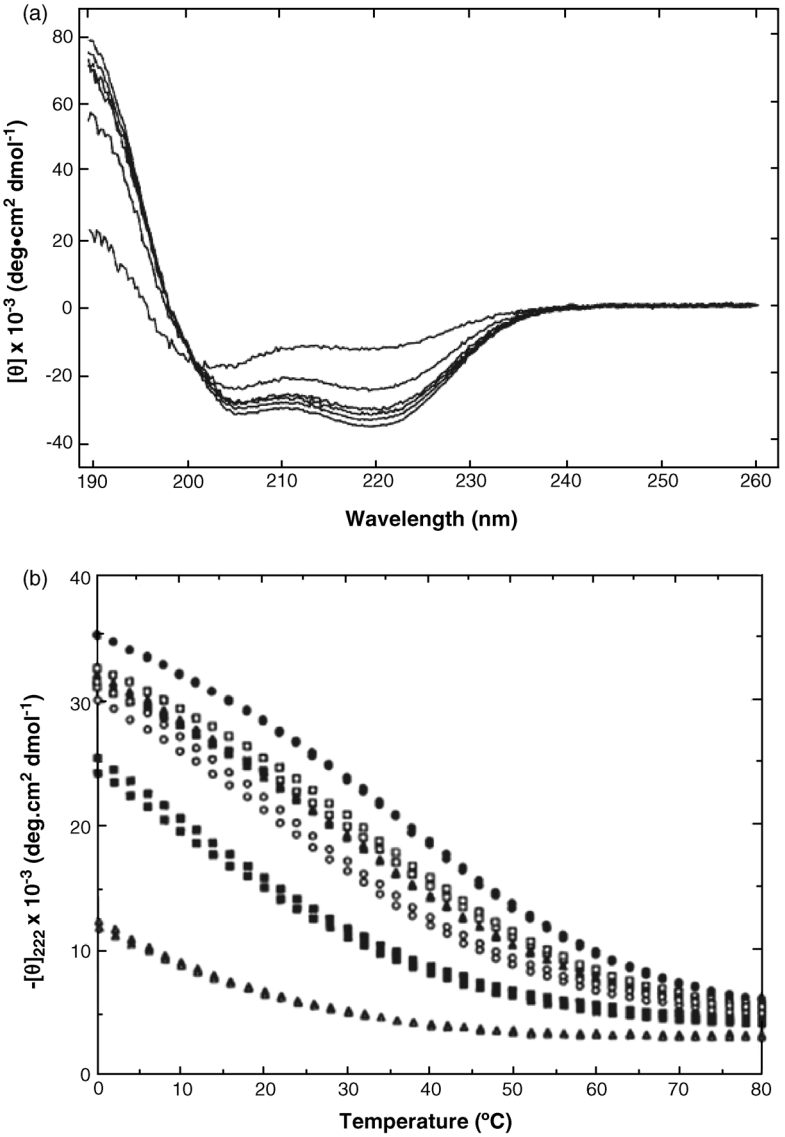

Figure 1.41 α-Helix formation in water versus temperature for short alanine-based peptides. (a) CD spectra of six peptides with chain lengths of 50, 38, 32, 26, 20, and 14 residues, reading from the lower curve to the upper curve, at 222 nm. (b) Thermal unfolding curves of the peptides monitored by CD. The differences between the two curves for every peptide are due to the uncertainty of measurement. Curves are shown for peptides with chain lengths of 50, 38, 32, 26, 20, and 14 residues reading from the upper to the lower curve. (Reproduced with permission from Scholtz *et al.* (1991). Copyright 1991, John Wiley & Sons, Inc.)

and ΔS_{tot} denote the change of the enthalpy and the entropy of the total system consisting of the polypeptide and the solvent. According to Section 1.1.2, an α-helix can be formed by hydrogen bonds between the oxygen atom in the carbonyl group of the ith amino acid and the hydrogen atom in the amide group of the $(i+4)$th amino acid of the polypeptide chain (Figure 1.15). The $(i, i+3)$ spacing of the Glu and Lys residues was selected by Scholtz *et al.* (1991) because side chain interactions are minimal when compared to the $(i, i+4)$ arrangements of Glu and Lys residues. The experiment was meant to be an example for helix–coil transitions associated with the polypeptide backbone and minimal side chain interactions.

From the observation that the helical conformation is stable in aqueous solution at low temperature, we can conclude that $\Delta H_{bond} = H_{helix} - H_{coil} < 0$ should be valid. For the change of the entropy $\Delta S_{tot} = S_{helix} - S_{coil}$, we can assume that there is always a negative contribution of the configuration entropy $\Delta S_{conf} < 0$ due to the limited degree of freedom of the monomers in the α-helix. Furthermore, the degree of freedom of the water molecules is restricted next to the helix–solvent interface. This causes a decrease of the entropy of the surrounding solvent molecules, $\Delta S_{solvent} < 0$, when extended helical structures are formed. Since the total entropy change is negative, $\Delta S_{tot} = \Delta S_{conf} + \Delta S_{sovlent} < 0$, there is a transition temperature $T_m = \Delta H_{bond}/\Delta S_{tot}$ beyond which the free enthalpy change ΔG becomes positive. Hence, the coiled configuration is the favored equilibrium structure above this critical temperature.

The driving force for the formation of the helical structure can be expressed by a parameter $\alpha \equiv (\Delta H_{bond} - T\Delta S_{tot})/(-2k_B T)$. Positive α means that the formation of the α-helix is thermodynamically favored. Its growth by one unit leads to a decrease of the free enthalpy by $\Delta G = -2\alpha k_B T$. For the evaluation of experimental data, it is useful to express α by ΔH_{bond} and the transition temperature $T_m \equiv \Delta H_{bond}/\Delta S_{tot}$ (often also called midpoint temperature) with

$$\alpha = \frac{1}{2}\frac{|\Delta H_{bond}|(T_m - T)}{k_B T T_m}. \tag{1.23}$$

The formation of a first bond between the ith and $(i+4)$th amino acid of the polypeptide always leads to some interaction with the neighboring amino acids of the yet coiled positions. This means the cooperativity of the transition has to be included into an extended model. Again we apply the description of the cooperativity, which we have already discussed for the modified FJC model of the load–extension behavior of polymer chains. The binding state of the amino acid at position i is characterized by a state parameter σ_i with $\sigma_i = +1$ for the helix structure and $\sigma_i = -1$ for the coiled structure. For the change of free enthalpy due to formation of a single hydrogen bond, we get $-(2\alpha - 4\gamma)k_B T$, where γ describes the mismatch interaction between neighboring bonded and nonbonded amino acids. A detailed statistical evaluation of the equilibrium distribution yields the average value for the state variable along the polypeptide (Nelson, 2008):

$$\langle\sigma\rangle = \frac{\sinh\alpha}{\sqrt{\sinh^2\alpha + e^{-4\gamma}}}. \tag{1.24}$$

With increasing cooperativity (large γ), the transition becomes sharper. The comparison with the experimental data shows that the molar ellipticity of the scattered light can be described in good approximation by a linear function of the average state variable, $-[\theta]_{222} = c_1 + c_2\langle\sigma\rangle$.

1.2.6 DNA Melting Transition

As already reported in Section 1.1.1, aqueous solutions of double-stranded DNA are stable at pH 7.0 and room temperature (25 °C). A temperature increase above 80 °C causes the viscosity of the solution to drop sharply and the UV absorption (typically recorded at 260 nm) to increase as a result of a reversible structural transition into two single-stranded molecules, known as melting or denaturation. This reversible transition is very similar to the helix–coil transition of polypeptides. The UV absorption characteristic can be derived from the thermodynamic equilibrium of a cooperative two-stage system as given in Eq. (1.24). Also in this case, weak hydrogen bonds (between the complementary bases) are responsible for the helix stability. The helix is the stable phase at low temperature. When DNA melts, the hydrogen bonds between the bases break. At the same time, the disruption of the base stacks is connected with loss of favorable van der Waals attraction and dipole–dipole interactions. The gain of energy due to reduced Coulomb interaction of the negatively charged backbones is smaller than the energy increase of the above-mentioned interactions. Thus, the total change of the enthalpy is positive, $\Delta H_{\text{bond}} = H_{\text{melt}} - H_{\text{helix}} > 0$, during melting. The overall entropy also increases, $\Delta S_{\text{tot}} > 0$. When the two DNA strands are separated, the screening ion clouds around the DNA can relax. The increasing flexibility of the backbones is connected with an increase of the configurational entropy. Furthermore, the unstacked base configurations contribute to this increase. An opposite contribution is caused by exposing hydrophobic regions of the DNA to the surrounding water.

In summary, we get a similar temperature dependence for the free enthalpy change $\Delta G = \Delta H_{\text{bond}} - T\Delta S_{\text{tot}}$ as for the helix–coil transition of proteins, with the disordered phase at high temperature and the ordered phase at low temperature. Therefore, DNA melting is sometimes called a helix–coil transition. For partially molten DNA, the transition region between double-stranded segments and separated strands is connected with an additional interaction energy that leads to the cooperativity discussed above. This explains the sharpness of the melting transition. A higher content of G–C pairs with three hydrogen bonds in comparison to A–T pairs with two hydrogen bonds leads to a higher melting temperature due to the increase of ΔH_{bond} (Nelson and Cox, 2008). By changing the pH value and the ionic strength, the repulsive electrostatic interaction can be influenced, and therewith also the melting temperature.

1.2.7 Biocatalytic Reactions

Biocatalysts, also called enzymes, mediate the chemical transformations of organic substances inside and outside living cells. The influence of biocatalysis on digestion

of food in the stomach has been explored already in the late 1700s. In the 1850s, the fermentation of sugar into alcohol by yeast cells led Louis Pasteur to the assumption that biocatalytic processes are always connected with living cells, a theory known as vitalism. Soon it was found that biocatalytic processes can also occur outside a living cell. (The term *ferment* is restricted to enzymes acting in living organisms.) Many functional proteins and some nucleic acids act as enzymes. Today, enzymes are widely used in food processing, brewing industry, paper industry, textile industry, biofuel industry, drug development, medicine, and molecular biotechnology. The principles that these applications are based on are potentially useful for other novel developments too.

The Reaction Transition State Model In 1946, Linus Pauling formulated a general model of the biocatalytic process based on the concept of *reaction transition states*, first proposed by Michael Polanyi in 1921 and John Haldane in 1930 (Haldane 1930). For simplicity, we consider a reaction where a substrate phase S is transformed by a chemical reaction into a product phase P. The reaction can be described by a reaction diagram.

The driving force for the reaction can be expressed by the difference of the free enthalpy between the S phase and the P phase, ΔG, with

$$\Delta G = \Delta G^0 + RT \ln\left(\frac{[\mathrm{P}]}{[\mathrm{S}]}\right). \tag{1.25}$$

Here R is the molar gas constant (8.315 J/mol), and [P] and [S] are the concentrations of the product and substrate phases, respectively. For negative $\Delta G^0 < 0$, the product phase is favored in thermodynamic equilibrium $\Delta G = 0$:

$$K_{\mathrm{eq}} = \exp\left(-\frac{\Delta G^0}{RT}\right) = \frac{[\mathrm{P}]_{\mathrm{eq}}}{[\mathrm{S}]_{\mathrm{eq}}} > 1, \tag{1.26}$$

where K_{eq} is the equilibrium constant of the reaction $\mathrm{S} \leftrightarrow \mathrm{P}$. The rate V of any unimolecular reaction $\mathrm{S} \rightarrow \mathrm{P}$ is determined by the product of rate constant k and substrate concentration $V = k[\mathrm{S}]$. Usually a noncatalyzed biochemical reaction is suppressed near room temperature for a long time, as the system has to overcome an activation barrier $\Delta G_{\mathrm{uncat}}$. For the rate constant k, the transition state theory yields

$$k = \frac{k_{\mathrm{B}} T}{h} \exp\left(-\frac{\Delta G_{\mathrm{uncat}}}{RT}\right), \tag{1.27}$$

where k_{B} is the Boltzmann constant and h is the Planck constant (see also Task 1.5).

In the presence of an enzyme, the reaction rate is much higher. This must be due to a lower activation barrier in the presence of the enzyme E interacting with the substrate S and the product P. These interactions are included into the formalism by introducing metastable transition states ES and EP (see Figure 1.42), which allows the reaction to be separated into a sequence of thermally activated reactions: $\mathrm{E} + \mathrm{S} \rightarrow \mathrm{ES} \rightarrow \mathrm{EP} \rightarrow \mathrm{E} + \mathrm{P}$. The binding energies between the enzyme E and the transient species ES and EP are the decisive parameters as they lower the activation barrier by $\Delta G_{\mathrm{B}} = \Delta G_{\mathrm{uncat}} - \Delta G_{\mathrm{cat}}$. Site-specific catalytic groups of

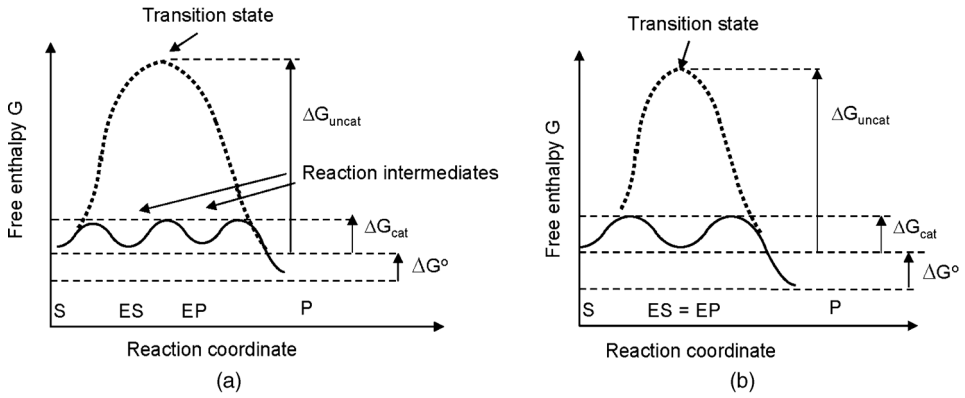

Figure 1.42 Reaction coordinate diagrams. Change of the free enthalpy in an uncatalyzed (dotted line) and catalyzed (full line) reaction in dependence on a reaction coordinate. S and P denote the ground states of the substrate and the product phase, respectively. ES and EP denote less stable intermediate phases of the enzyme-catalyzed reaction (a). Often in a simplified model only one intermediate phase can be assumed to describe a catalytic reaction path (b). This assumption has been used in the Michaelis–Menten model. (Adapted from Nelson and Cox (2008).)

the enzyme, such as amino acid residues, can form transient covalent bonds with the substrate and product phases. In addition, noncovalent bonds, such as hydrogen bonds or hydrophobic and ionic interactions between substrate and enzyme, lower the activation barrier. Some enzymes need additional nonprotein molecules called *cofactors* to be active. These can be inorganic components such as metal ions (e.g., Fe^{2+}, Mg^{2+}, Mn^{2+}, and Zn^{2+}) or *coenzymes*. Coenzymes are small organic groups that transport chemical groups from one enzyme to another. Important examples are NADH (nicotinamide adenine dinucleotide), which provides electrons for reactions in the respiratory chain, and ATP (adenosine triphosphate), which acts as an energy carrier by phosphate ion transfer.

The substrate and the enzyme change their structure during the formation of the intermediate phases ES and EP to realize the energetically optimized reaction path. This differs from the action of inorganic catalysts, and it explains the high efficiency of biocatalysts. Initially, it had been assumed that already a perfect fit between the substrate and the enzyme would explain the high efficiency of the reactions. Such a "lock and key" model explains the high specificity of the enzymatic reaction but not the *existence of a stable transition state*. The latter can be explained by a refined lock and key model taking into account the ability of the enzyme to reshape itself continually during the reaction. In the "induced fit" model, it is assumed that the conformation of subunits is changed during the reaction to provide precise fit with the changing substrate. For an intended use of enzymes as components for biohybrid materials, care has to be taken that the necessary freedom for structural relaxation is not lost by the immobilization or entrapment of the enzyme on or in the carrier material. For accelerating the reaction by a factor of 10, $\Delta G_B = 5.7\,\mathrm{kJ/mol}$ is required. The energy contribution of a single weak bond is typically in the range of

4–30 kJ/mol. Therefore, multiple noncovalent interactions will be sufficient to lower the activation barrier by 60–100 kJ/mol. This explains why the reaction rate can be increased with enzymes by 10^5–10^{17} times, which demonstrates the huge potential of enzymes for biochemical engineering.

Enzyme Kinetics It would be highly desirable to evaluate the efficiency of an enzyme by a straightforward experiment. Of particular interest are the probability of transient sticking of the substrate at the enzyme and the maximum turnover rate k_{cat} of the whole process. Stimulated by first studies of Henry in 1903, Michaelis and Menten proposed in 1913 a useful scheme for the evaluation of the kinetics of catalytic reactions. With some simplifying assumptions on the process, an equation can be derived that describes the relation between the reaction velocity of a one-substrate enzyme-catalyzed reaction and the substrate concentration. The beauty of this approach is the possibility to derive the above-mentioned intrinsic enzyme properties in a simple way. Michaelis and Menten have considered the simplest case of the reaction with only one transient state ES (see Figure 1.42):

$$\mathrm{E} + \mathrm{S} \underset{k_{-1}}{\overset{k_1}{\rightleftharpoons}} \mathrm{ES} \underset{k_{-2}}{\overset{k_2}{\rightleftharpoons}} \mathrm{E} + \mathrm{P}. \tag{1.28}$$

The prerequisite of the model is that only the early stage of the reaction is considered. This means it can be assumed that the concentration [P] of the product phase is small. Therefore, any back reaction can be neglected ($k_{-2} = 0$). Furthermore, it is assumed that the concentration [S] of the substrate is large with respect to the total enzyme concentration $[\mathrm{E_{tot}}]$. In the initial stage, changes of the substrate concentration are negligible in the total reaction balance. Under these assumptions, a reaction rate equation for the transient state can be formulated with [ES] as the concentration of the transient phase ES:

$$\frac{\mathrm{d}}{\mathrm{d}t}[\mathrm{ES}] = k_1[\mathrm{S}]([\mathrm{E_{tot}}] - [\mathrm{ES}]) - (k_{-1} + k_2)[\mathrm{ES}]. \tag{1.29}$$

Here $[\mathrm{E_{tot}}] - [\mathrm{ES}]$ is the concentration of the free (or unbound) enzyme. With the initial condition $[\mathrm{ES}](t = 0) = 0$ and the assumption $[\mathrm{S}] = \mathrm{const}$, it leads to a very simple solution:

$$[\mathrm{ES}](t) = (1 - \exp(-\lambda t))[\mathrm{ES}]_{\mathrm{st}},$$

with

$$\lambda = k_1(K_\mathrm{m} + [\mathrm{S}]) \quad \text{and} \quad [\mathrm{ES}]_{\mathrm{st}} = \frac{[\mathrm{E_{tot}}][\mathrm{S}]}{K_\mathrm{m} + [\mathrm{S}]}. \tag{1.30}$$

Here K_m is the *Michaelis constant*:

$$K_\mathrm{m} = \frac{k_{-1} + k_2}{k_1}. \tag{1.31}$$

The solution is limited to the early part of the reaction only (see also Figure 1.43). As we see, at very short time (for $t \ll \lambda^{-1}$) there is a linear increase of the occupation of the transition state. The slope increases for higher substrate concentration. For

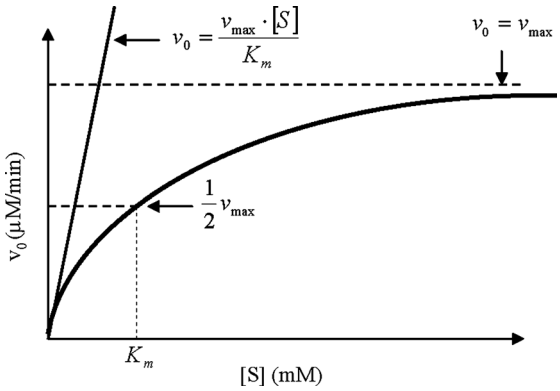

Figure 1.43 The Michaelis–Menten model of enzyme kinetics: the Michaelis–Menten plot. The kinetic parameters can be determined from the asymptotic behavior at low and high substrate concentrations.

longer time, saturation is reached with a stationary value $[ES]_{st}$ for the concentration of the transient phase. This *quasi-steady state* is considered by Michaelis and Menten in their further evaluation. In the quasi-steady state, the reaction velocity v_0 of the product phase is given as

$$v_0 = k_2[E]_{st} = v_{max}\frac{[S]}{K_m + [S]} \quad \text{with} \quad v_{max} = k_2[E_{tot}]. \tag{1.32}$$

This *Michaelis–Menten rule* expresses the saturation value of the reaction velocity of the enzyme in the early stage of the reaction depending on the concentrations of the substrate [S] and the enzyme $[E_{tot}]$. v_{max} is the maximal reaction velocity. The maximum turnover number $v_{max}/[E_{tot}] = k_2$ characterizes the internal speed of a single enzyme molecule. The Michaelis constant K_m is a measure for the maximum occupation of the transition state of the enzyme:

$$\text{maximum}\left([ES]_{st}/[E_{tot}]\right) = K_m^{-1}. \tag{1.33}$$

A small value of the Michaelis constant corresponds to a high concentration of the transition phase. If the enzyme binds the substrate with a high rate in comparison to the catalysis rate k_2 and the substrate dissociation rate k_{-1}, then we observe a high occupation of the transition state. The Michaelis–Menten model characterizing the early stage of the catalytic reaction allows a universal description of the dependence of the product rate v_0 on the substrate concentration, [S], if the two phenomenological fitting parameters v_{max} and K_m are known (Figure 1.43). The evaluation of the product rate allows a straightforward determination of these parameters by rewriting the Michaelis–Menten equation in the form of the so-called Lineweaver–Burk equation:

$$\frac{1}{v_0} = \frac{K_m}{v_{max}[S]} + \frac{1}{v_{max}}. \tag{1.34}$$

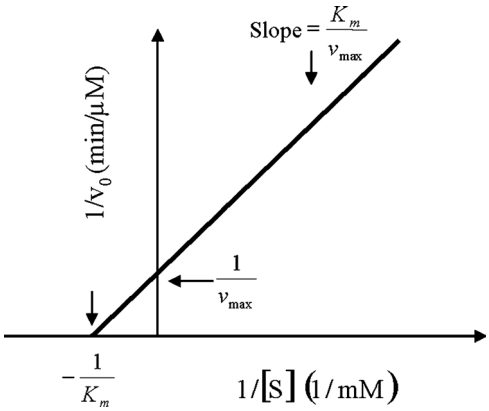

Figure 1.44 The Michaelis–Menten model of enzyme kinetics: the double-reciprocal Lineweaver–Burk plot.

The double reciprocal plot of $1/v_0$ versus $1/[S]$ plot is suitable for fitting experimental data. As one can see in Figure 1.44, the two intercepts on the $1/v_0$ axis and $1/[S]$ axis yield immediately $1/v_{max}$ and $-1/K_m$, respectively.

1.3 Bioengineering

1.3.1 Biointerfacing

Today, the study of biological interfaces with the aim to exploit them for the development of novel materials covers a wide range of sizes lasting from big orthopedic implants down to biofunctionalized nanowires or nanoclusters in advanced biosensors. Accordingly, the topic "biointerfacing of materials" includes a broad field of research activities. It concerns interfaces of artificial materials with (i) single biomolecules, (ii) cellular organelles, (iii) the extracellular matrix of tissue, and (iv) single cells or biofilms. For further discussion, we have a brief view on natural interfaces in biological systems.

Compartmentalization is an essential prerequisite for living systems to generate separate spaces for biochemical reactions. The cell as a whole and the various subcellular organelles of eukaryotic cells are surrounded by membranes, mostly based on lipid bilayers. Lipid bilayers are fluid – in the sense that the molecules can arrange and rearrange themselves more or less easily while staying inside the monolayer or bilayer – thus behaving like a two-dimensional liquid. The fluidity of a membrane mainly depends on the chemical nature of the lipids. Unsaturated lipids make membranes more fluid, while saturated ones and cholesterol have the opposite effect. In order to fulfill their main function of separation, biomembranes are impermeable to most molecules. Only small

lipophilic molecules are able to freely diffuse through the membrane. Transport of ions and hydrophilic molecules including water is strictly controlled by specific channels or transport proteins embedded in the membrane. Signal transduction is facilitated by membrane-anchored receptor proteins via binding of specific molecules.

Functionalization of technical surfaces with native biomembranes is extremely challenging because of their complex physical and chemical properties. Another level of complexity is added by the fact that cells permanently remodel the membrane composition according to their physiological needs. Technical surfaces of any chemical constitution will somehow interact with membrane components, and hence tend to produce artifacts. A possible solution to this dilemma is offered by cells whose cell membranes are covered with an additional layer, for example, the cell wall or surface layers, simple membranes that are mainly or exclusively composed of proteins. These rigid structures provide mechanical stability. At the same time, their porous structure allows the access of most molecules to the underlying cell membrane. *Bacteria and yeast cells may therefore be prime candidates* for the application of whole cells to technical devices (see also Chapter 4).

An alternative solution can be the use of the *extracellular matrix as a natural coupling medium* between the living cells and an artificial material. This is an option that has already been successfully used in many developments of biocompatible implants for regenerative therapy in medicine. For example, metallic or ceramic implants for bone surgery can be coated with collagen–hydroxyapatite composites that are the main components of the bone matrix. It is obvious that such coatings substitute the functions of a real bone matrix only to a limited degree. Therefore, it is intended to use cells of the surrounding tissue to rebuild such artificial coatings. With the incorporation of signal molecules, such as cytokines or growth factors, the basic interactions can be controlled (see also Chapter 6).

The sensitivity of the biomolecules with respect to their surroundings may cause serious problems in the case of direct coupling to an artificial material. As explained in Section 1.2, the functionality of proteins depends strongly on their correct folding, which is, for example, difficult to achieve at hydrophobic surfaces. Therefore, it is usually necessary to design multilayered coatings that provide "soft" transitions to the main material.

General Design Rules for Biointerfaces While the functionalization of technical devices with living cells is still in its infancy, a wide variety of methods has been developed to engineer surfaces with biomolecules. Some general rules have to be fulfilled for the successful preparation of biomimetic interfaces by using biomolecular building blocks.

- *Preservation of the native conformation:* The functionality of biomolecules depends strongly on their conformation in space. The molecular information stored in proteins, DNA, and polysaccharides can only be used if the molecules, assembled at an interface, have the conformational freedom as in their natural environment. This is only possible if the correct three-dimensional structure of a biomolecule is

retained during immobilization, which is a difficult challenge for highly complex biomolecules. The conformation of many of chain-like molecules is governed by weak noncovalent bonds. Therefore, uncontrolled adsorption of the biomolecules at surfaces can be critical. Unspecific adsorption can be avoided by an appropriate coating with hydrophilic polymer films such as poly(ethylene oxide) (PEO), leading to a "neutral interface". Hydrophobic molecules like integral constituents of membranes, such as ion channels, exhibit surface-exposed hydrophobic residues. Their native structure can only be attained and preserved in an appropriate *lipophilic environment*.

- *Site-specific binding and controlled patterning:* Usually, biofunctionalization of artificial materials aims at information transfer between living matter and an engineering component. In micro- or nanostructured hybrid constructs such as biosensors, microarrays, hybrid electronic circuitries, or implanted biomedical devices, the interface has to meet specific requirements. Key parameters are the density distribution of molecules which transfer the signals between the living system and the technical device, their uniformity, and often a controllable patterning of the interface. The natural length scale for structure control has to be in the range of a few nanometers, determined by the characteristic sizes of the biomolecular building units. This is preferably realized by *self-assembly* as it occurs in biological systems (see also Chapter 7).
- *Chemical compatibility:* From the chemical point of view, the organic interface has to be compatible with the multiple substrate materials such as silicon, silica, glasses, noble metal films, polystyrene, polydimethylsiloxane (PDMS), and various polymorphic carbon phases (graphite, diamond, and carbon nanotubes). In the case of incompatibility, a suitable transition layer has to be applied.
- *Thickness requirements:* For many sensor applications, such as various optical sensors (e.g., surface plasmon resonance (SPR) spectroscopy and interferometry), and electronic sensors (e.g., field-effect transistors), the highest sensitivity of the hybrid device is obtained with interfaces whose thickness does not exceed a few nanometers. There are other applications, such as whole-cell sensors, that require coatings of several μm thickness providing microcavities for the immobilization of living cells as well as a channel system communicating with a life-sustaining environment.
- *Reusability and regeneration:* Finally, aspects of cost efficiency also have to be considered, for instance, the option of reusability or regeneration of the biological interface in the case of biosensors.

In conclusion, one needs a high versatility of available processing options to meet the multiple demands regarding the design of biological interfaces. This design is based on a modular approach that uses biological components such as DNA, proteins, lipids, membranes, or whole cells as building blocks. To create a stable interface, different interaction mechanisms can be employed that can roughly be divided into *physical absorption*, *chemical binding*, and *bioaffinity interactions*. As explained in the following sections, there are various technological platforms available that can be applied for the purpose in question. In this chapter, we will

preferentially address solutions based on interfaces functionalized with DNA and proteins.

1.3.2 DNA-Based Nanotechnology

The use of DNA for the creation of new materials and processing techniques in nanotechnology has benefited from the rapid methodical progress in life sciences. Advances in high-throughput DNA sequence analysis and expression profiling resulted in the development of diverse techniques for fabrication of DNA microarrays. The biological self-assembly of nucleic acids has been one of the key mechanisms that motivated chemists, physicists, and materials scientists to work with DNA. Due to its restricted number of bases and their unique capability of self-recognition, it has been the most suitable molecule for demonstrating the feasibility of the "bottom-up approach" in the manufacturing of artificial nanostructures. Soon it was found that DNA and RNA are suitable as templates for building nanostructured surfaces of almost any kind of materials. This paved the way for application of DNA-assembled interfaces in materials engineering. The innovative potential of DNA is most obvious in two main areas: (i) biomolecular templates for submicrometer electronic circuitries, and (ii) programmable nanoprobes.

1.3.2.1 Biomolecular Templates for Submicrometer Electronic Circuitries

In 1965, Gordon Moore formulated an empirical observation in the so-called Moore's law that the market for silicon-based microelectronics is characterized by doubling the functionality (bits) per chip surface area every 18 months. Today, this empirical law is still valid in semiconductor industry. The large-scale production of such structures is still realized by using top-down lithography. The microstructures are "carved out" from bulk-like materials by applying sophisticated physical and chemical technologies, such as optical lithography, UV lithography, or electron beam and X-ray lithography. It can be expected that the top-down lithography will come to principal physical limits when the structure sizes will fall below 10 nm. For processing, it means that new technologies summarized as bottom-up approach are needed. Arrangement and interconnection of nanosized electronic components into a functional circuit have to be realized. It has to be processed in parallel with high reliability on a large scale of length (typically tens of micrometers). Therefore, recognition and self-assembly should be essential ingredients of these new techniques. Comparing these demands with the machinery inside living cells evokes the idea of implementing such objects in future nanoelectronic technology. One basic idea behind such developments is the use of DNA for self-assembling nanostructures. The specific base pair recognition, the charged phosphate groups along the backbone, and the existing options for conjugation with additional functional groups are the reasons why DNA can act as a programmable template for the formation of a nanostructured circuit. The whole process of biotemplating can be subdivided into four parts: preparation of the DNA for immobilization, end-specific immobilization, stretching of coiled DNA, and functionalization of DNA templates.

Preparation of DNA for Immobilization Stable immobilization of the ends of single- or double-stranded DNA (dsDNA) can be achieved by nonspecific physical binding (electrostatic or hydrophobic interactions), covalent binding, site-specific biomolecular interactions (bioaffinity), or physical embedding of DNA ends in coatings. Whereas physical embedding of the DNA molecule needs no further modification, for covalent binding and bioaffinity the DNA ends have to present specific linkers depending on the substrate chemistry. There are two basic ideas derived from natural DNA replication that can be applied for the end-specific functionalization of a dsDNA (Figure 1.45). During replication, each single strand of an unwound DNA double helix acts in the cell as a template for *immobilization of individual matching nucleotides*. Enzymes catalyze this process. It is possible to use this mechanism for *in vitro* polymerization of nucleotides at so-called single-stranded overhangs of a dsDNA. Figure 1.45a shows how DNA polymerase catalyzes the binding of deoxynucleotide triphosphates dATP, dCTP, dGTP, and dTTP at the sticky end of a dsDNA. In the example, the last nucleotide (dTTP) is functionalized with a reactive

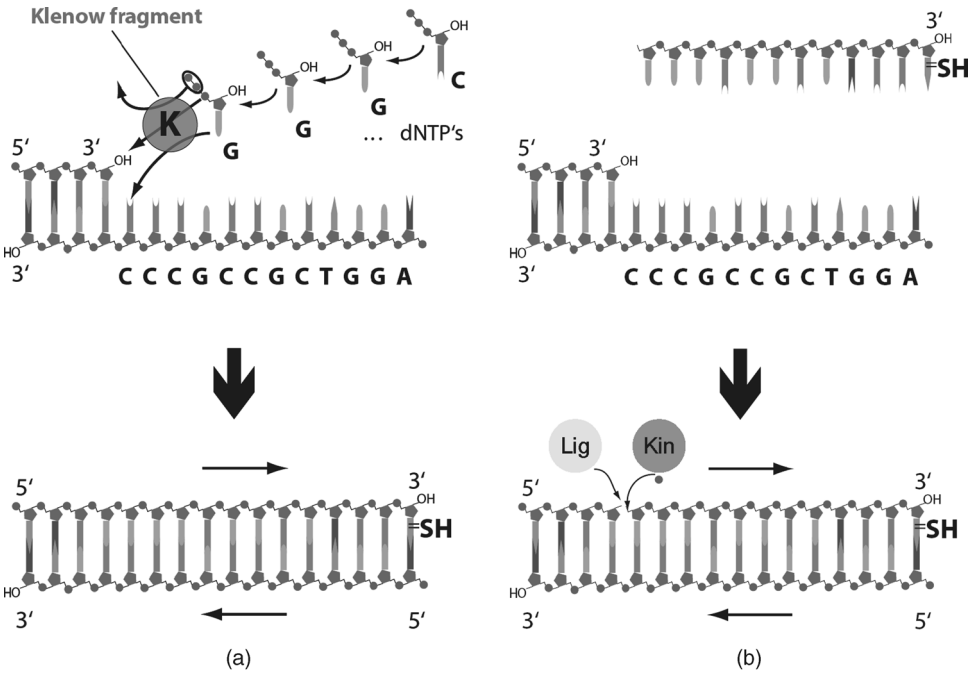

Figure 1.45 (a) Sticky-end functionalization. The exonuclease-free Klenow fragment of DNA polymerase incorporates the deoxynucleotide triphosphates dGTP, dCTP, and dATP and the thiol-modified S^4-TTP, resulting in a functionalized blunt end. (b) Hybridization of a thiol-modified oligomer to the sticky end of a λ-DNA. The single-stranded nick can be closed by a two-step process: phosphorylation of the OH-terminated 5′-end of the oligomer before hybridization using T4 kinase (Kin), and ligation after hybridization using T4 ligase (Lig).

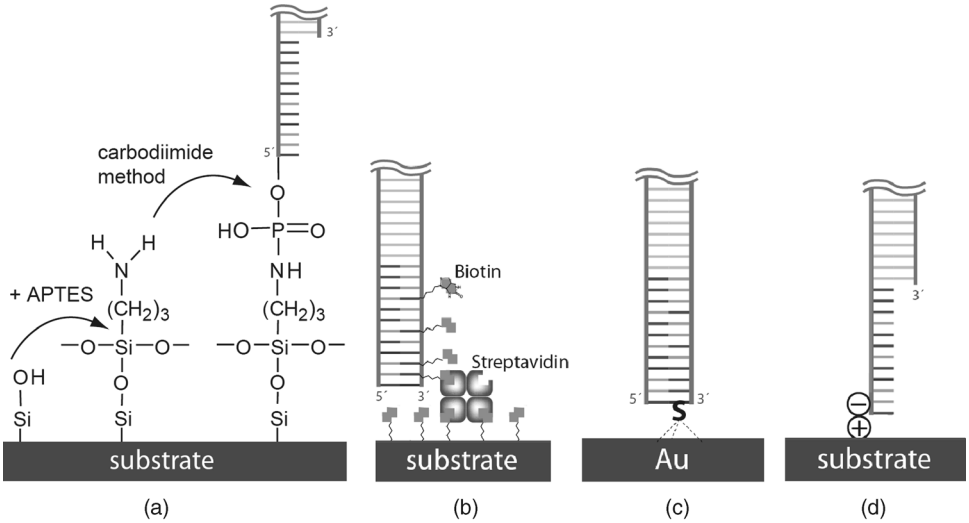

Figure 1.46 Different techniques for end-specific anchoring of DNA to surfaces: (a) At the DNA end, an activated phosphoester formed by the carbodiimide method is covalently coupled with a nucleophilic agent such as an amine formed by silanization to create a stable covalent bond. (b) Affinity reaction forming a streptavidin bridge between the biotinylated DNA end and a biotinylated surface. (c) Specific binding of thiol-functionalized DNA to a gold surface. (d) Electrostatic bonding between positively charged amino groups and twofold negatively charged DNA ends.

SH group. In this way, the blunt end of the dsDNA is modified to bind covalently to a gold surface. Other, often used reactive groups are the coenzyme biotin and the steroid digoxigenin. Alternatively, the sticky end can be filled with an already *functionalized complementary sticky end by hybridization* by means of the enzyme T4 kinase (Kin). Finally, the nick is closed by ligation by means of the enzyme T4 ligase (Lig).

End-Specific Immobilization The structure of DNA offers many possibilities for coupling to an inorganic material: the amines in the bases, the negatively charged backbone, the phosphodiesters within the backbone, the phosphate at the 5′-end, and the hydroxyl group at the 3′-end. The anchoring of a single end of DNA at a silica substrate or patterned gold contact is an elementary process step for the immobilization of DNA templates for microelectronic circuitries. Various techniques are available for this purpose (Figure 1.46). DNA can be bound covalently to reactive surface sites by various coupling reactions. Besides the NH_2 groups, other reactive groups on the DNA can be generated by activation reactions such as the carbodiimide or the activated ester method. On hydroxyl-terminated substrates such as silica or glass, *DNA can be covalently immobilized by silanization* of the substrate with reactive silanes. 3-Aminopropyltriethoxysilane (APTES), which provides an amino group for chemical reaction, is commonly applied for

silanization (Figure 1.46a). The amino group can be connected with an activated phosphoester of the DNA by reaction with carbodiimide. Covalent binding is the preferred technique for DNA immobilization owing to the high bond strength, optional high uniformity, and packing density of the oligonucleotides (provided they do not exceed ~20 bases). Other processing routes to covalent binding are summarized in Table 1.9.

Another approach makes use of *bioaffine coupling*: A biotinylated DNA is anchored to a biotinylated surface by means of a streptavidin bridge (Figure 1.46b). *Biotin and streptavidin* form one of the strongest natural bonds. Streptavidin and the closely related avidin are tetrameric proteins with four binding sites for biotin. Their bond strength to biotin depends on the loading rate. It varies between 5 pN for low loading rate and 170 pN for high loading rate.

The functionalization of gold contacts with oligonucleotides can be accomplished by applying *thiol chemistry* (Figure 1.46c). Thiol groups are used for chemical binding of biomolecules on metals such as gold, silver, platinum, or copper. On gold surfaces, each sulfur atom is coordinatively bonded with three gold atoms. The gold–sulfur bond ruptures at a force of about 1.4 nN (at a loading rate of 10 nN/s).

The fourth option is nonspecific physical binding via *electrostatic interaction* between a positively charged substrate surface (e.g., gold contacts functionalized with amino–thiol groups) and the twofold negatively charged end of the DNA (Figure 1.46d). This method demands an appropriate control of the pH and the ion concentration in the solution to prevent attraction of the whole DNA chain by the positively charged surface. To get preferential binding of the termini of the DNA, the charges should be partially shielded by an appropriate choice of the pH value (about pH 8–9).

As to be discussed in the following subsection, even *hydrophobic interaction* can be used for DNA adsorption on hydrophobic surfaces. In overstretched double-stranded DNA, disturbed hydrogen bonds between complementary bases cause hydrophobic interactions. This mechanism can be applied for transfering oriented stretched DNA on a substrate, which will be discussed in the following subsection. Finally, the immobilization of DNA in a hydrogel offers the possibility of depositing thicker DNA coatings on a substrate. This technique could be relevant if a higher effective surface density of the DNA probes is needed for higher sensitivity of a biosensor. The main processing routes developed for immobilization of DNA on various kinds of materials are compiled in Table 1.9. For more details see Festag *et al.* (2005).

Stretching of Coiled DNA The manufacturing of linear templates for microelectronic circuitries requires to align stretched molecules on the particular substrate. As explained in Section 1.2.3, the stress–strain curve of an individual DNA molecule shows an elastic range followed by an extended yield range where the molecule is stretched without being denatured. This permits the formation of well-aligned templates for nanowires. Various techniques for stretching and parallel alignment of DNA molecules are available: stretching of single molecules by atomic

Table 1.9 Immobilization mechanisms of DNA on solid surfaces.

Interaction	Surface modification	DNA modification	Remarks
Covalent binding		Depending on spacer head group	
Thiol chemistry	Gold substrate with thiol–spacer constructs: thiol–alkyl, multiple thiol anchor, steroid disulfide	Thiol modified	Consecutive probing possible
Amine chemistry	Gold substrate: amine/succinimide, maleimide; silica substrate: 3-aminopropyltriethoxysilane + 1,4-phenylene diisothiocyanate (PDC)	Amino modified	
Epoxy chemistry	Silica substrate with 3-glycidoxypropyltrimethoxysilane (GOPS)	Amino modified	High loading capacity, good uniformity
Bioaffinity interaction	Streptavidin; biotin/streptavidin double-layer S-layer/streptavidin	Biotinylated	High specific binding strength, high binding efficiency and uniformity
Electrostatic interaction	Amino groups	Control of effective charge of the negatively charged backbone	About pH 8–9
Hydrophobic interaction	Hydrophobic substrate	Partially denatured by stress, defects of H-bonds between nucleic acids	Relevant for molecular combing
3D nanoporous hydrogels	Silica substrate with GOPS		Higher loading capacity

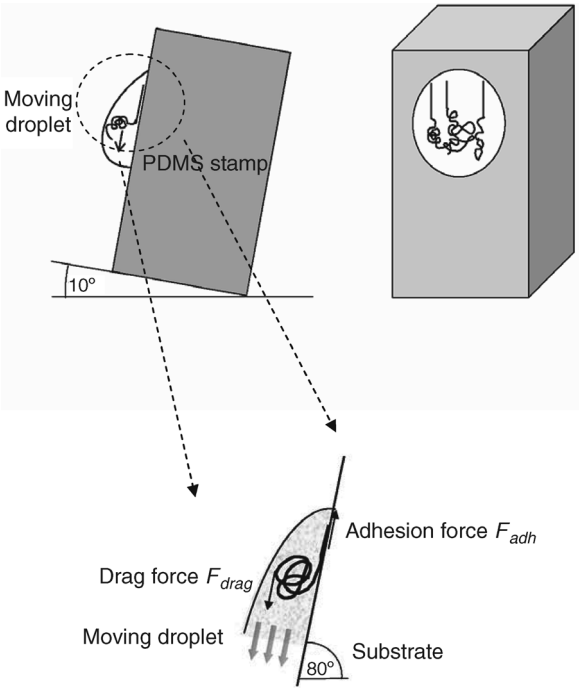

Figure 1.47 Principle of molecular combing with a moving droplet: Coiled DNA suspended in aqueous solution and stuck to the substrate with one end is stretched by the liquid flow.

force microscopy, optical and magnetic tweezers, or simultaneous alignment of many molecules by methods such as molecular combing, hydrodynamic flow, and electrophoretic stretching.

Molecular Combing The principle of molecular combing is depicted in Figure 1.47. A droplet of DNA solution is placed on the surface of a hydrophobic substrate in an inclined position such that it flows down. A favored substrate is polydimethylsiloxane. This hydrophobic polymer is well suited for the fabrication of stamps enabling the transfer of biomolecules. In order to become stretched by the drag of the liquid flow and adsorbed in the stretched conformation in parallel alignment, the molecules must be stuck to the substrate with one end. The process of parallel alignment of DNA on a substrate is called "molecular combing".

Random sticking can be controlled by the experimental conditions such as pH, the presence of additional cations, and the degree of hydrophobicity of the surface. Figure 1.48 shows the strong influence of the pH value, with the other parameters kept constant.

The sudden change of the aspect of the deposited DNA between pH 3 and pH 4 is due to a transition of the adsorption behavior. At pH 3 and pH 4, the DNA is adsorbed in a coiled shape, whereas beyond pH 4 the DNA is adsorbed at one end only, and then

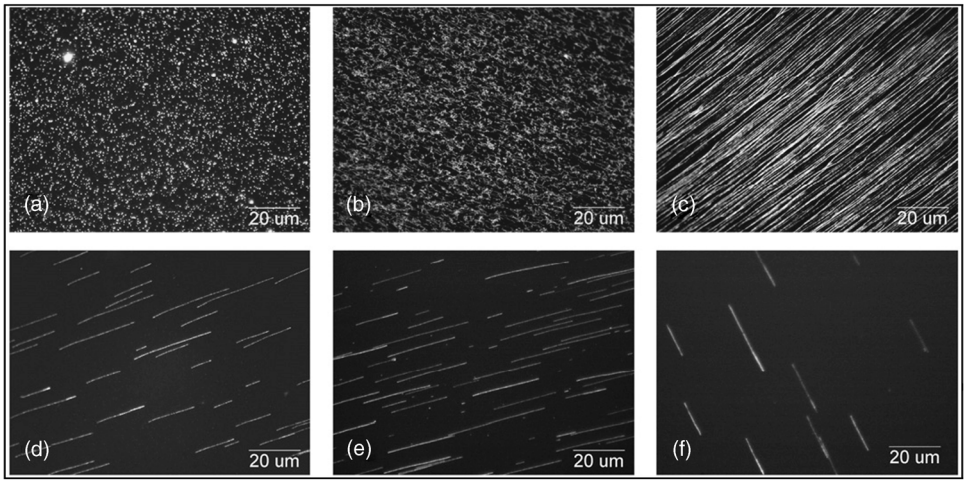

Figure 1.48 pH-dependent behavior of λ-DNA solution in molecular combing experiments on an hydrophobic PDMS surface ((a) pH 2, (b) pH 3, (c) pH 4, (d) pH 6.2, (e) pH 9, (f) pH 10). (Reproduced with permission from Benke *et al.* (2011). Copyright 2011, IOP Publishing Ltd.)

stretched and aligned in the direction of the moving droplet. The stretched molecules are longer than the contour length of λ-DNA, which is 16.2 μm. Apparently, the density of stretched molecules is highest at pH 4. The conspicuously changing behavior of the DNA as a function of pH in this experiment coincides with the change of the surface charge of PDMS. For high acidity, the surface is positively charged by preferential adsorption of hydronium ions (H_3O^+), whereas beyond pH 4 it is negatively charged through adsorbed hydroxide ions (OH^-). This property of PDMS explains why with high acidity the adhesion of coiled DNA molecules with their negatively charged phosphate backbone is so strong that the drag force of the liquid flow is not able to stretch them. In less acidic solutions, only the hydrophobic sticky ends of the dsDNA bind strongly to the substrate so that the coil can be stretched into a straight line. With higher pH, the sticking probability of the DNA is reduced by Coulomb repulsion between the DNA and the surface charge of the PDMS.

The double-stranded λ-DNA possesses 12 unpaired bases on its two single-stranded sticky ends that present hydrophobic binding sites to the PDMS substrate. With one of the sticky ends stuck to the substrate after incidental contact, the main part of the coiled molecule is dragged along by the moving liquid, whereby it becomes unraveled, stretched into straight shape, overstretched to lengths exceeding the contour length by factors of 1.6–2.1, and aligned in the direction of flow (Figure 1.49). Experiments with a controlled stationary flow (Brochard-Wyart, 1995) have shown that the stretching of DNA by the drag force occurs at flow velocities as low as 20 μm/s (see the following subsection). Hence, no "meniscus force" is required to explain the stretching. The overstretching of the natural B-DNA by the moving droplet exposes hidden hydrophobic binding sites that bind to the hydrophobic substrate. Thus, the overstretched DNA is stabilized on the PDMS stamp. On

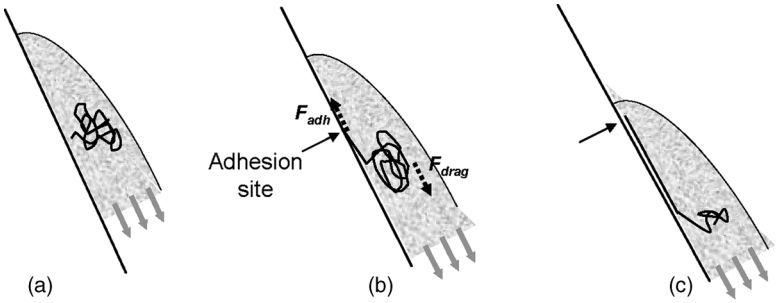

Figure 1.49 Molecular combing of DNA by means of a moving droplet: (a) DNA suspended in solution; (b) one end adhering; (c) partially stretched.

a hydrophilic substrate, such as a PDMS surface with 30° contact angle after treatment with plasma (air), the overstretched DNA relaxes to its contour length and becomes partially unstretched (Figure 1.50).

To sum up, the observed combing can be understood as a three-step process: (i) One end of the coiled DNA suspended in solution gets stuck to the substrate. (ii) The DNA is stretched while the coil becomes unraveled by the drag force of the liquid. (iii) The drag acting on the stretched B-DNA causes overstretching into the S-DNA form or partially molten DNA. After deposition of aligned DNA molecules at the stamp surface, they can be transferred by microcontact printing onto the final substrate. With an appropriate surface profile of the PDMS stamp, structured patterns of well-aligned DNA can be produced (Figure 1.51).

Superposition of DNA patterns can be realized by sequential printing (Figure 1.52).

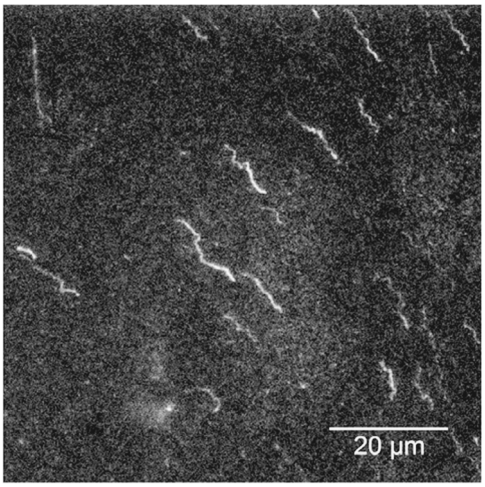

Figure 1.50 DNA relaxed after molecular combing and adsorption on a hydrophilic surface. Adsorption of DNA molecules has been done on plasma-treated hydrophilic PDMS. (Reproduced with permission from Benke *et al.* (2011). Copyright 2011, IOP Publishing Ltd.)

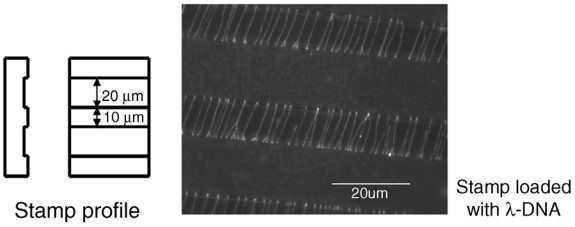

Figure 1.51 Transfer of λ-DNA, combed at a patterned PDMS surface, onto a glass substrate (Benke, 2007).

Stationary Hydrodynamic Flow The stretching, alignment, and deposition of DNA molecules by means of the drag force in liquid flow, as it has been done simply with a moving droplet of aqueous solution, can be done in a better controllable way by means of a more complex experimental setup (Figure 1.53). An open flow cell is arranged on an inverted microscope. A patterned array of interdigital gold electrodes on a glass slide is chosen as a substrate in this example. It is covered with 200 µl of 100 mM phosphate buffer. A controlled flow velocity is realized as indicated in the drawing. The microcapillaries can be positioned by means of a micromanipulation system. It allows the control of the flow velocity, the flow direction with respect to the electrode array, and the depth profile of the velocity field. For the monitoring of the stretching process, the molecules are labeled with the fluorescent dye YOYO-1. Intercalation of the dye increases the contour length of the labeled DNA. With a staining ratio of 0.72 base pairs per dye molecule, the length of λ-DNA increases from 16.2 to 21.8 µm. In order to facilitate covalent binding of the sticky ends of the double-stranded λ-DNA to the gold electrodes, both ends are thiolated (T–DNA–T)

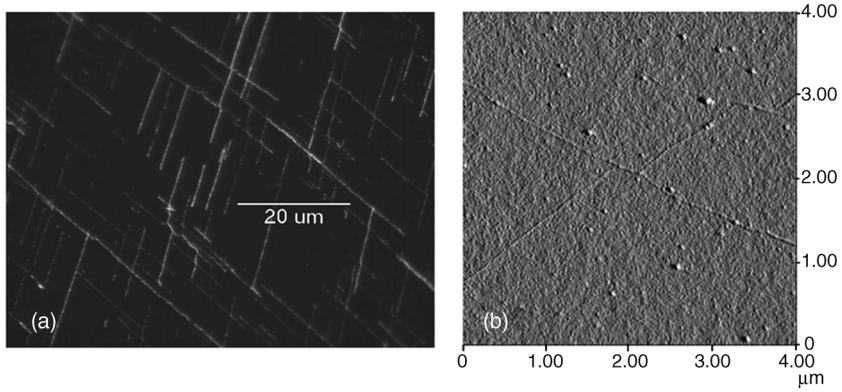

Figure 1.52 Fluorescence image (a) and AFM image (b) of a DNA network of λ-DNA aligned by molecular combing technique on a PDMS stamp and transferred onto a glass surface. The pattern of crossing DNA was produced by two-step stamping. (Reproduced with permission from Benke *et al.* (2011). Copyright 2011, IOP Publishing Ltd.)

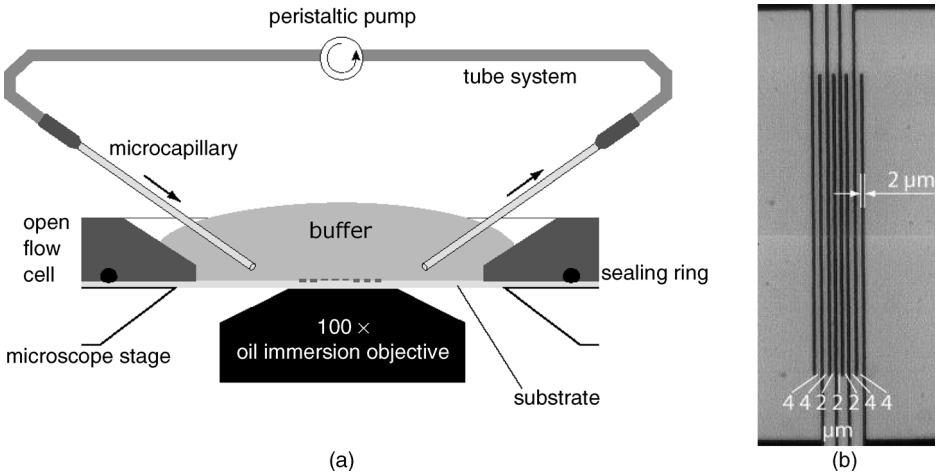

Figure 1.53 Setup for hydrodynamic deposition of DNA. (a) Open flow cell arranged on an inverted fluorescent microscope, with microcapillaries positioned above the substrate. (b) Substrate with an interdigital electrode array. (Reprinted with permission from Erler, Guenther, and Mertig (2009) and Erler (2010). Copyright 2009, Elsevier.)

by the Klenow polymerization reaction as described above. The stretching of a coiled DNA molecule tethered at one end to an electrode is controlled by the flow velocity.

In a model experiment with single DNA, Wirtz (1995) has studied the transport behavior of single DNA in liquids. The fluorescently labeled DNA tethered to a small magnetic bead was pulled by a magnetic force through a solution of unlabeled DNA molecules. Three types of conformations have been observed, depending on the flow velocity. Below 3.5 µm/s, a quasi-equilibrated *coil* shape is stable. It changes into a *trumpet* shape for $3.5\,\mu m < v < 20\,\mu m$. For higher velocities $v > 20\,\mu m/s$, a *stem and flower* conformation is observed. As mentioned above, this velocity is nearly three orders smaller than the characteristic velocity of the moving droplet in the molecular combing experiment.

Figure 1.54 shows characteristic patterns of stretched DNA, with the flow direction perpendicular to the electrodes (dark stripes). By varying the concentration of T–DNA–T in the solution, the number of interconnects can be controlled. First, the solutions were flushed in with a flow rate of about 2.5 µl/s to allow single-end binding to the gold electrodes. With a flow rate of 12.5 µl/s, the molecules became stretched, thus being able to form a bridge to the next electrode and get bound there with their free end. By clockwise changing the orientation of the flow direction with respect to the electrodes, the orientation of the interconnects can be changed (Figure 1.55a). The stability and elasticity of the immobilized molecules can be demonstrated by applying an oblique flow of buffer with 210 µl/s (Figure 1.55b). Most of the molecules are bowed out, and a smaller number of molecules are ruptured. Rupture is indicated by the short length of the fragments attached on the left at the electrodes. Probably, this rupture is caused mainly by photoinduced cleavage of the stretched DNA. Failure of the anchorage on the right would leave longer trailing ends.

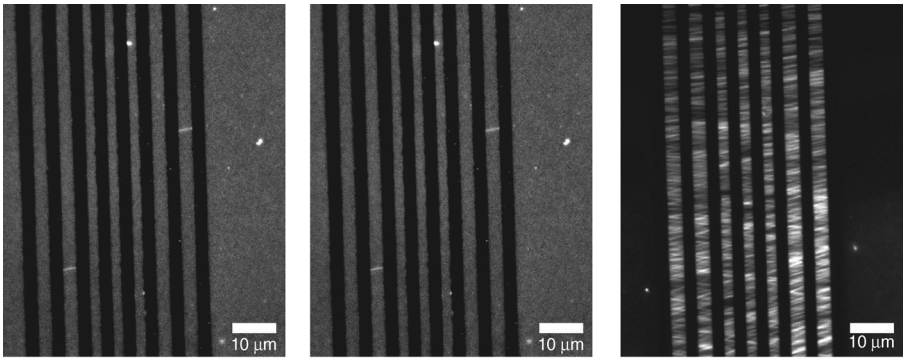

Figure 1.54 T–DNA–T bridging the gaps between electrodes after stretching in liquid flow, depending on DNA concentration of the solution: (a) 0.5 ng/μl; (b) 4 ng/μl; and (c) 10 ng/μl. (Reprinted with permission from Erler, Guenther, and Mertig (2009) and Erler (2010). Copyright 2009, Elsevier.)

DNA Branching for Network Formation Two essential steps of the bottom-up approach for nanoelectronic circuitries by using DNA have already been explained in the previous two sections: site-specific immobilization and controlled alignment of DNA molecules. However, there is still a long way to go from the discussed examples involving single- or double-stranded DNA to complex electronic circuitry. As a further step on this way, the assembling of 2D and 3D network structures has to be considered. In this context, one can try to make use of the unique properties of

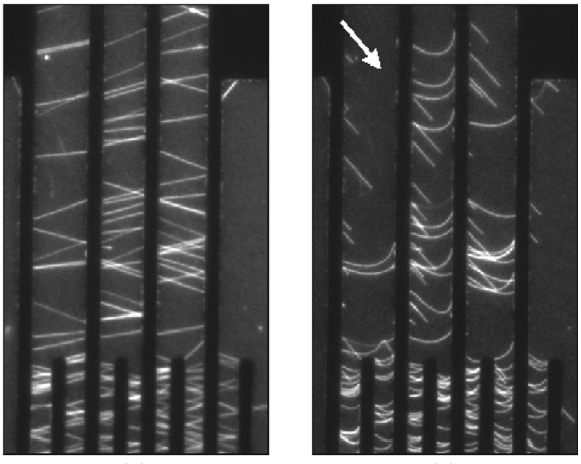

Figure 1.55 T–DNA–T bridging the gaps between gold electrodes after stretching in liquid flow: (a) as deposited; (b) affected by an oblique flow of 210 μl/s as indicated by the arrow, suitable for testing the anchoring strength. (Reprinted with permission from Erler, Guenther, and Mertig (2009) and Erler (2010). Copyright 2009, Elsevier.)

DNA, the encoding of information on the nanoscale combined with a reliable and robust recognition mechanism, and the self-assembly of DNA molecules near room temperature, for the *manufacturing of a complex DNA structure in a one-step process by self-assembly*. DNA structures obtained in this way may subsequently serve as templates for the deposition of nanoelectronic functional elements.

DNA Tiles and Origamis The fundament for the design of nanostructured DNA templates has been laid with the so-called tile model by the pioneering work of Nadrian Seeman (Seeman, 1982, 2003; Seeman and Belcher, 2002). The basic idea consists in the preparation of multi-arm junction motifs that are self-assembling tiles for higher order structures. The tiles have to be sufficiently stiff, and they must be equipped with a suitable number of single-stranded overhangs that serve as linkers for the self-assembly of the higher order structure. The tiles are formed by hybridization of single-stranded synthetic oligonucleotides (Figure 1.56a). The stiffness of the tile can be increased by a large number of crossovers between the individual molecules forming one compact tile. Up to now, a large variety of 2D and 3D tiles have been prepared. Such tiles have been successfully used to produce 2D lattices, nanoribbons (Liu *et al.*, 2005), and nanotubes (Liu *et al.*, 2004, 2006). Moreover, various 3D structures have been produced by assembling of oligonucleotides: cubes (Chen and Seeman, 1991), octahedra (Zhang

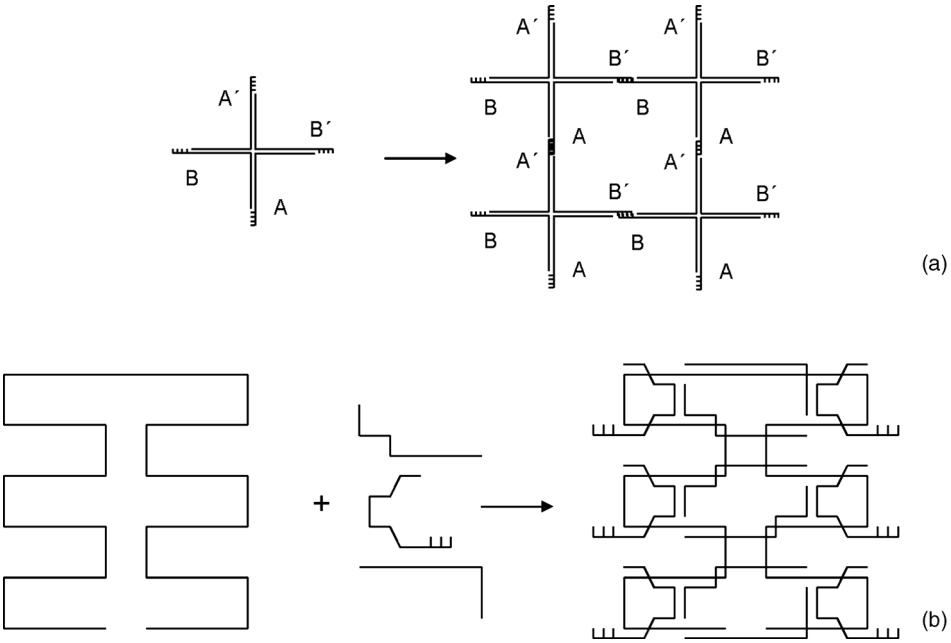

Figure 1.56 Self-assembly of large DNA structures. (a) The tile concept (Seeman, 1982): branched DNA junctions interact via sticky-end hybridization (A–A′, B–B′) to self-assemble into 2D or 3D lattices. (b) The concept of DNA origami (Shih *et al.*, 2004; Rothemund, 2006): a single-stranded DNA is folded into the intended shape and stabilized by a multitude of short staple strands. Some of the staple strands simultaneously form sticky ends.

and Seeman, 1994), buckyballs (He *et al.*, 2008), and dynamic capsules that can be switched between different states (Aldaye and Sleiman, 2007).

For the design of templates of nanoelectronic circuitries, the Seeman tiles have to be modified. The size of synthetic oligonucleotides is restricted to about 100 bases. This means that the length of single branches is only in the range of a few nanometers. For nanoelectronic networks, this size should be larger by at least a factor of 10. Therefore, the tiles should be enlarged with appropriate elongations of the short arms. This can be achieved by the following strategy (Figure 1.57) (Mertig and Pompe, 2004). In a two-step process, first a small DNA tripod is prepared with three oligonucleotides that have partially complementary sequences. Lines with same gray shades represent complementary DNA duplex strands.

Alternatively to Seeman's tile concept, Shih *et al.* (2004) and Rothemund (2006) have transferred the famous Japanese art of folding complex origamis from one

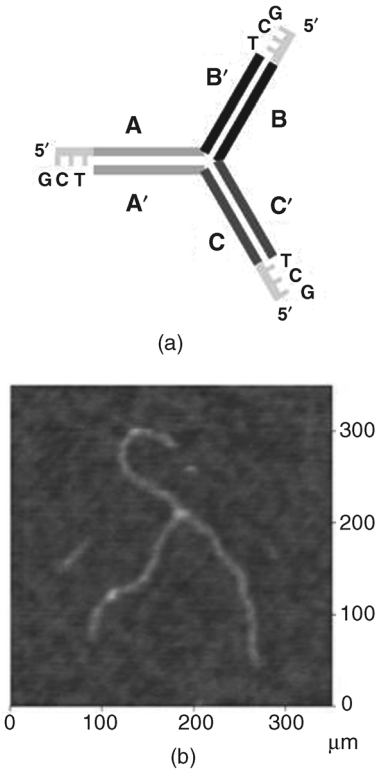

Figure 1.57 (a) Schematic viewgraph of a DNA tripod used as central element for a DNA junction. Each duplex arm possesses at its end a GCT 5′ overhang that can be used for ligation of double-stranded DNA fragments of about 500 bp and sticky ends that are complementary to the tripod overhangs. In this way, each arm of the tripod is elongated by about 180 nm long upon ligation. (b) Scanning force microscopy of a three-armed DNA junction. (Reproduced with permission from Mertig and Pompe (2004). Copyright 2004, Wiley-VCH Verlag GmbH.)

piece of paper into the DNA world. To build a complex DNA structure, only one long single-stranded DNA is sufficient if a number of short single strands (staples) are added (Figure 1.56b). Each staple strand has a unique sequence that governs a specific folding action. It allows the additional incorporation of appendices as, for example, loops. Thus, together with the folding, spatially addressable elements can be implemented in the structure. A wide range of structural variation can be obtained in this way. Examples such as a square nut, a 12-tooth gear, and a hollow box that can be opened by an external DNA "key" suggest promising applications in nanotechnology. DNA boxes that can be opened, loaded, and selectively immobilized on cells can be used as nanorobots for targeted transport of molecular payloads in order to stimulate cells in tissue cultures. Douglas, Bachelet, and Church (2012) provided the first example by creating a hexagonal DNA barrel with dimensions of 35 nm × 35 nm × 45 nm (see Figure 1.58). The barrel is formed by two domains that are covalently connected in the rear by single-stranded hinges. The barrel can be

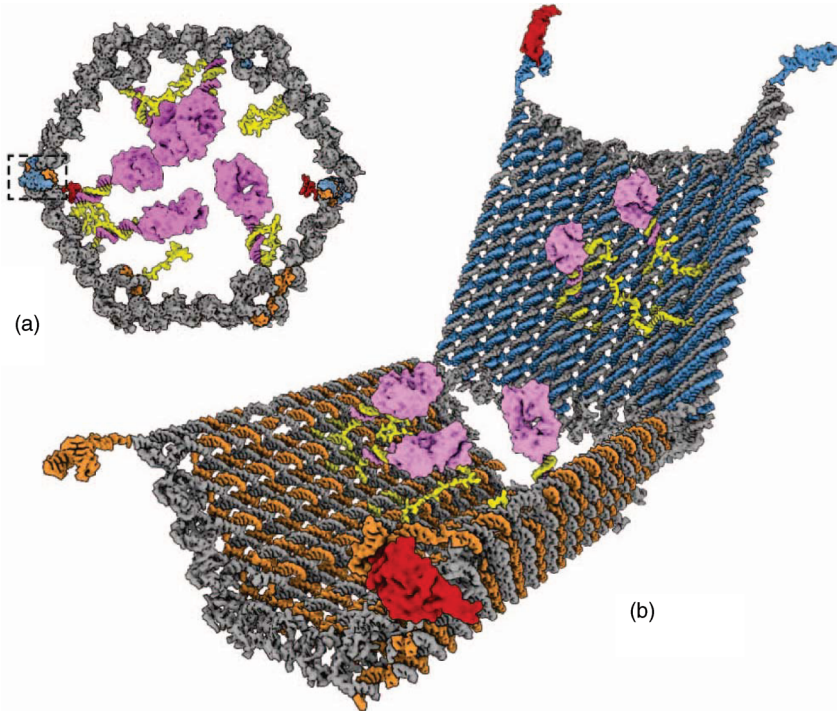

Figure 1.58 Design and TEM analysis of an aptamer-gated DNA nanorobot. (a) Schematic front orthographic view of a closed nanorobot loaded with a protein payload. Two DNA aptamer locks fasten the front of the device on the left (boxed) and the right. (b) Perspective view of the nanorobot opened by protein displacement of the aptamer locks. The two domains are constrained in the rear by scaffold hinges. (c) TEM images of robots in closed and open conformations. Left column: unloaded; middle column: robots loaded with 5 nm gold nanoparticles; right column: robots loaded with antibody fragments. Scale bar: 20 nm. (Reprinted with permission from Douglas, Bachelet, and Church (2012) Copyright 2012, AAAS.)

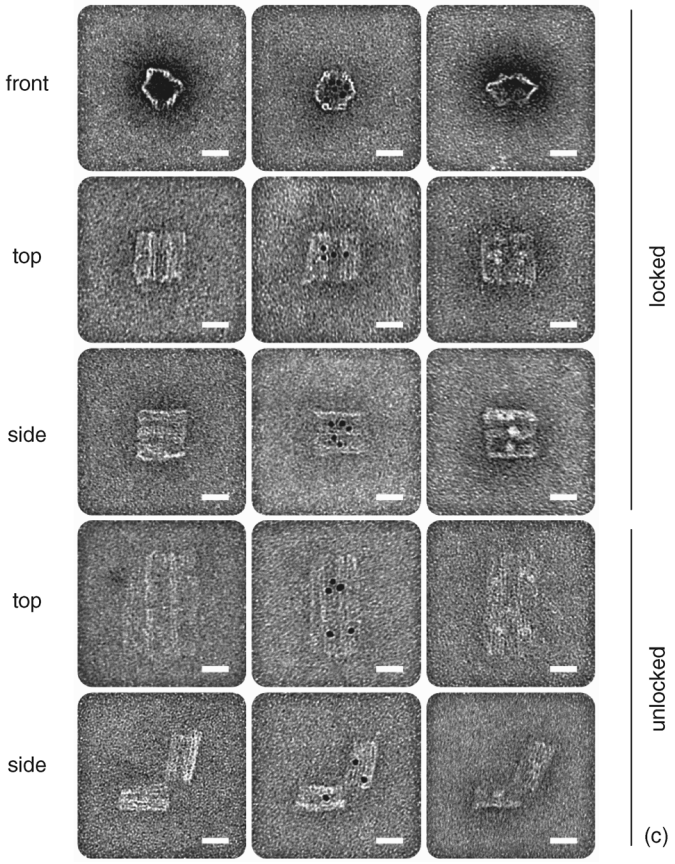

Figure 1.58 (*Continued*)

noncovalently closed in front by staples modified with DNA aptamer-based locks (for aptamers, see also Section 2.1). The locks open in response to binding antigen keys. Each barrel possesses one specific duplex of aptamer locks that undergoes opening when both aptamers recognize their corresponding antigens at the target (cell surface). Then the barrel is opened like an entropic spring. The inner faces of the barrel are exposed, and any payload previously immobilized at the inner barrel faces can interact with surface receptors. In the example, by choosing three different aptamers, six different lock duplexes were prepared. As proof of principle, the nanorobots were loaded with combinations of antibody fragments that stimulated specific signaling pathways in six different cell types leading to inhibition or activation of cellular processes, respectively.

Among the shown examples, assemblies of nanotubes or bundles are of particular interest because of their higher stiffness compared to double-stranded DNA (see also Section 7.3.1). This is useful for the design of well-aligned connections in nanoelectronic circuitries.

Electronic Properties of DNA For several reasons, DNA molecules seem to be suitable elements for the assembly of nanoelectronic circuitries, among them: (i) synthesis of tailored variants with predesigned length and base order; (ii) controlled self-assembly into well-defined shapes. Since the early 1990s, experimental work addressing the electric conductivity of single- and double-stranded DNA has been performed. The early results were contradictory as the reported *conductivities varied between metal-like and insulating*. Soon it became obvious that the results were affected by temperature, pH, humidity, and presence of counterions and oxygen, and hence did not represent the intrinsic conductivity of the DNA. The latter can be properly measured by integrating an individual DNA molecule into a microscopic solid-state device, such as a molecular field-effect transistor on a silicon chip, or a tunneling barrier between the tip of a scanning tunneling microscope and a gold film.

A favored platform for measuring electrical transport in single DNA molecules is based on nanoscopic contact structures made by single-walled carbon nanotubes (SWCNTs) integrated in a microelectronic structure on a silicon chip (Guo *et al.*, 2008; Roy *et al.*, 2008). Carbon nanotubes and DNA have similar diameters of 1–2 nm. In order to reduce the contact resistance, a strong electronic coupling between the carbon nanotubes and the DNA has to be realized. The DNA can be covalently bound to the carbon nanotubes functionalized with carboxyl groups forming the source and the drain contact. The conducting silicon wafer serves as a back gate. *I–V* curves have been measured under ambient and vacuum (10^{-5} Torr) conditions for single-stranded and double-stranded DNA (Figure 1.59). The resistance of a very short piece (~6 nm) of double-stranded DNA with well-matched base pairs has been found to be 0.1–5 MΩ (Guo *et al.*, 2008). This is in the same range as the *c*-axis resistance of highly oriented bulk pyrographite with similar dimensions (about 1 MΩ). This means that the electrical behavior of a stack of DNA base pairs is similar to that of the stack of aromatic graphite planes. The resistance increases with the width of the gap between the source and the drain. Unlike usual conducting materials, where the resistance scales with the length of the conductor, the resistance of DNA increases exponentially with length. For a ~27 nm long double-stranded DNA (80 bp long DNA fragment encoding a portion of the H5N1 gene of the avian influenza A virus), a resistance of 25–40 GΩ was measured under ambient conditions (Roy *et al.*, 2008). At a source–drain voltage of about 1 V in a

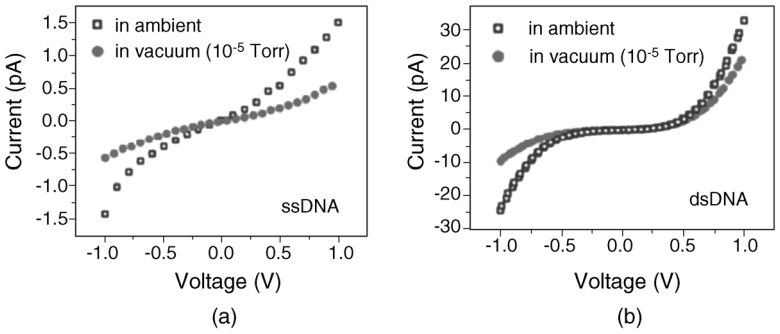

Figure 1.59 *I–V* characteristics of single DNA: (a) single-stranded DNA; (b) double-stranded DNA. (Reprinted with permission from Roy *et al.* (2008). Copyright 2008, the American Chemical Society.)

single-stranded DNA of a length ~27 nm, the current is typically only a few pA, whereas in a double-stranded DNA it is about 20 times larger. This is primarily due to the lack of a regular stacking of the nucleotide bases in the single-stranded DNA.

In most experiments, double-stranded λ-DNA has been used. Better information on the electron transport through DNA molecules can be derived from experiments with artificial poly(dA)–poly(dT) and poly(dG)–poly(dC) DNA molecules consisting of identical base pairs. Yoo *et al.* (2001) performed experiments with poly(dA)–poly(dT) and poly(dG)–poly(dC) DNA molecules with average lengths of about 0.5–1.5 μm and about 1.7–2.9 μm, respectively. More than 20 samples were analyzed at ambient conditions and in vacuum and revealed an essential difference between the two molecular species. Current–voltage curves have been measured (Figure 1.60). The

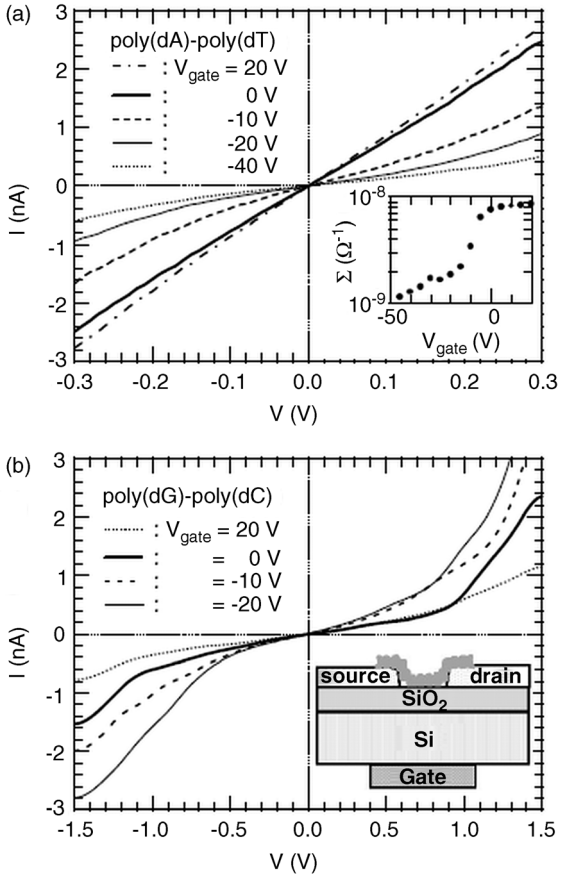

Figure 1.60 *I–V* curves measured at room temperature for various values of the gate voltage (V_{gate}) for poly(dA)–poly(dT) (a) and poly(dG)–poly(dC) (b). In the inset of (a), the conductance at $V = 0$ is plotted as a function of V_{gate} for poly (dA)–poly(dT). The inset of (b) is a schematic diagram of electrode arrangement for gate-dependent transport experiments. (Reprinted with permission from Yoo *et al.* (2001). Copyright 2001, the American Physical Society.)

electron transport between the source and drain electrodes was additionally influenced by an external electric field caused by the constant potential V_{gate} of a gate electrode placed next to the current path (see Figure 1.60b). The evaluation of the conductance Σ (slope of the I–V curve) at $V = 0$ reveals a significant difference in the dependence on the gate voltage for the two types of molecules. The inset of Figure 1.60a shows that the conductance decreases when a negative voltage V_{gate} is applied. It means that the charges transported in the poly(dA)–poly(dT) molecules are electrons hindered in their motion by the negative gate potential. Consequently, the molecule behaves like a *n-type semiconductor*. However, in poly(dG)–poly(dC) molecules the conductance Σ increases when the gate voltage gets negative, as can be seen in Figure 1.60b. The charges, transported between source and drain, are positively charged holes. The molecule is like a *p-type semiconductor*. A strong temperature dependence of the conductance has been observed around room temperature with a crossover to a weak temperature-dependent conductance at low temperatures. This dependence can be explained by a stepwise thermal excitation of the vicinity of the charge carriers moving forward as so-called hopping polarons.

Metallization of DNA One of the conclusions of the previous subsection is that the electronic properties of DNA are not suitable for assembling nanoelectronic circuitry with DNA molecules only. However, their outstanding biochemical properties related to versatile structural transformations such as scission, ligation, and hybridization facilitate various "cut and paste" procedures that may be useful in following a bottom-up approach toward complex structures. In the 1990s the question arose whether it would be possible to modify the DNA chemically in order to improve the electron transport. Generally, the various functional units of the DNA offer options to add further organic or inorganic compounds without loosing its unique ability of self-assembly and information coding. For improving the electronic properties by metallization, the following three concepts have been explored: (i) incorporation of metallic ions into the base pair stack, (ii) DNA-directed assembly of metallic or semiconducting nanoparticles using DNA templates and hybridization of complementary sequences, and (iii) heterogeneous nucleation and growth of metal clusters at the DNA (Figure 1.61).

Incorporation of Metallic Ions into the Base Pair Stack Already in 1993, a new conformation of DNA, the so-called M-DNA, has been reported (Lee *et al.*, 1993). At pH values above 8, B-DNA undergoes a conformational change in the presence of divalent metal ions Zn^{2+}, Co^{2+}, or Ni^{2+}. NMR studies show that the imino protons with coordination to the N3 position of thymine and the N1 position of guanine are replaced by the divalent ions. This means that the natural hydrogen bonds are replaced by *metal coordination interaction*. The absorption and circular dichroism spectra of the M-DNA differ only slightly from those of B-DNA. In every base pair (T–A or C–G), one divalent metal ion is incorporated while one hydrogen bond is retained. The metal ion is "interchelated". The distance between the metal ions is about 0.4 nm regardless of the sequence of the double-stranded M-DNA. Thus, the normal B-DNA can be reformed without denaturation on removal of the metal ion.

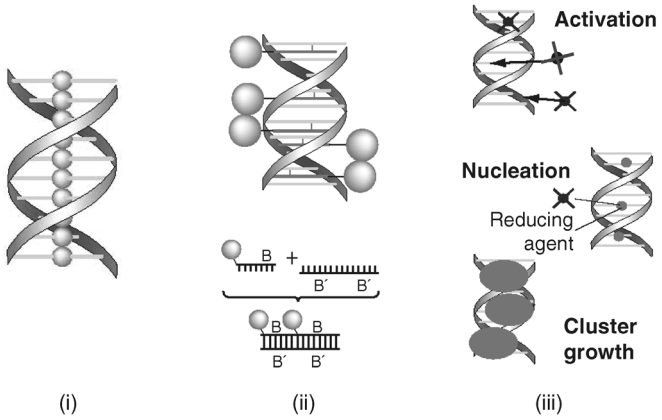

Figure 1.61 Possible concepts for improving the electronic properties of DNA: (i) incorporation of metallic ions into the base pair stack; (ii) DNA-directed assembling of metallic or semiconducting nanoparticles, using DNA templates and hybridization of complementary sequences; and (iii) heterogeneous nucleation and growth of metal clusters.

The regular quasiperiodic distribution of the metal ions in the center of the base-paired M-DNA helix implies enhanced electron transport. Resistance measurements in vacuum at room temperature show metal-like conductivity of M-DNA, unlike B-DNA, which behaves as a narrow-bandgap semiconductor (Rakitin *et al.*, 2001). Conductivity measurements were performed on DNA bundles of $\sim 10^2$ molecules. The *I–V* curves of the B-DNA show a pronounced asymmetry. As a possible explanation, electric fields could build up within the B-DNA bundles, related to double-well potentials associated with the imino protons in the center of the helix with coordination to the N3 of thymine and N1 of guanine in every base pair. In M-DNA, these imino protons are replaced by Zn^{2+} ions leading to a collapse of the double-well potentials (Figure 1.62). The M-DNA behaves as a molecular wire with a diameter of one atom surrounded with a negatively charged insulator. In addition, the wire exhibits all the structural advantages of a natural B-DNA, such as molecular coding of information and the capability of self-assembly.

The substitution of synthetic bases for natural base pairs offers a second route for the incorporation of metal complexes into oligonucleotides of DNA. Tanaka *et al.* (2006) have developed synthetic nucleosides that form chelator complexes with metal ions such as Pd^{2+}, Pt^{2+}, Cu^{2+}, and Hg^{2+} (Figure 1.63). Two *nucleobases are paired through interstrand metal coordination*. This principle allows a large variety of structures to be generated by incorporation of metal ions into DNA at any position by automated DNA synthesis. Similarly, linear metal arrays can be built by template-directed formation onto preorganized duplexes with appropriate metal binding mismatches. Oligonucleotides have been synthesized that bear salicylic aldehyde mismatches (S–S) as the metal complexing unit and thymine mismatches. The S–S base pair can only complex a metal ion (M = Cu^{2+}, Ni^{2+}, Mn^{3+}, Fe^{3+}, and VO^{2+}) in the presence of an equimolar amount of ethylenediamine (en) (S–M(en)–S). The thymine mismatch (T–T) is used for the Hg^{2+} complexation instead of the pyridine

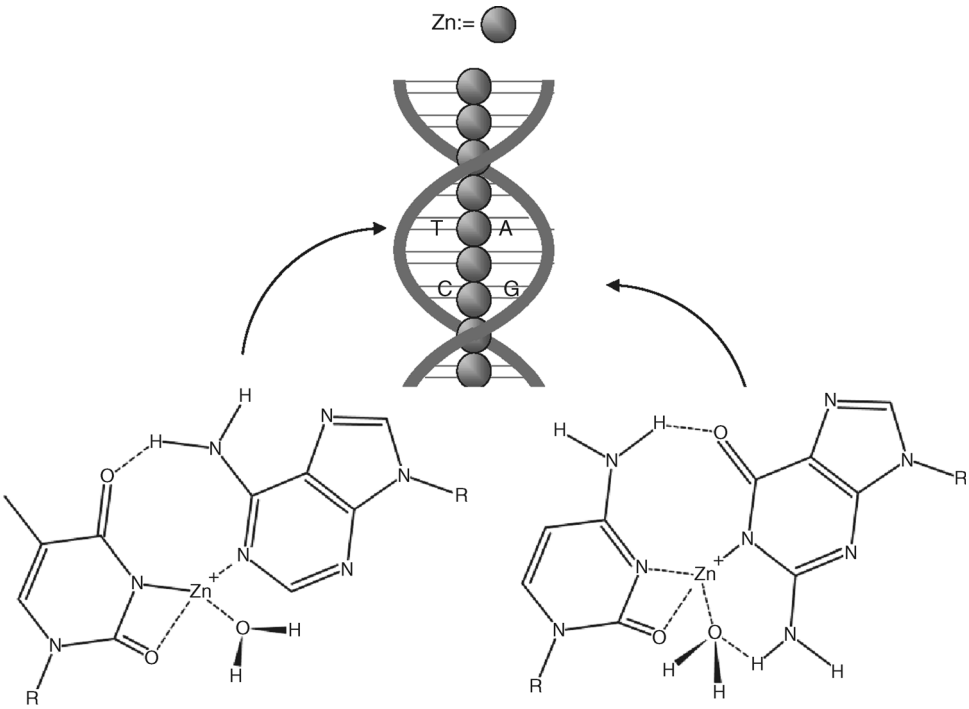

Figure 1.62 Base-pairing scheme for M-DNA with Zn^{2+} (Aich *et al.*, 1999). The imino protons with coordination to the N3 position of thymine and the N1 position of guanine are replaced by the divalent Zn^{2+} ion.

bases (P–P) that are also possible (as shown in the first example). Already Kuklenyik and Marzilli (1996) had demonstrated that two thymine bases in a single-stranded DNA can be cross-linked by a Hg^{2+} ion forming a T–Hg–T pair that can cause conformational changes such as a hairpin–duplex transition. The feasibility of the template concept has been demonstrated by preparing a double-stranded 20-mer with a central cassette of 10 metal complexing units (5 S–S and 5 T–T mismatches) creating a robust bimetallic ion stack inside the DNA double helix (Tanaka *et al.*, 2006). A certain restriction of the Tanaka concept is set by the limited length of synthetic oligonucleotides. The examples show that the development of M-DNA and oligonucleotides with synthetic bases points to a new technology of future molecular electronics in which DNA with *programmable conductivity and magnetism* could be used as nanoelectronic building blocks.

The formation of specific bonds between metal ions and nucleotide bases has found another promising application in nanotechnology for the *development of analytic tools*. Metal ions such as Hg^{2+} and Ag^{+} are severe environmental pollutants. Therefore, there is a high demand for a cheap and reliable analytic device for analysis of water and food with respect to such contaminations. The change of the fluorescence of semiconductor quantum dots (QDs) such as CdSe, ZnS, or corresponding alloyed

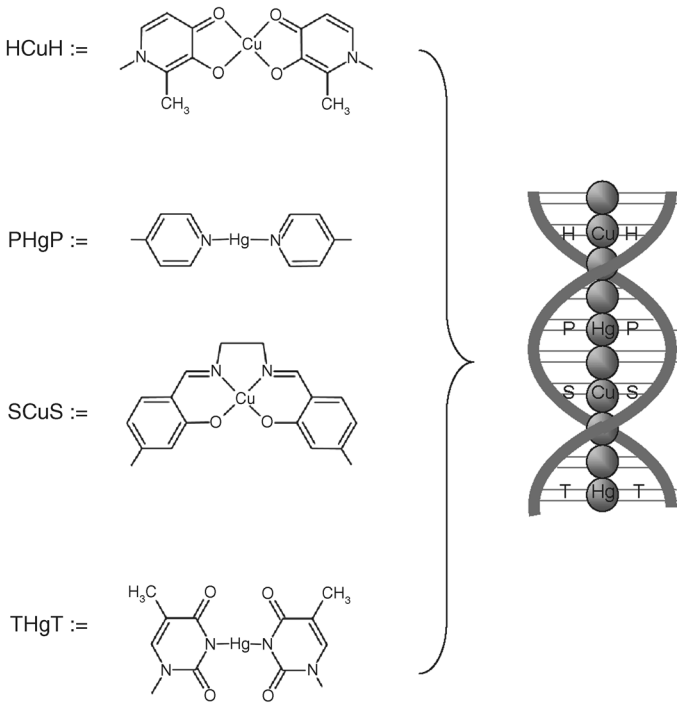

Figure 1.63 Heterogeneous metal assembly through Cu^{2+}- and Hg^{2+}-mediated duplex formation between two artificial oligonucleotides in which two hydroxypyridone nucleobases (H) and one pyridine nucleobase (P) replace the natural base pairs, and assembly through use of salicylic aldehyde–salicylic aldehyde (S–S) as well as thymine–thymine (T–T) mismatches for heterogeneous metal stacking consisting of S–Cu^{2+}(en)–S and T–Hg^{2+}–T base pairs (Tanaka *et al.*, 2006).

materials in the presence of metal ions has served as the basic idea for the development of such a sensor system. The fluorescence intensity of the QDs is reduced by electronic energy transfer to metal ions, if there are any nearby. This process, the so-called electron-transfer quenching, can be realized by functionalizing the QDs with oligomers that contain appropriate sequences of thymine and cytosine (see also Figure 1.64). Hg^{2+} ions bridge thymine bases. Similarly, Ag^{+} ions form stable cytosine bridges. By an appropriate arrangement of these bases along the oligomers **1** and **2**, a rigid hairpin structure is formed in the presence of Hg^{2+} and/or Ag^{+} ions, respectively. If QDs of differential sizes, which fluoresce at differential wavelengths, are functionalized with T- or C-modified oligomers, a multiplexed analysis can be realized.

The same principle can be applied to the design of logic gate operations (Freeman *et al.*, 2009). Figures 1.65 and 1.66 show how the two basic states "0" and "1" can be realized by making use of the specific electron-transfer quenching of two QDs of different sizes by Hg^{2+} or Ag^{+} ions as input. Quenching of both wavelengths (in the presence of both ions) may represent the signal "1", whereas quenching of only one

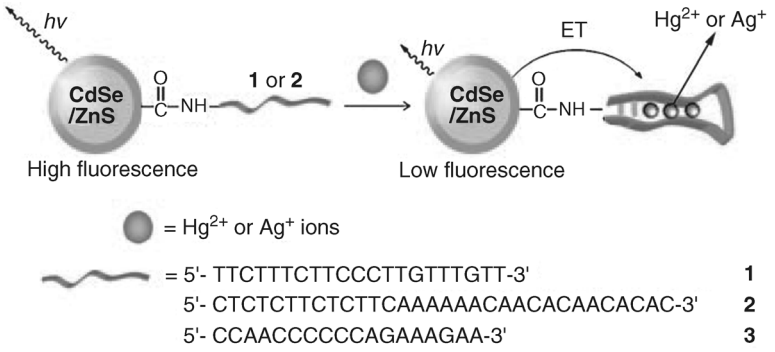

Figure 1.64 Optical analysis of Hg^{2+} and Ag^{+} ions by nucleic acid modified QDs. Examples for possible oligonucleotide sequences are (**1**) 5′-TTCTTTCTTCCCTTGTTTGTT-3′ and (**2**) 5′-CTCTCTTCTCTTCAAAAAACAACACAACACAC-3′. (Reproduced with permission from Freeman *et al.* (2009). Copyright 2009, Wiley-VCH Verlag GmbH.)

wavelength (in the presence of only one of the ion species) may represent the signal "0". The proposed system can be considered as a first step for the implementation of QDs as optical readout signals for logic gate operations.

DNA-Directed Assembly of Metallic or Semiconducting Nanoparticles Using DNA Templates and Hybridization of Complementary Sequences Prefabricated nanoparticles can be assembled along a DNA by covalent or electrostatic interaction. An

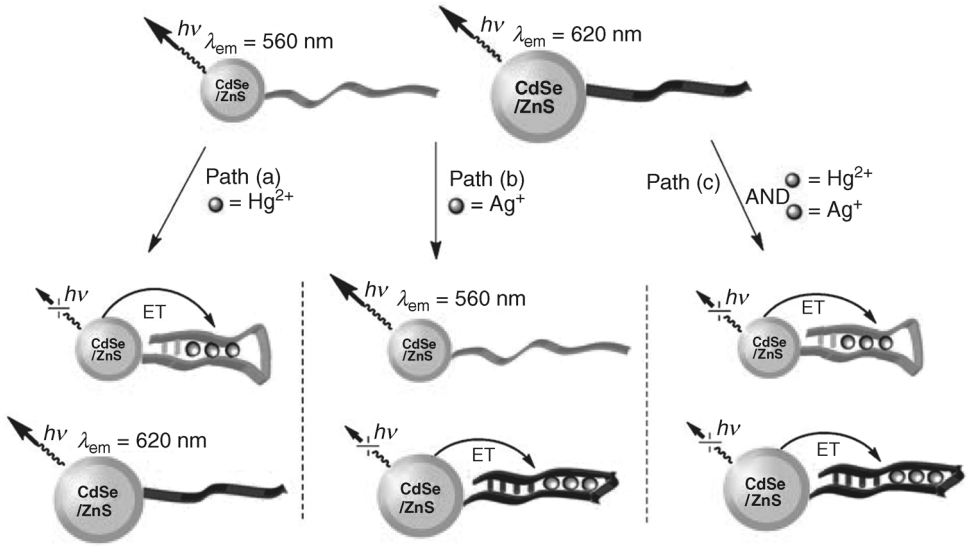

Figure 1.65 The "AND" logic gate system based on the electron-transfer (ET) quenching of **1**- and **2**-QDs by Hg^{2+} and Ag^{+} inputs. (Reproduced with permission from Freeman *et al.* (2009). Copyright 2009, Wiley-VCH Verlag GmbH.)

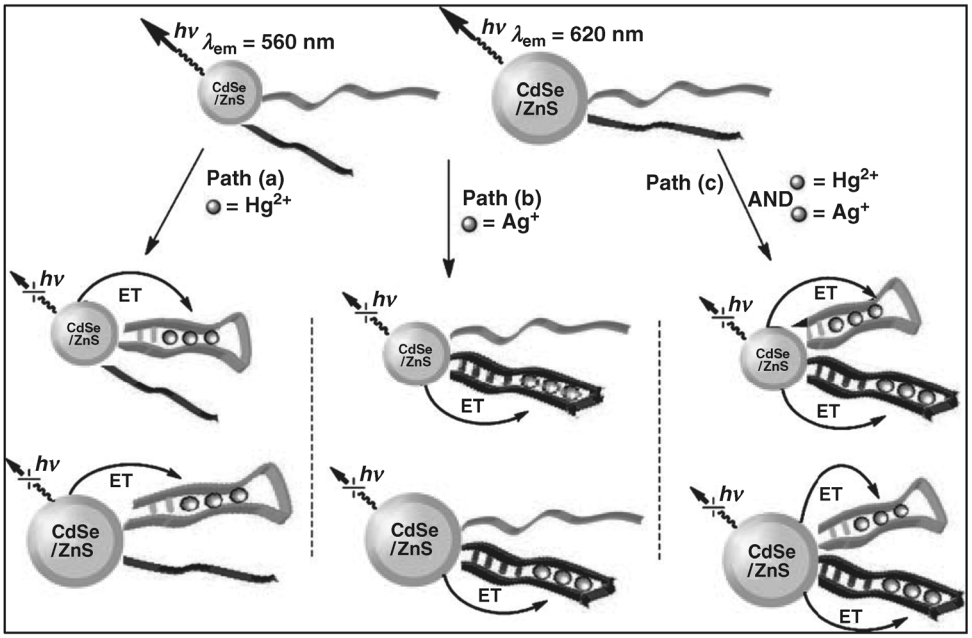

Figure 1.66 The "OR" logic gate system based on the electron-transfer quenching of **1**- and **2**-QD by Hg^{2+} and Ag^{+} inputs. (Reproduced with permission from Freeman *et al.* (2009). Copyright 2009, Wiley-VCH Verlag GmbH.)

example for covalent integration has been elaborated by the Willner group in 2002 (Patolsky *et al.*, 2002). Site-specific covalent binding of 1.4 nm Au nanoparticles with thymine bases in a double-stranded poly(A)–poly(T) duplex has been realized in a three-step process. In the first step, the Au particles functionalized with mono-*N*-hydroxysuccinimide are covalently linked with amino psoralen (Figure 1.67), which acts as intercalator in the second step when the modified Au particles are mixed with a solution of poly(A)–poly(T) duplexes of about 900 nm length. After 20 min, the mixture is irradiated with UV light ($\lambda < 360$ nm) for 45 min, which causes a photo-induced covalent attachment of the intercalator at the thymine residues. AFM images prove that a well-organized Au nanoparticle wire is formed in the poly(A)–poly(T) template (Figure 1.68). The average height of 4 nm can be interpreted as the intercalation of single nanoparticles in the helical double-stranded DNA.

Harnack *et al.* (2002) have used Au nanoparticles (1.3 nm) capped with negatively charged tris(hydroxymethyl)phosphine (THP) for the metallization of calf thymus DNA. First, the DNA molecules were spin coated on a silicon substrate in order to stretch the molecules. The solution of THP–Au colloids was then applied to the substrate for 2–15 min, rinsed, and dried. Surprisingly, it was possible to create a dense deposition of the negatively charged particles along the negatively charged DNA. Obviously, the electrostatic interaction was screened by the presence of additional molecules in the solvent (ethanol–water mixture). It is assumed that short-range

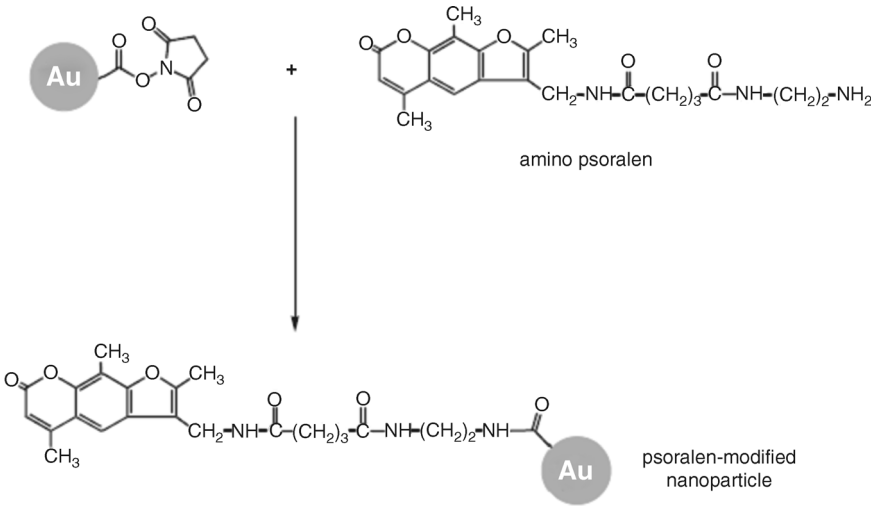

Figure 1.67 Functionalization of Au nanoparticles with amino psoralen, which facilitates intercalation with poly(T)–poly(A) duplexes. (Reproduced with permission from Patolsky *et al.* (2002). Copyright 2002, Wiley-VCH Verlag GmbH.)

interactions such as hydrogen bonds between THP and DNA facilitate the binding. There can also be covalent bonds between THP and amino groups of the DNA bases. In the final process step, the tiny Au nanoparticles were enlarged by electroless gold plating, which provided a nanowire with a diameter of about 30–40 nm. The wires showed ohmic behavior with resistivity of $\sim 3 \times 10^{-5}\ \Omega$ m, which is about 1000 times higher than the bulk resistivity of gold ($2 \times 10^{-8}\ \Omega$ m). A similar strategy has been applied by Sastry *et al.* (2001) exploiting the electrostatic interaction of positively charged Au nanoparticles (4 nm in size) with the negative charges of the phosphate backbones of double-stranded DNA. The gold clusters were capped with lysine

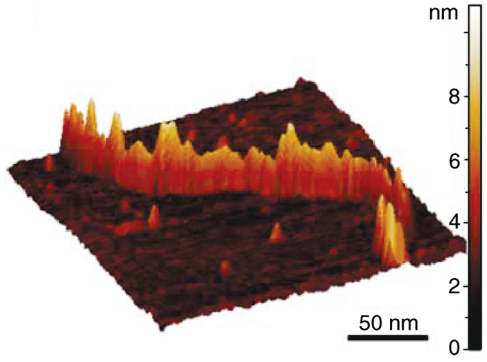

Figure 1.68 AFM image of a chain of Au nanoparticles intercalated in a poly(A)–poly(T) template. (Reproduced with permission from Patolsky *et al.* (2002). Copyright 2002, Wiley-VCH Verlag GmbH.)

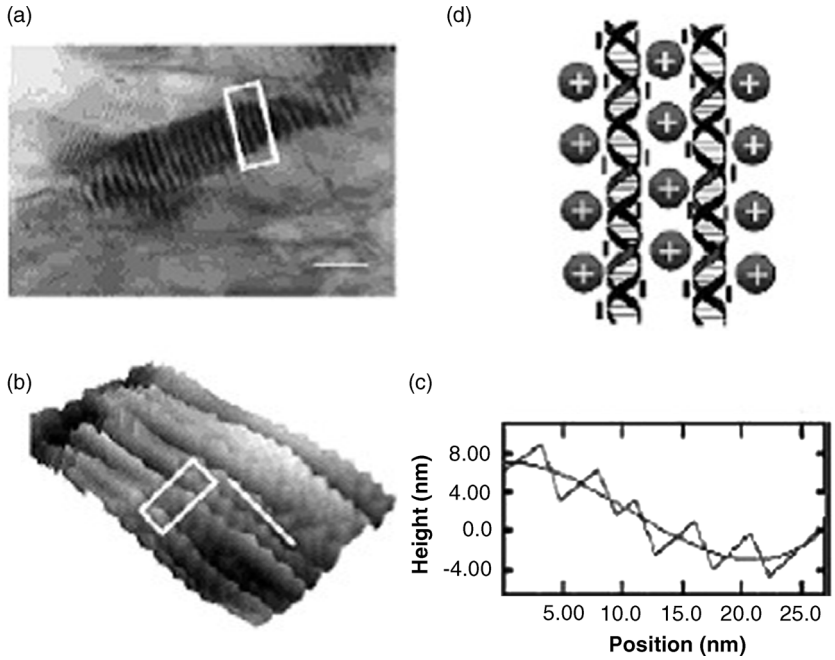

Figure 1.69 Formation of Au superclusters on a band-like template of oligonucleotides. (a) TEM picture of a Au supercluster mediated by a template of 15-mer oligonucleotides. (b) Scanning tunneling microscopy (STM) image of a Au supercluster grown on a template of 30-mer oligonucleotides. (c) Height change profile along the line in the STM image. (d) Proposed structure model for the band-like Au supercluster. (Reproduced with permission from Kumar *et al.* (2001). Copyright 2001, Wiley-VCH Verlag GmbH.)

molecules causing a positive surface charge at pH 7. Fifteen- and 30-mer oligonucleotides were hybridized with complementary oligomers. Films of the short double-stranded DNA templates were cast on a Si wafer or quartz substrate. After drying the film, the Au particle solution was dropped onto the film. As shown in the TEM pictures of Figure 1.69, bands of closely packed Au superclusters were formed where the width of the bands is in the range of the length of the DNA duplexes. The positive charges of the lysine molecules bound to the gold particles and the negative charges of the phosphate backbones of the short DNA duplexes cause the assembly to form a "line-by-line" structure in the film. This is similar to the "layer-by-layer" structure of anionic and cationic polyelectrolytes organized onto a planar substrate (see also Section 4.3). Obviously, the initial DNA structures were still sufficiently mobile to relax into the energetically favored band-like line-by-line structures.

Heterogeneous Nucleation and Growth of Metal Clusters The various functional groups of a DNA can also serve as nucleation sites for heterogeneous nucleation of metal clusters starting with aqueous solution of metal salts (Mertig *et al.*, 2002; Seidel, Mertig,

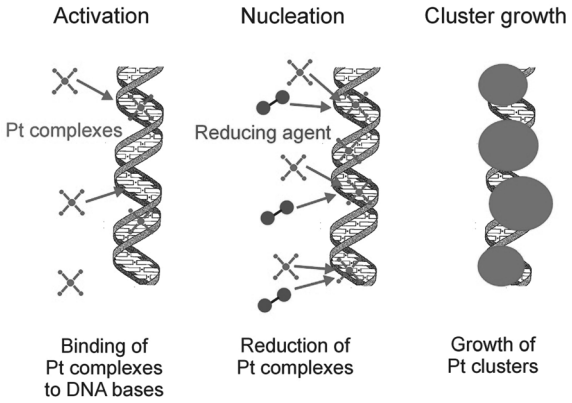

Figure 1.70 DNA metallization by heterogeneous nucleation as a two-step process: activation by site-specific binding of metal complexes; formation of seeds by adding reducing agent; and stable cluster growth from seeds. (Reproduced with permission from Mertig and Pompe (2004). Copyright 2004, Wiley-VCH Verlag GmbH.)

and Pompe, 2002; Seidel *et al.*, 2004). By stable growth of these clusters and their aggregation, continuous metallic wires can be produced on the DNA template. This idea is based on the work by Coffer, Bigham, and Li (1996) and Braun *et al.* (1998). Coffer and coworkers had deposited Cd^{2+} ions on plasmid DNA. By reducing them with H_2S, chains of 5 nm CdS clusters at the ring-shaped templates were produced. Braun *et al.* adapted this concept for metallization of λ-DNA. For this purpose, λ-DNA was stretched between electrodes and activated with silver salt solution. Afterwards, the immobilized silver complexes acted as nucleation sites for the growth of silver clusters in the presence of hydroquinone as a reducing agent. Finally, a granular conducting wire of 100 nm in diameter was obtained.

The principle of heterogeneous nucleation and growth of metal clusters on DNA is shown in Figure 1.70. The *electroless metallization of DNA* involves two steps. First, metal ions or complexes are immobilized at specific binding sites. Platinum, and palladium complexes are preferentially bound at the bases. *The DNA bases act as electron donors.* It has been shown that the N7 position of guanine bases is a preferred site for covalent binding of hydrolyzed metal complexes (Lippert, 1999; Colombi Ciacchi, 2002). Other metal ions such as cadmium and copper bind preferentially to the phosphates at the backbone. Typically, the reaction time for sufficient activation of the DNA is in the range of a few hours. For example, the activation with platinum complexes starting with K_2PtCl_4 is saturated after ∼10 h. In the following process step, a *reducing agent* is added in order to provide electrons for the further reduction of the bound metal complexes. *Suitable reducing agents* are dimethylaminoborane (DMAB, $(CH_3)_2NH{\cdot}BH_3$), hydroquinone (HQ, $C_6H_4(OH)_2$), sodium borohydride ($NaBH_4$), or hydrogen. Instead of applying a reducing agent, photoreduction is another option. For example, silver (Berti *et al.*, 2005) and platinum (Erler, Guenther, and Mertig, 2009) particles have been grown by exposing the DNA with metal complexes to 254 nm UV

irradiation. It is assumed that the DNA acts as a light harvester that favors the localized metallization. The bound metal complexes are reduced to seeds for the *stable growth of clusters* along the DNA. A typical example of a metallized λ-DNA is shown in Figure 1.71 (Mertig *et al.*, 2002). High-resolution transmission electron microscopy reveals

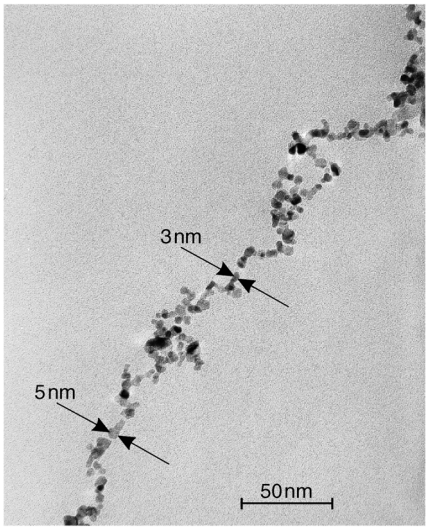

(a)

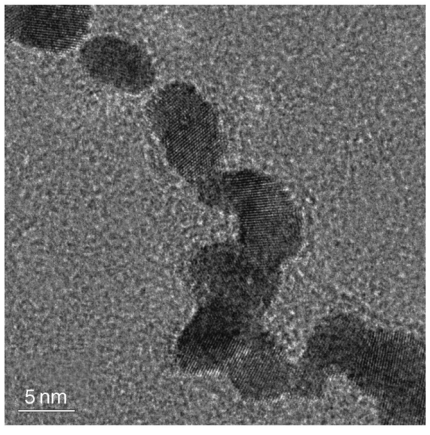

(b)

Figure 1.71 Pt cluster chain grown on λ-DNA. The DNA was incubated in a K_2PtCl_4 solution for 10 h, keeping the ratio of hydrolyzed metal complexes to nucleotides at 65 : 1. The reducing agent DMAB has been applied for the initiation of cluster growth. (a) TEM image of a continuous chain of platinum clusters (diameter: 4 ± 1 nm). (b) High-resolution TEM image of the platinum clusters grown on the DNA. The lattice planes of the single crystals can be seen. Several clusters are fused, thus forming a short conducting path along the DNA. (Reproduced with permission from Mertig and Pompe (2004). Copyright 2004, Wiley-VCH Verlag GmbH.)

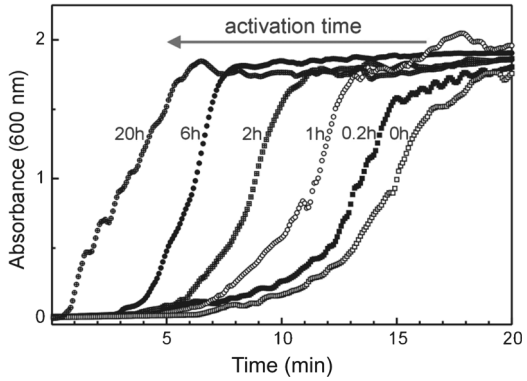

Figure 1.72 Optical absorbance versus time of a hydrolyzed K_2PtCl_4 solution at 600 nm in the presence of λ-DNA. (Reproduced with permission from Mertig and Pompe (2004). Copyright 2004, Wiley-VCH Verlag GmbH.)

that the clusters are single crystals, where the (111) lattice plane distance of $d = 0.227$ nm corresponds to that of bulk platinum. As a characteristic feature of the experiment, there is no indication of homogeneous nucleation of platinum clusters in the solution. This is unexpected because only about 3% of the available Pt complexes are bound to the DNA during the activation. The heterogeneous nucleation sites are highly effective. They act as autocatalytic reaction sites in the subsequent growth process. The influence of the activation on the rate of heterogeneous nucleation is also evident from optical absorption measurements during the metallization reaction. The change of the absorbance indicates the formation of colloidal platinum at the DNA. The reduction time needed for complete metallization of the DNA decreases with longer activation time (Figure 1.72). The role of the nucleotides in the metallization process becomes obvious from the plots of reduction time versus activation time for several ratios of G–C and A–T pairs (Figure 1.73). The reduction time is defined here as the time required to reach half saturation of the absorbance. The lower reduction time for

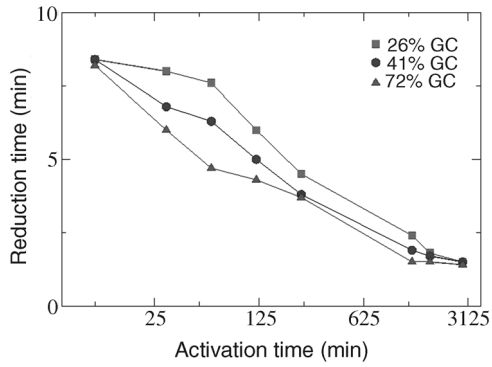

Figure 1.73 Influence of the GC content of the DNA on the metallization kinetics. (Reproduced with permission from Mertig and Pompe (2004). Copyright 2004, Wiley-VCH Verlag GmbH.)

higher G–C content indicates higher binding efficiency of the G bases compared to the A bases for platinum complexes.

The stochastic nature of the growth process and the interface stresses of touching clusters with different crystallographic orientations are the reasons for a fluctuating shape of the ultrathin cluster chains. Therefore, metallized DNA suitable as nanowire for bridging gaps of a few micrometers has to be thicker, typically $\geq$50 nm. In the temperature range from 300 down to 4.2 K, the relation between current and voltage is linear for wires of such type (Richter *et al.*, 2002), indicating metallic conductivity. Interestingly, here the conductivity of the nanowires is only a factor of about 7 lower than that of the bulk material. The conductivity of 2×10^4 S/cm corresponds to a mean free electron path of 2 nm, which is about the same size as the grown clusters (Figure 1.74). Hence, the observation is compatible with the concept of conductivity being governed by the scattering of the electrons at the grain boundaries. The presence of metallic conductivity is confirmed by the linear dependence on temperature in a wide range. The conspicuous deviation at about 30 K and below is due to the *quantum nature of the electron scattering process*. The

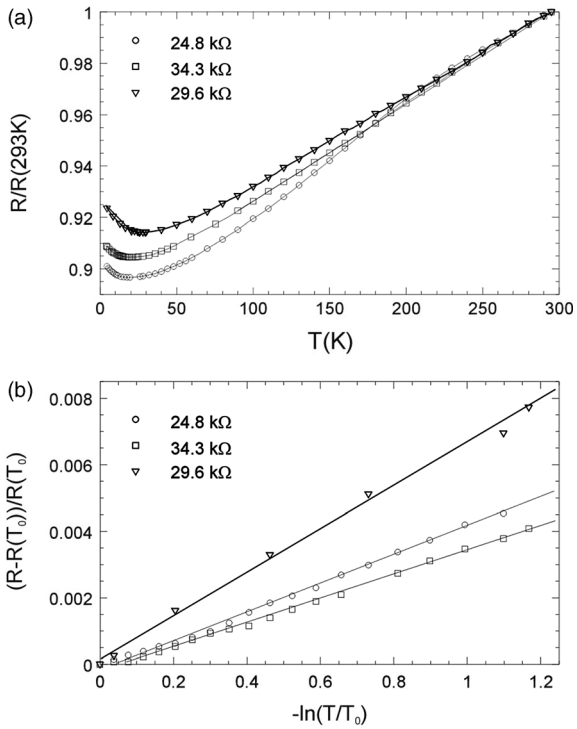

Figure 1.74 (a) Temperature dependence of the resistance of three palladium wires, normalized to their room-temperature resistances of 24.8, 29.6, and 34.3 kΩ. (b) Low-temperature resistance versus $-\ln(T/T_0)$, with $T_0 = 13.5$ K. (Reproduced with permission from Richter *et al.* (2002). Copyright 2002, Springer + Business Media.)

logarithmic dependence of the increase below 30 K indicates that the electron transport in the nanowires corresponds rather to *scattering processes in a thin film* (2D) than in a 1D structure. Annealing of the Pd nanowires for 2 h at 200 °C caused grain growth resulting in lower resistance at room temperature, higher temperature coefficient of the resistance, and disappearance of the quantum behavior at low temperature.

The advantage of DNA for heterogeneous nucleation and for growth of metallic nanowires is still more obvious when additionally the molecular recognition properties are exploited. This opens the way to *molecular lithography*. Braun and coworkers have given an impressive example for such an option by patterning a gold nanowire at molecular resolution (Keren *et al.*, 2002), as shown in Figure 1.75a. The basic idea is a sequence-specific covering of short areas along the DNA *with enzymes*. In the example, RecA was chosen, which facilitates the so-called homologous recombination, a protein-mediated reaction by which two DNA molecules with homologous sequences are linked. RecA monomers can be polymerized on a selected DNA sequence to form a *nucleoprotein filament*. Such filaments are then mixed with the target, a solution of double-stranded DNA. It leads to *site-specific covering of the target DNA due to binding at the sites of the homologous recombination*. This routine process from molecular biology can be implemented in the metallization process. In step (i), RecA monomers polymerize on a single-stranded DNA molecule to form the nucleoprotein filament. In step (ii), the nucleoprotein filament binds to an aldehyde-derivatized double-stranded target DNA at a homologous sequence. The bound aldehyde groups act as localized reducing agents in the following nucleation of metal clusters along the derivatized DNA. In step (iii), incubation in $AgNO_3$ solution results in Ag nuclei arranged along the target DNA at regions unprotected by RecA. In step (iv), the Ag nuclei serve as catalysts for electroless gold deposition, which converts the unprotected regions into conductive gold wires. In this step, hydroquinone is applied as a reducing agent. Thus, the site-specific deposition of RecA on aldehyde-derivatized DNA enables the manufacturing of patterned nanowires with well-defined isolating gaps in between. The efficiency of this process has been demonstrated by producing gold nanowires (diameter 50 nm) with an insulating gap region covered with a 2027-base RecA nucleoprotein filament. The approach described has been refined by changing the sequence of process steps by marking already the natural DNA with a RecA pattern before aldehyde derivatization is performed, as schematically shown in Figure 1.75b (Keren, Berman, and Braun, 2004). The derivatization of the DNA with glutaraldehyde occurs only at regions that are not covered with RecA protein. After removal of excess glutaraldehyde, the RecA protein can be disassembled so that underivatized regions along the DNA are left over. Subsequent metallization occurs only at the aldehyde-derivatized regions whereas the underivatized DNA segments are available for biomolecular manipulation based on the recognition properties of DNA. One interesting option is the immobilization of metallic clusters or semiconducting quantum dots at those sites (as schematically shown in Figure 1.75b), or biotinylated DNA strands to create junctions and networks in nanoelectronic devices.

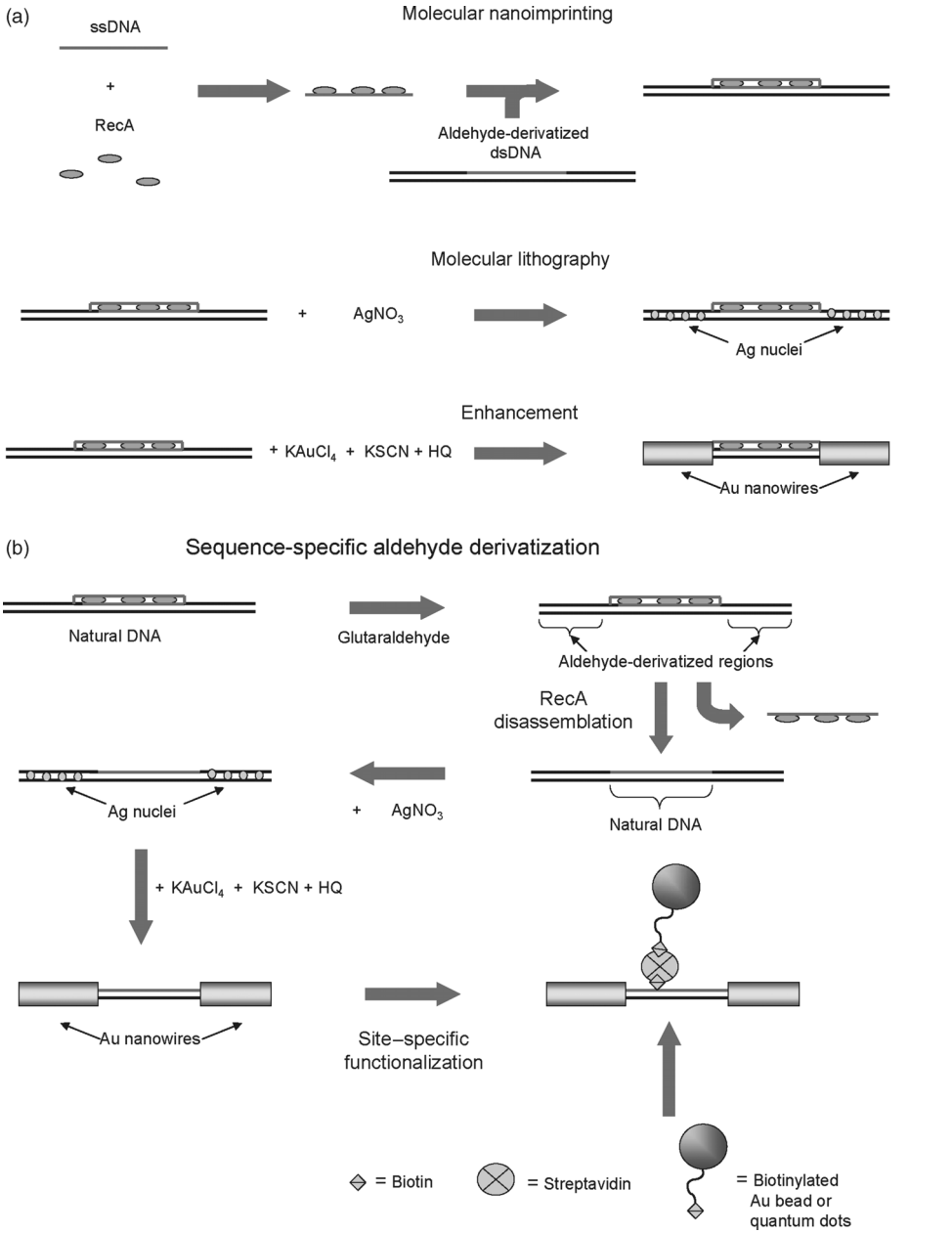

Figure 1.75 Schematics of the homologous recombination reaction and molecular lithography. (a) The site-specific recombination of the structured ssDNA with the aldehyde-derivatized dsDNA leads to a patterned template for the following metallization of the unprotected regions of the DNA template. HQ = hydroquinone. (b) Localization of a reducing agent, glutaraldehyde, on selected DNA sequences directs their metallization. DNA retains its recognition capability and other biological functionalities at the nonderivatized region. (Adapted from Keren, Berman, and Braun (2004).)

1.3.2.2 DNA-Based Nanoprobes

The unique properties of metallic and semiconducting nanoparticles (NPs), related to fluorescence, magnetism, and electronic behavior, make them interesting for a broad range of applications including materials technology, biotechnology, and medicine. Mostly applied are NPs of gold, magnetic alloys, ZnS, CdS, CdSe/ZnS, silica, diamond, and nanorods (NRs), such as carbon nanotubes. Typical sizes of the NPs range from 2 to 50 nm. Advanced preparation technologies guarantee well-defined particle sizes and shapes. Variation of sizes and shapes as well as alloying offers additional degrees of freedom for tuning the physical properties, as shown by the examples depicted in Figures 1.76 and 1.77 for the optical properties (extinction and plasmon resonance) of

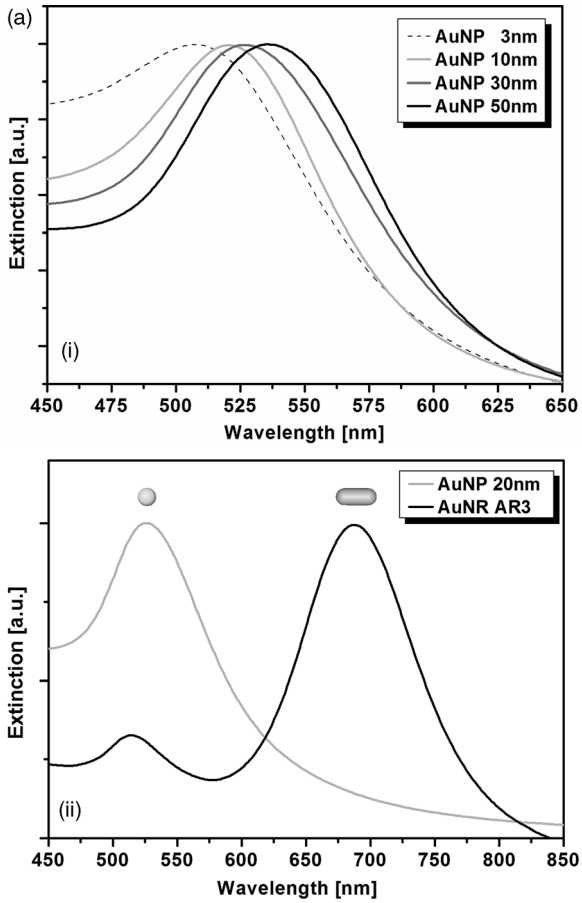

Figure 1.76 (a) UV–Vis spectra of spherical gold nanoparticles and gold nanorods. The peak positions of the plasmon resonance due to collective oscillation of the valence electrons depend on the particle diameter (i), and the aspect ratio (AR) (here AR = 3 with diameter of 20 nm) (ii). (b) Variation of size and shape of Au nanoparticles depending on growth conditions: (i) Au nanospheres; (ii) spherical Au cores with a magnetite shell; (iii, iv) Au nanorods; and (v, vi) prismatic Au nanoparticles. (Reprinted with permission from Lakatos (2013).)

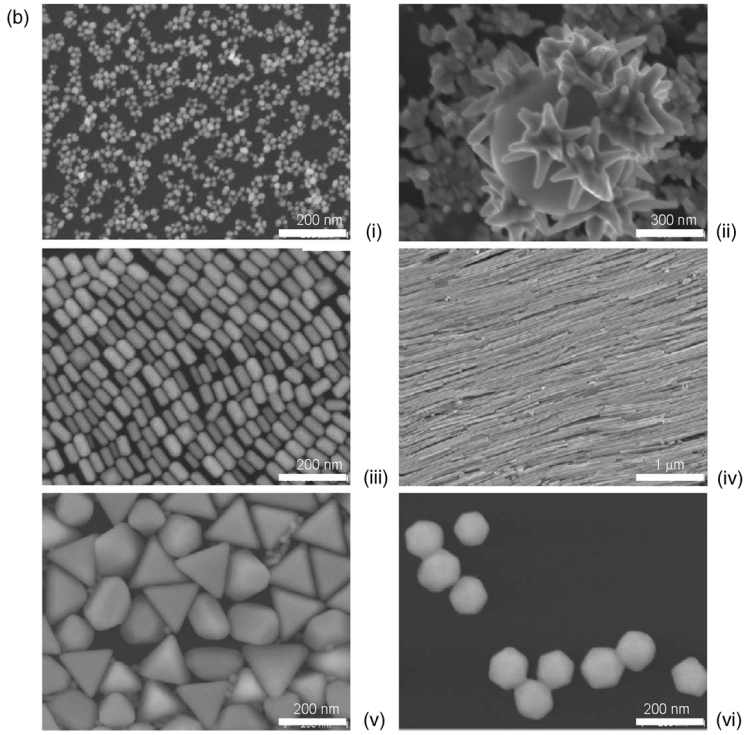

Figure 1.76 (*Continued*)

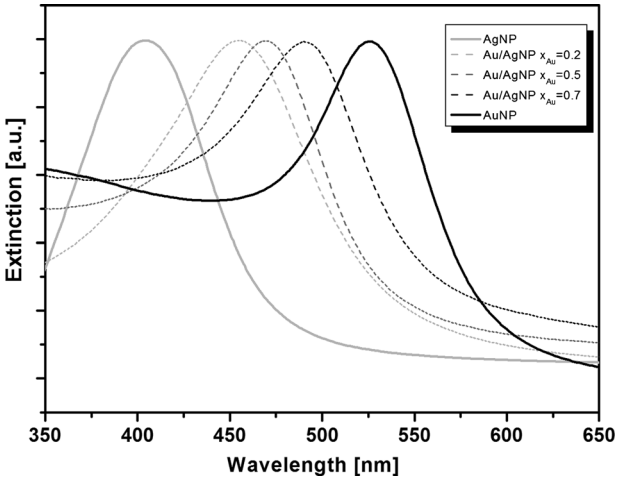

Figure 1.77 Change of the UV–Vis spectra of alloyed Au/Ag nanoparticles. With increasing Au concentration (x_{Au}), the plasmon resonance shifts from yellow to red. (Reprinted with permission from Lakatos (2013).)

gold nanoparticles (AuNPs), gold nanorods (AuNRs), and alloyed Au/AgNPs. Hence, the physical and chemical properties of nanomaterials are tunable. As another extension of versatility, nanomaterials can be functionalized with biomolecules. In this way, molecular recognition patterns can be utilized for biologically directed self-assembly of biofunctionalized nanoparticles into higher order structures. These topics will be discussed in detail in Chapter 7. Respective developments were initiated with DNA-conjugated nanoparticles. Therefore, they are considered here as an introduction into the broader field.

It is not surprising that the breakthrough in the application of DNA-conjugated nanoparticles was realized in biodiagnostics. Nanoprobes capable of reading biomolecular signals and translating them into physical or chemical signals are highly desirable in this field (Rosi and Mirkin, 2005). Diagnostic assays for DNA, proteins, small molecules, or metal ions in life sciences as well as in environmental technology are examples for this development. Research activities are aiming at inexpensive and disposable systems that allow rapid and user-friendly data acquisition. At the same time, the novel systems should exhibit a sensitivity meeting or even exceeding the current standard. In the area of DNA diagnostics, the standard is represented by the polymerase chain reaction (PCR) in combination with molecular fluorophore technology. In PCR, the theoretically achievable sensitivity is nearly unlimited. However, complexity, cost, and restrictions in multiplexing (detection of multiple targets in one assay) set serious bounds in praxis with a sensitivity of about 100 aM. For protein diagnostics, the new techniques have to compete with the sensitivity realized with enzyme-linked immunosorbent assays (ELISA) (~pM limit).

In 1996, the Alivisatos group and the Mirkin group published independently two basic papers on "nanocrystal molecules" combining the recognition properties of DNA with the physical properties of nanobeads (Alivisatos *et al.*, 1996; Mirkin *et al.*, 1996). These structures have been produced by attaching single-stranded DNA oligonucleotides of defined lengths and sequences to individual AuNPs. The thiol-terminated oligonucleotides have been covalently linked to the gold particles. These AuNPs can be assembled into complex structures by adding additional single-stranded DNAs that are partially complementary to every one of the immobilized oligonucleotides (Figure 1.78a). Densely packed lattices of gold clusters are produced by self-assembly. In the case of short oligonucleotides and short target DNA, the small distance between the gold beads leads to mutual electronic interaction. This interaction affects the plasmon resonance spectrum of the particle in the form of a red shift of the plasmon peak. The change of light absorption turns the color of the colloidal gold solution from red to blue. Furthermore, the interaction between the gold beads affects the melting transition of the DNA. The melting transition of the DNA in assemblies with metallic nanoparticles is significantly sharper than that of unmodified DNA. Apparently, the melting of DNA in such aggregates is a highly cooperative process (see also Section 1.2.4), and the presence of the gold nanoparticles obviously enhances the cooperativity (Jin *et al.*, 2003). The transition profile is affected by various factors, such as the DNA surface density, the nanoparticle size, the interparticle distance, and salt concentration in the solvent. An increasing oligonucleotide density on the nanoparticle surface leads to an increase of the

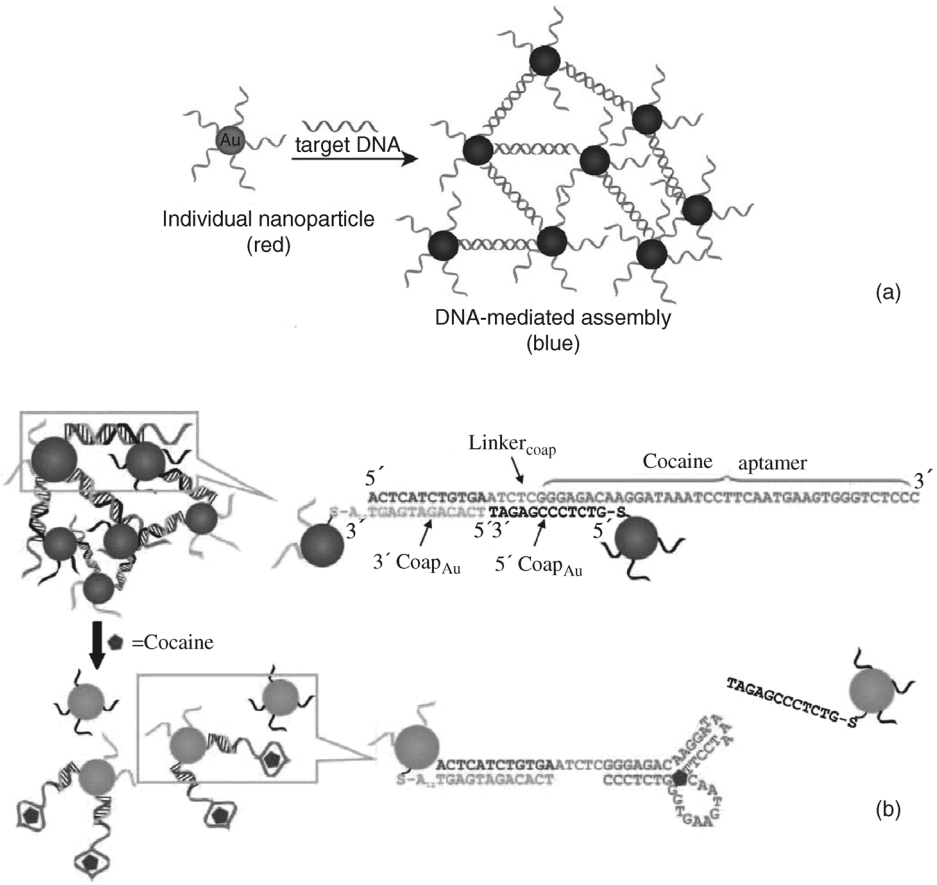

Figure 1.78 Au nanoparticle-based colorimetric sensors. (a) In the presence of complementary target DNA, oligonucleotide-functionalized AuNPs aggregate, turning the color of the solution from red to blue. (Reproduced with permission from De, Ghosh, and Rotello (2008). Copyright 2008, Wiley-VCH Verlag GmbH.) (b) Aptamer-based colorimetric detection of cocaine by disassembling of the nanoparticles. (Reproduced with permission from Liu and Lu (2006). Copyright 2006, Wiley-VCH Verlag GmbH.)

melting temperature and a sharper profile. Larger particle size is connected with a higher number of links. Increasing the salt concentration causes an enhanced charge screening of the negatively charged DNA, and hence an increase of the melting temperature. Below a critical concentration, melting at room temperature is observed. Increasing the interparticle distance by adding poly(A)$_n$ spacer segments at each end of the DNA duplex increase the melting temperature as the electrostatic repulsion of the nanoparticles is diminished with the larger distance.

In another approach, aptamers, which are single-stranded oligonucleic acid-based binding molecules with the ability to bind a wide range of targets with high affinity and specificity, have been incorporated into such colorimetric sensor. An example has been

worked out for cocaine sensing, using a cocaine-specific aptamer by Liu and Lu (2006). For this purpose, the Au nanoparticles were functionalized with two different sequences of single-stranded DNA, one for conjugation and another one with the cocaine aptamer as shown in Figure 1.78b. The sensor assay was made of two kinds of Au nanoparticles, one kind functionalized with a 3′-thiol-modified DNA ($3'Coap_{Au}$) and another one functionalized with a 5′-thiol-modified DNA ($5'Coap_{Au}$). To create aggregates, linker DNA ($Linker_{Coap}$) molecules have been used. The linker was composed of three segments. The first segment hybridized with a $3'Coap_{Au}$ nanoparticle. The second segment hybridized with the last five nucleotides of a $5'Coap_{Au}$ nanoparticle. The third segment was the aptamer sequence for cocaine. By adding the $Linker_{Coap}$ to a solution of the two kinds of Au particles, purple-colored aggregates were formed. In the presence of cocaine, the aptamer changed its structure to bind cocaine. As a result, only five base pairs were left to hybridize with $5'Coap_{Au}$. This link was unstable at room temperature. The $5'Coap_{Au}$ particles dissociated from the $3'Coap_{Au}$ particles. The disassembly of the aggregates caused a color change of the solution from purple to red.

The sharp melting transition is one of the most important advantages for use of metallic nanoparticles as colorimetric sensors in chip-based systems. It is the basic concept of the so-called *scanometric assay* (Taton *et al.*, 2000). Different capture strand DNAs are immobilized on a glass chip. The target DNA of interest is recognized by a particular capture strand. A sequence of the captured target DNA is then labeled with a specific oligonucleotide–nanoparticle conjugate. Nonspecifically bound targets are washed away. In the final step, the bound gold particles can be enlarged by catalytic reduction of silver onto the surface. The bound structures are evaluated by light scattering. The scattered light is much more intense than the fluorescent light. For example, the intensity scattered by one 80 nm gold particle is comparable to that emitted from 10^6 fluorescein molecules. As another advantage, the signal is resistant to quenching. As target concentrations as low as 50 fM can be detected with this approach, this technique possesses a sufficiently high sensitivity to possibly replace the costly PCR in medical praxis.

The catalytic silver enlargement of immobilized AuNPs can also be applied for the *electrical detection* of the target molecule (Park *et al.*, 2002). In such a setup, oligonucleotide capture strands are immobilized in the gap between two electrodes (Figure 1.79). Analogous to the previous example, target DNAs together with appropriately functionalized AuNPs form sandwich complexes that can be enlarged by the catalytic silver deposition. The target DNA is detected by the change of the electrical resistance between the two electrodes. For a nonoptimized version, a detection limit of 500 fM has been reported. There is another outstanding feature of the experiment. It allows a stringent differentiation between perfectly complementary DNA sequences and those with a single mismatch. As discussed above, the sandwich structures are characterized by a sharp melting transition. Therefore, when the chip is washed at 50 °C before treatment with silver enhancer solution, the complexes with a single-base mismatch are denatured, whereas the complexes with perfectly complementary sequences remain stable. After the subsequent silver enhancement for 3–20 min, the resistance of gaps spotted with perfectly complementary strands is typically 500 Ω, whereas the gaps with single-base mismatches

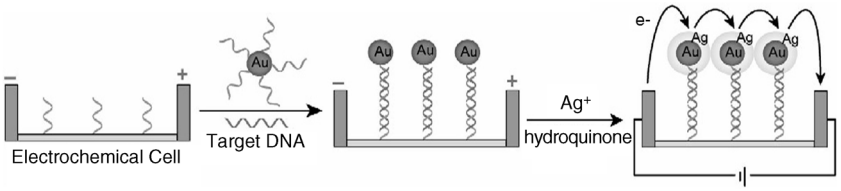

Figure 1.79 Electrical detection of DNA. Capture oligonucleotides whose one end is fixed to a patterned area in the gap between two electrodes bind to a complementary part of the target DNA in the solution. Oligonucleotides whose one end is fixed to an AuNP bind to another complementary part of the target DNA so that the AuNP becomes tethered to the substrate. Catalytic deposition of silver onto the sandwiched structure leads to a composite structure that can be detected electrically by the change of the electrical resistance. (Reproduced with permission from De, Ghosh, and Rotello (2008). Copyright 2008, Wiley-VCH Verlag GmbH.)

behave as insulators, with resistances exceeding 200 MΩ. Differentiation of perfectly and nonperfectly hybridized complexes can also be realized by exploiting the influence of salt solutions on the stability of hybridized structures. Washing the chip with solutions with suitable concentrations of cations (e.g., Na^+) at room temperature before silver amplification is another possibility to denature the single-base-mismatch complexes. The electrical detection approach can be realized in conventional microelectrode arrays. Thus, it is well suited for massive multiplexing, when a larger array of electrode pairs is spotted with different capture oligonucleotides.

The sensitivity of the assay can be increased about 100-fold by exploiting the interaction of metal particles and electromagnetic waves. Under laser irradiation, strong electric fields arise near the particles. Depending on the particle size and shape, the local power density can exceed that of the laser beam by 10^6–10^8. This phenomenon is utilized for surface- or particle-enhanced Raman spectroscopy (SERS). It is one of the most sensitive spectroscopic techniques in chemistry. Multiplexed spectrometric detection has been realized with conjugates of gold nanoparticles and *Raman dye-labeled oligonucleotides* (Cao *et al.*, 2002) (Figure 1.80). Compared to conventional fluorescence assays with multiple fluorophores as labels, Raman spectroscopy is favorable for several reasons: narrow spectroscopic lines, broader spectral window, and single-wavelength laser sufficient for excitation. By the additional silver enhancement, a sensitivity of ~20 fM was reached in a nonoptimized experiment.

The signal amplification with silver-coated AuNPs leads to a maximum sensitivity of ~100 aM in scanometric detection of target DNA, provided that a preceding target amplification by PCR is applied. However, PCR is a time-consuming process, which is a disadvantage for practical use. There is another alternative approach with less expensive and faster indirect target amplification, called the *bio-barcode amplification* (BCA) (Nam *et al.*, 2002, 2004). The basic idea of the BCA approach is summarized in Figure 1.81. Two different types of biofunctionalized probes are applied in the procedure. The first one is a magnetic iron oxide microparticle (MMP) deposited with single-stranded capture oligonucleotides that are complementary to one half of the sequence of the target oligonucleotide (analyte). The second probe is an AuNP (about 30 nm size) functionalized with two different types of oligonucleotides. One

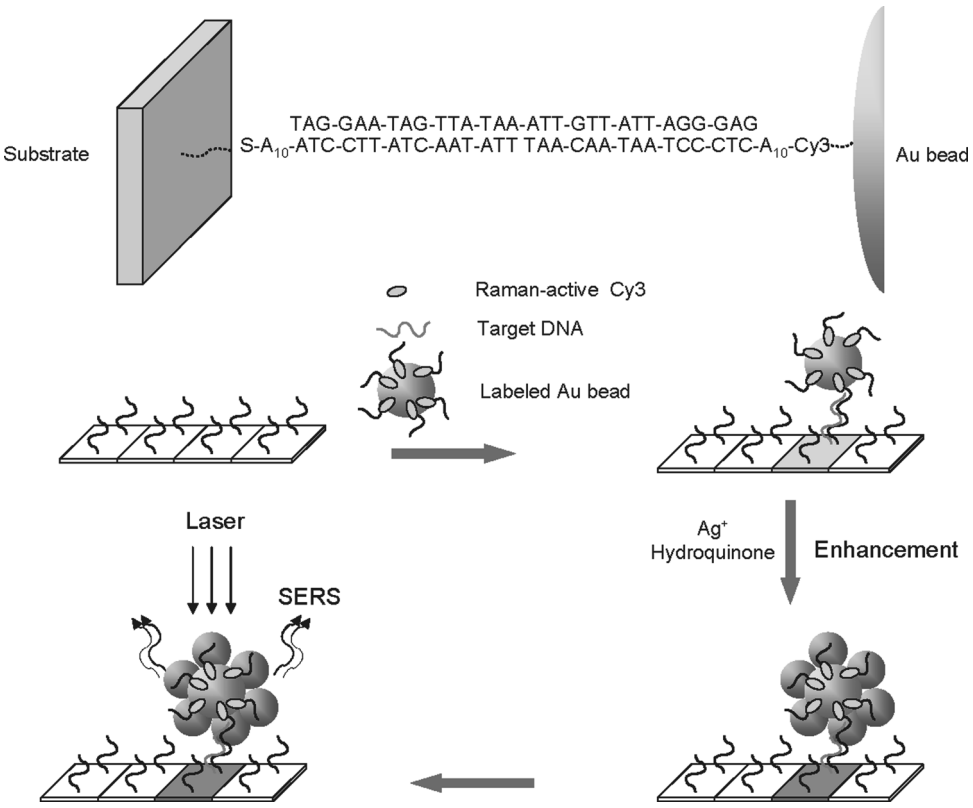

Figure 1.80 Scheme for SERS detection of DNA targets. In a sandwich assay similar to those above, DNA nanoparticles encoded with Raman-active dyes (e.g., Cy3) are hybridized to the surface-immobilized capture/target hybrid and silver enhancement is performed. Upon single-wavelength laser excitation, the particles emit a strong and reproducible Raman spectrum specific to the Raman-active dye chosen. (Reproduced with permission from Thaxton and Mirkin (2004). Copyright 2004, Wiley-VCH Verlag GmbH.)

is complementary to the second half of the target sequence (analyte), and the other one is complementary to the half of a barcode sequence (amplification signal). This second oligonucleotide acts as a unique identification tag of the particular target sequence. In order to realize high amplification, the ratio of barcode binding DNA and target binding DNA has to be large (about 70 : 1), and the total number of bound oligonucleotides per AuNP should be about 300–400. The whole detection process consists of three steps. In step 1, sandwiched structures of MMPs, AuNPs, and target DNA are formed by hybridization in a mixture of the functionalized MMPs and AuNPs together with the target DNA. After hybridization, in step 2, the magnetic sandwiched structures together with unreacted MMPs are separated from the solution by a magnetic field. By repeated washing, the unreacted DNA and AuNPs are removed. Afterward, the magnetic field is switched off. In pure aqueous solution, the particles are heated to 55 °C for 3 min to release the barcode

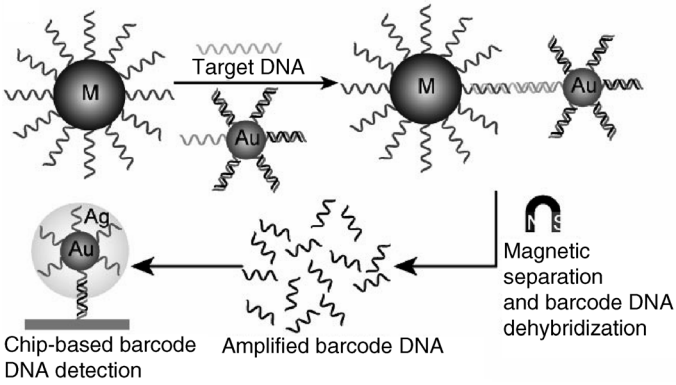

Figure 1.81 Schematics of the DNA BCA assay. The two types of biofunctionalized particles used in the BCA: (Au) AuNPs functionalized with two different oligonucleotides. One is complementary to half of the sequence of the target DNA, whereas the second one is complementary to half of a specific barcode sequence. (M) Magnetic iron oxide microparticles functionalized with one type of oligonucleotides that are complementary to the second half of the sequence of the target DNA. After magnetic separation, chip-based DNA detection can be applied for identification of the amplified barcode DNA. (Reproduced with permission from De, Ghosh, and Rotello (2008). Copyright 2008, Wiley-VCH Verlag GmbH.)

DNA by dehybridization. Also in step 2, the MMPs are removed from the solution by reapplying the magnetic field. In step 3, the solution with barcode DNA can be analyzed with the above-mentioned scanometric method. The high ratio of barcode binding DNA to target binding DNA deposited onto the AuNPs leads to very high amplification of the initial signal. Nam *et al.* (2004) have shown that 500 zM ($zM = 10^{-21}$ M) concentration of target DNA ($\sim$10 copies in a 30 µl sample) can be differentiated from a control solution with only noncomplementary DNA.

DNA-Directed Assembly of Single-Walled Carbon Nanotubes Single-walled carbon nanotubes are one of the most promising artificial nanomaterials for application in electronics, optics, plasmonics, mechanics, thermal transport, biosensing, and drug delivery. The outstanding physical properties, such as electrical and thermal conductivities, mechanical strength, and stiffness, make them a preferred material for the manufacturing of nanocomposites. Several difficulties have to be overcome on the way from preparation to application: separation of bundles of the hydrophobic carbon tubes in aqueous solution, assembling of the SWCNTs into large architectures, and the formation of binding sites for a subsequent functionalization with other nanostructures. This can be done by linking SWCNTs with single-stranded DNA, based on the observation that single-stranded DNA molecules wrap around the hydrophobic SWCNTs. This mechanism has been exploited for dispersion of SWCNTs in aqueous solutions, and sorting them with respect to metallic and semiconducting tubes (Zheng *et al.*, 2003). By the conjugation of SWCNTs with single-stranded DNA, their binding sites can be used for a subsequent self-assembly

process (Chen *et al.*, 2007). The basic idea behind this technique is compatible with the above-discussed experiments made with DNA-functionalized AuNPs. Two basic experiments have been performed: (i) By wrapping oligonucleotides around SWCNTs, hybridization reactions with complementary oligonucleotides can be used for the reversible formation of SWCNT aggregates. Mixing of one type of conjugated SWCNTs with another type, conjugated with the complementary oligonucleotides, leads to multicomponent nanocomposites. (ii) In the first process step, thiolated DNA single strands were linked to AuNPs. Subsequently, these AuNPs were mixed with a solution of SWCNTs conjugated with the complementary DNA, which resulted in the formation of SWCNT–AuNP complexes by hybridization.

DNA-Based Protein Assemblies Covalent or noncovalent coupling facilitates the generation of synthetic DNA–protein conjugates (Niemeyer, 2002). This opens a wide range of opportunities for generating versatile molecular constructs for applications in life sciences and nanotechnology. The addressable assembly of DNA can be combined with the functionality of proteins. The addressability of DNA can be used in such constructs for controlled site-specific deposition of peptides or proteins on material surfaces. Another option is the use of conjugated double-stranded DNA for sensitivity enhancement of protein-based sensors, as explained with an example below. Several successful applications have been reported: self-assembly of high-affinity reagents for immunoassays, fabrication of laterally microstructured protein chips, design of bienzymatic complexes and biometallic aggregates, and DNA-directed immobilization (DDI) of peptides or proteins at implants for controlled cell adhesion (Niemeyer, 2002). Various advanced techniques are available for *covalent conjugation of oligodeoxyribonucleotides* (ODNs) to proteins or peptides. Amino groups or thiol groups can be used for covalent coupling of the ODNs with amino acids. In Figure 1.82, an example is given for the conjugation of an *aminopropylated ODN with a short hexapeptide* GRGDSP mediated by disuccinimidyl tartrate (DST) (for application see the following example for improvement of bone cell interaction with titanium implants in Figure 1.85).

Similarly, *thiol-modified ODNs* can be bound with the *heterospecific cross-linker sulfosuccinimidyl 4-[p-maleimidophenyl]butyrate* (sSMPB) to the protein (Niemeyer and Mirkin, 2004). Another approach is based on the conjugation of a recombinant protein containing a *C-terminal thioester* that is selectively bound to *cysteine conjugates of nucleic acids* (Tomkins *et al.*, 2001). In Figure 1.83, two examples are given for immunoassay applications. An antibody is coupled to DNA oligomers. Covalent conjugates of double-stranded DNA fragments and immunoglobulin (IgG) molecules are used for the detection of antigens. The detection signal of the antigen–antibody interaction can be enhanced by subsequent polymerase chain reaction multiplying the coupled DNA oligomer. Thus, the immuno-PCR (IPCR) increases the sensitivity about 1000-fold compared to the conventional enzyme-linked immunosorbent assay (Hendrickson *et al.*, 1995). The detection sensitivity for small-weight molecules, too, can be enhanced. Fluorescein has been chosen as a model analyte. The free analyte competes with a fluorescein–streptavidin–DNA conjugate. Short biotinylated DNA forms nanocircles bound to streptavidin. The nanocircles

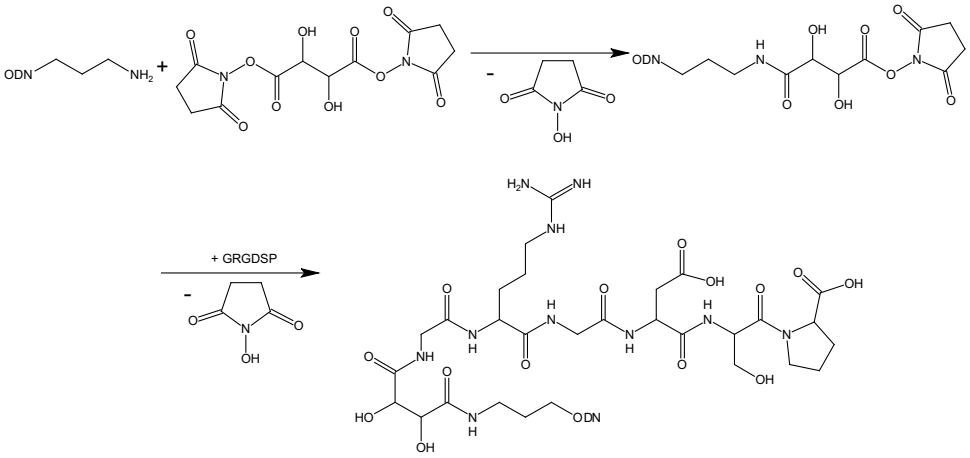

Figure 1.82 Conjugation reaction of aminopropylated ODN and GRGDSP mediated by disuccinimidyl tartrate.

can be functionalized by the coupling of biotinylated fluorescein. After competitive binding, the immobilized conjugate has been detected with PCR.

DNA–streptavidin conjugates have proven to be versatile constructs for the design of innovative nanostructures (Niemeyer, 2002), as indicated in Figure 1.84. Streptavidin covalently bound to *5′-thiol (SH)-modified oligonucleotide* serves as a unique building block. A single-stranded carrier nucleic acid with complementary sequences can act as a template for the formation of well-defined streptavidin aggregates. The biotin-binding sites of streptavidin allow the construction of various

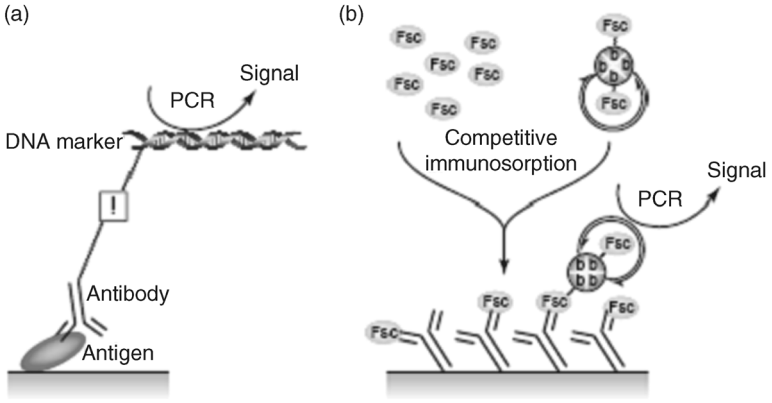

Figure 1.83 (a) Application of DNA–protein conjugates in immuno-PCR. The antigen is detected with a specific antibody that is coupled to a DNA fragment. PCR amplification leads to a high sensitivity of the antigen detection. The key of the experiment is a reliable chemical conjugation indicated by the square box. (b) Detection of small-weight molecules by competitive IPCR. Fluorescein (Fsc) is chosen as a model analyte. It competes with Fsc–streptavidin–DNA conjugates. The binding of the conjugates can be detected via PCR amplification. (Reprinted with permission from Niemeyer (2002). Copyright 2002, Elsevier.)

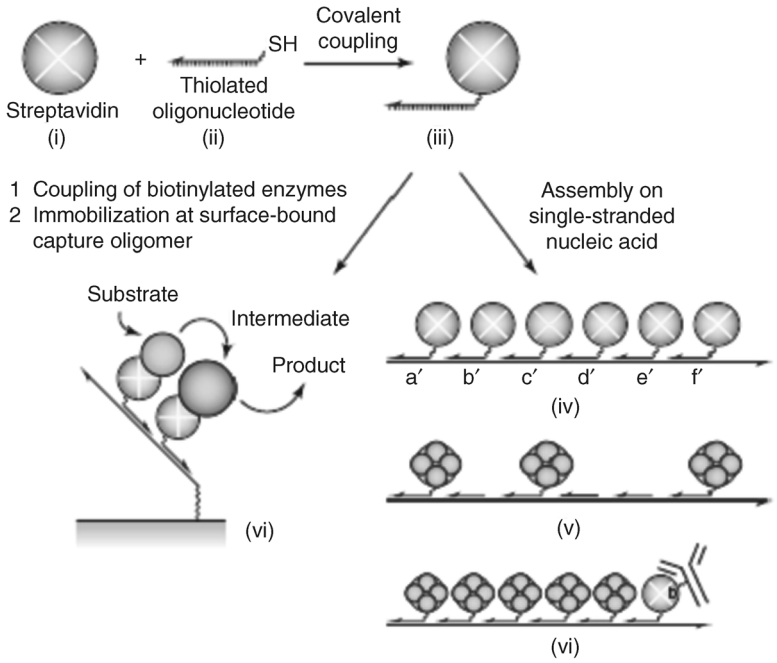

Figure 1.84 Synthesis of covalent DNA–streptavidin conjugates (iii) by covalent coupling of 5′-thiol (SH)-modified oligonucleotides (ii) and streptavidin (i). A set of conjugates (iii) self-assembles in the presence of a single-stranded nucleic acid with complementary sequence stretches (iv). Two examples are shown: fabrication of an antibody-containing metallic cluster chain (vi), and a bienzymatic functional complex (vi). (Reprinted with permission from Niemeyer (2002). Copyright 2002, Elsevier.)

supramolecular functionalities (Niemeyer *et al.*, 2002a). One example has been realized with the fabrication of a chain of gold particles grown by labeling the streptavidin with biotinylated 1.4 nm gold clusters. With a biotinylated immunoglobulin, coupled to the DNA–streptavidin conjugate, additionally incorporated into the chain, the whole construct can be considered as a promising nanoprobe for antigen detection. Another option is the close coupling of two enzymes enabling bienzymatic reactions (Niemeyer *et al.*, 2002b).

DNA–protein conjugates open also interesting options for the design of material interfaces capable of a controlled interaction with living cells, which is of high interest for implantology. Among the favored metallic implant materials in surgery are titanium and its alloys that exhibit good biocompatibility. High strength, good corrosion resistance *in vivo*, and toxicological harmlessness make them widely applied materials. Similar to other implant materials, however, difficulties may arise in cases of systemic diseases, such as diabetes and osteoporosis, or after radiation therapy. A material is needed that promotes the growth of new bone tissue near the implant interface. In such cases, bone tissue growth can be furthered by specific peptides promoting cell adhesion or directing cell proliferation or differentiation. Also, the immobilization of drug delivery units at the implant interface can be beneficial. When

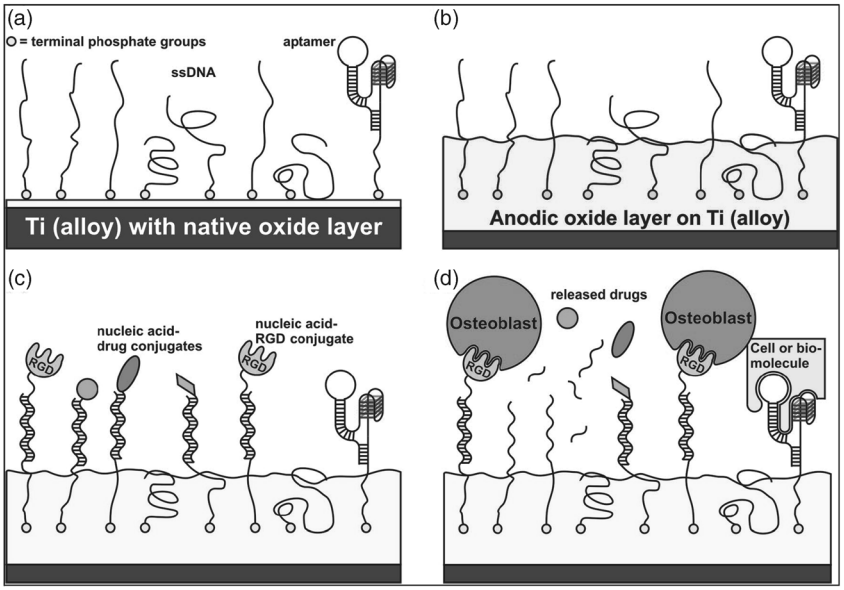

Figure 1.85 Four process steps of functionalization of titanium interfaces for improvement of cell interaction by means of oligonucleotide–protein conjugates. (a) Adsorption of single-stranded anchors of functional nucleic acids. (b) Anodic growth of a TiO_2 layer for partial entrapment of the biomolecules. (c) Hybridization of the nucleic acid conjugates to the anchor strands. (d) Specific binding of osteoblasts to RGD peptides. (Reprinted with permission from Michael *et al.* (2009). Copyright 2009, the American Chemical Society.)

such structures are to be integrated into the interface, care has to be taken that their biological functionalities are not destroyed by interaction with the metal. Degradation can be avoided by applying a coupling layer between peptide and metal surface. Oligonucleotide–peptide/protein conjugates are suitable for this purpose. In particular, this concept has been successfully applied for titanium alloys (Michael *et al.*, 2009). The whole process is subdivided into four steps (see also Figure 1.85):

a) Nucleic acid anchor strands (AS) or functional nucleic acids such as aptamers are adsorbed on the native oxide layer of the titanium implant.
b) The adsorbed nucleic acids are partially entrapped during subsequent anodic growth of a TiO_2 layer.
c) Fixed AS hybridize either with complementary strands (CS) conjugated to biomolecules (e.g., RGD peptides and growth factors) or drugs (e.g., antibiotics and antiphlogistics) or with functional nucleic acids. As an advantage, the technique can be adapted to the specific needs of the patient.
d) After implantation, specific tissue reactions are induced by the biomolecules (immobilized and/or released in a defined way).

The feasibility of this process has been demonstrated by adhesion experiments with bone-forming osteoblasts. As mentioned above, the hexapeptide GRGDSP was

chosen as the biologically active model substance because the sequence RGD is an adhesive motif in extracellular matrix proteins of bone cells. The adhesion of the osteoblasts on the conjugate-modified titanium surface is found to be stronger than that on the plain surface. Interestingly, this effect is observed already in the presence of the anchor oligonucleotides alone.

1.3.3 Protein-Based Nanotechnology

The design of hybrid nanomaterials based on proteins is even more challenging than the DNA technologies described above. This is due to the higher complexity of proteins at the level of the primary structure (20 amino acids versus 4 nucleotides) particularly at the level of secondary and tertiary structures that determine the protein function. Therefore, the immobilization strategy has to be selected very carefully, taking into account the given surface chemistry, the particular protein structure, and the intended application. Important issues are the *maintenance of the structural integrity to avoid denaturation*, the stable transfer of the *natural protein configuration*, and an *optimized spacing between the proteins*. Very often a *defined orientation at the interface* is required to ensure that the reactive sites needed for the intended function are exposed and hence accessible to external signals. Known immobilization routes can be classified into those for manufacturing two-dimensional or three-dimensional interfaces, and also into physical, chemical, and bioaffinity-mediated ones.

Physical Immobilization Several adhesive interactions are suitable for conjugation of proteins with a nonbiological material: electrostatic, hydrophobic/hydrophilic, and various kinds of polar interactions (Table 1.10). Usually they produce a random pattern of weakly bound proteins.

The simplest way of controlling the protein adsorption is by tuning of the electrostatic interaction. Plasma treatment of the solid substrate, polyelectrolyte coatings, adsorption of ions (e.g., Mg^{2+}, NH_2^+, and $(C_3H_5O(COO)_3^{3-})$), and pH control are potential options. Figure 1.86 shows an example for patterned

Table 1.10 Mechanisms of protein adsorption.

Interaction	Surface modification	Advantages	Drawbacks
Ionic bonds	Plasma activation, polyelectrolyte coating, tuned ion adsorption	Widespread applicability	Randomly oriented, heterogeneous, weak adsorption, nonspecific bonding, high background signals
Hydrophobic/ hydrophilic interaction	Self-assembled monolayers, lipid bilayers, hydrogels, BSA adsorption	Molecular designed tail groups	
Polar interaction	SAM		

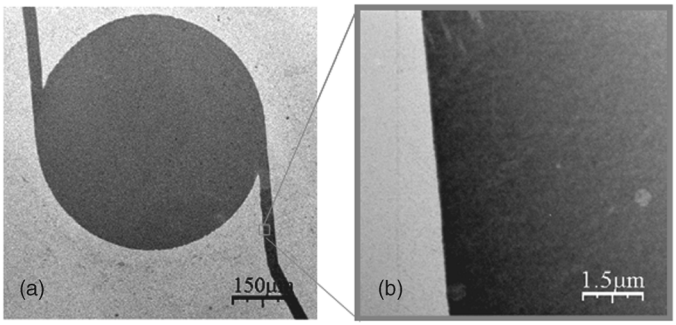

Figure 1.86 Scanning electron micrograph of a recrystallized protein layer (dark structure – bacterial surface protein of *Bacillus sphaericus* NCTC 9602) on a Si wafer. By using a PDMS stamp with an appropriate profile, the protein monomers can be physisorbed in the restricted reaction volume after preadsorption of Mg^{2+} ions. (a) Active probe region of a piezoelectric sensor; (b) the marked area shows the sharp boundary of the protein layer. (Reprinted with permission from Blüher (2008).)

functionalization of sensor surfaces by physisorption of proteins. Bacterial surface layer proteins served as templates for local metallization of probe regions. The adsorption on a silica surface was controlled by addition of Mg^{2+} ions. In a subsequent step, the protein layer acts as a template for the deposition of nanosized noble metal clusters (Pt or Pd) suitable for catalytic gas sensors (for more details see Section 7.3).

Layer-by-layer deposition of differentially charged polyelectrolytes allows the electrostatic interaction to be controlled. Hydrogels with charged surface groups, such as sulfate-modified dextrans or carboxymethyl cellulose, are suitable for adsorbing proteins. Self-assembled monolayers (SAMs) are known for their ability to control electrostatic, hydrophobic, and polar interactions (Mrksich and Whitesides, 1996). SAMs are formed spontaneously by exothermic interaction of the surface-active group with the substrate. Thiols and disulfides are commonly used as head groups on noble metal substrates such as gold, silver, and platinum, whereas silanes form the head groups on nonmetallic oxidic surfaces such as silica and titanium oxide. The side chains are usually alkyl chains or derivatized alkyl chains because they can form densely packed monolayers. The side chains are usually tilted with respect to the surface normal to maximize the van der Waals interactions between the molecules. The interaction of the SAMs with proteins can be tailored by a suitable choice of the tail group. Polar functional groups such as carboxylic acids and hydroxyls form hydrophilic interfaces, whereas nonpolar, organic groups such as methyl or trifluoromethyl form hydrophobic interfaces. The adsorption of proteins and the degree of denaturation correlate with the hydrophobicity of the surface of the SAM. Polyethylene glycol (PEG) has proven to be most suitable for avoiding protein adsorption. Therefore, biosensor surfaces that are to be protected against protein adsorption are often coated with alkanethiols terminated in short oligomers of ethylene glycol (e.g., $HS(CH_2)_{11}(OCH_2CH_2)_nOH$, $n = 2–7$). Another option is the preadsorption of a protein, for example, bovine serum albumin (BSA),

Table 1.11 Non-site-specific immobilization of proteins via covalent binding.

Interaction	Surface modification	Amino acids	Remarks
Amine chemistry ($-NH_2$)	Carboxylic acid, *N*-hydroxysuccinimide, aldehyde groups, epoxy	Lysine, hydroxylysine	Multipoint attachment, restricted conformational flexibility, heterogeneous, generally above pH 9
Thiol chemistry ($-SH$)	Maleimide, pyridyl disulfide, vinyl sulfone	Cysteine	Better orientation, pH 7–9.5
Carboxyl chemistry ($-COOH$)	Aminated SAM, carbodiimide	Aspartic acid, glutamic acid	Usually major fraction of surface groups
Epoxy chemistry ($-OH$)	Amino supported	Serine, threonine	

which precludes the adsorption of other proteins. Alternatively, there are also methods for covalent coupling of proteins to the SAM surface. Active tail groups that form amide or disulfide bonds are most suitable for this purpose. Application of mixed SAMs (protein adsorptive and adsorption resistant) offers the option of adsorbing proteins in a patterned manner. The weak binding and the random distribution of proteins are the major drawbacks of physical immobilization mechanisms for the formation of stable biointerfaces.

Chemical Immobilization Functional groups of amino acid side chains are possible binding sites for the chemical immobilization of proteins (see Tables 1.11 and 1.12).

Table 1.12 Site-specific immobilization of proteins via covalent binding.

Interaction	Surface modification	Protein	Remarks
Diels–Alder cycloaddition	Maleimide modified	Cyclopentadiene ligated	Reaction in water at room temperature, high rate
"Click" chemistry, 1,3–dipolar cycloaddition of azide and alkyne	Alkyne modified	Multipoint azide functionalized	High-density immobilization, simple process
α-Oxo semicarbazone ligation	Aldehyde groups	Semicarbazone ligated	
Peptide ligation	Ester glycoaldehyde, thioester	N-terminal cysteine, serine, histidine, threonine containing weak base nucleophiles	
Staudinger ligation	Phosphinothioester	Azido modified	pH 7.4–7.6 without noticeable side chain products

Very often the binding pattern is random as the binding can occur through many side chains of amino acids exposed on the exterior of the protein. In order to realize site-specific immobilization, a particular chemical nanostructuring of the substrate or additional functionalization of the protein is necessary. Site-specific immobilization is favored when the abundance of the functional amino acids exposed by the protein is very small (e.g., cysteine); ideally, the protein should exhibit only one reactive amino acid. Genetic modification of proteins can be a means for designing a suitable side group without affecting the protein function. Under such conditions, the protein can be deposited at a well-defined site with predictable orientation without affecting conformational stability. Various chemical methods can be used for immobilization, depending on the exposed amino acids (Rusmini *et al.*, 2007; Jonkheijm *et al.*, 2008; Goddard and Erickson, 2009). For non-site-specific immobilization, the available functional side groups are given in Table 1.11, and for site-specific covalent immobilization in Table 1.12.

Bioaffinity Immobilization The immobilization of proteins by means of biochemical affinity reactions is the favored method when the functionality of the protein is to be preserved. It is also advantageous when gentle detachment of a protein or regeneration of a protein coating under near-line processing conditions is intended. As these methods make use of molecular recognition structures, we will discuss the various options later in Chapter 2.

Biofunctionalized Nanoparticles: Artificial Proteins The large interest in medical and biological application of nanoparticles is partially due to the fact that the tunable size can be well adapted to the sizes of the various molecular and subcellular targets. There are two major areas of nanoparticle application in biology: bioimaging and nanotherapy. Bioimaging concerns targeted optical contrast enhancement, fluorescence imaging, nanosized magnetic resonance imaging (MRI), and locally enhanced spectroscopy (e.g., particle-enhanced Raman spectroscopy). The development of nanotherapy is aimed at administering the therapeutic formulations with high precision to the malignant cell. This is important in view of the fact that in current cancer therapy only 10–100 ppm of intravenously administered monoclonal antibodies reach their targets *in vivo*. This may be improved by a therapeutic means that overcomes the biological barriers on the path to the target. Moreover, the delivery has to be highly selective in order to minimize collateral damage to the tissues. Obviously, multifunctionality of nanoparticles would be highly desirable in nanotherapy. An "ideal" nanoparticle should carry one or more therapeutic agents, permeate biological barriers, avoid uptake by macrophages, target selectively subcellular objects, and deliver the therapeutics in a controlled way after reaching the target. This means that multifunctional nanoparticles should be carrier, sensor, and actor in one. A related design concept, intended for advanced cancer therapy, has been proposed by Ferrari (2005).

The manufacturing of multifunctional nanoparticles ought to be done in a stepwise process starting from a colloidal solution, as proposed by Moyano and Rotello (2011). The nanoparticle is made to surround itself with a polymeric or biochemical shell

resulting in a noninteracting core–shell structure. The shell can be functionalized with specific functional groups adapted to a particular biosystem under consideration. Typically, the core nanoparticles are stabilized by surface charges (electrostatic stabilization) or by short polymers (sterical stabilization) (Hunter, 1992). This initial stabilization can interfere with the subsequent step of the formation of the shell. A sufficiently stable and reproducible shell may be obtained by stable chemisorption of linker molecules. Favored molecules are structures that allow the presentation of addressable functional groups in high regularity. The shell is usually formed with short alkyl-based monolayers with specific functional tail groups. However, as the hydrophobic interior of alkyl-based monolayers can result in protein denaturation, oligo- or polyethylene glycol layers (OEG or PEG, respectively) are often applied. Moyano and Rotello (2011) have proven that an optimized shell structure can be obtained by combining an inner shell of alkyl chains with a thin outer shell of OEG. The inner hydrophobic shell serves as a stable linkage to the core whereas the outer shell provides a noninteracting surface. An outer layer consisting of four ethylene glycol repeats has turned out to be optimal. Structures of this type have been successfully prepared with CdSe quantum dots (3.2 nm core diameter) as well as Au core particles (2 nm diameter) (Figure 1.87). The hydrophobic part of the shell was formed by an alkanethiol-based monolayer.

Core–shell constructs have been tested as carriers for a model enzyme, the protease chymotrypsin (ChT). The positively charged enzyme denatures if the core is

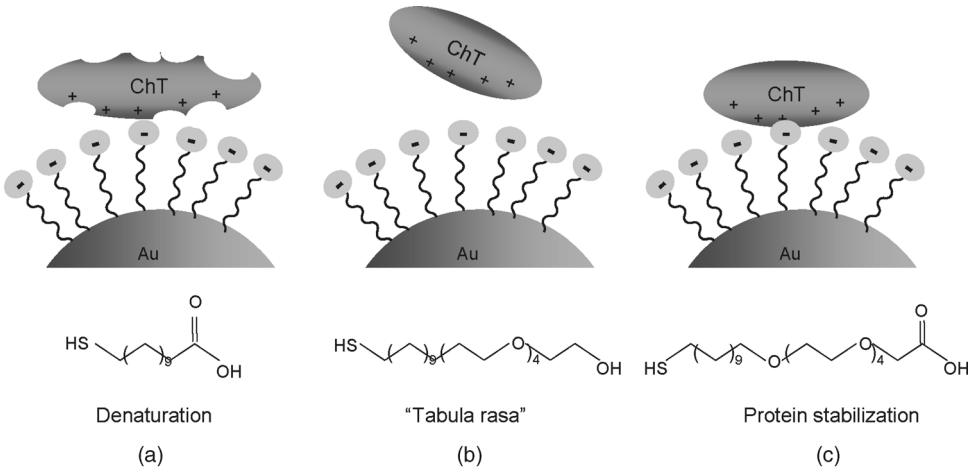

Figure 1.87 Generic approach to a hybrid core–shell structure of biofunctionalized nanoparticles with tailored interaction with proteins. In this example, a positively charged protein (ChT) is considered. (a) Simple alkanethiol-based monolayer results in protein denaturation. (b) TEG-functionalized particles are noninteracting. (c) Termination of the TEG layer with carboxylate groups results in reversible binding of the protein. (Adapted with permission from Moyano and Rotello (2011). Copyright 2011, the American Chemical Society.)

functionalized only with the alkanethiol monolayer (e.g., mercaptoundecanoic acid). By adding an additional outer shell of tetraethylene glycol (TEG) segments, a noninteracting "tabula rasa" structure is formed. The termination of the TEG layer with carboxylate groups leads to reversible binding of the ChT to the nanoparticles functionalized with the carboxylated TEG layer (NP–TCOOH). The enzyme is stabilized with full functionality. The stabilization of ChT at the NP–TCOOH structure leads to an essential increase of the substrate selectivity of the enzyme. Free ChT is a promiscuous enzyme hydrolyzing anionic, neutral, and cationic proteins. Owing to the negatively charged surface of the carrier nanoparticle NP–TCOOH, anionic substrates are repelled, whereas cationic substrates are attracted. This leads to an accelerated hydrolysis of the cationic substrates and a retarded reaction with the anionic ones (Moyano and Rotello, 2011). As mentioned above, the established platform allows systematic variation of the functional groups of the outer shell of the NP–TCOOH complex. For the majority of applications, the conjugation of the core–shell NP with a protein is mediated by noncovalent linkage in order to avoid any irreversible structure changes of the protein. This is usually realized with a tailored content of hydrophobic/hydrophilic and electrostatic interactions between the shell and the targeted protein. By adding specific amino acids to the terminal group in a controlled way, the degree of hydrophobicity can be varied. Alternatively, also bioaffine linkers can be incorporated into the shell. With the tailored linkage of amino acids to terminal groups of the shell structure, protein–protein interactions can be mimicked in a systematic way. The core–shell nanoparticle can be regarded as an "artificial protein" with tunable functional properties.

Core particles consisting of gold provide interesting options for the design of optical biosensors. The concept of a fluorescence assay suitable as a "chemical nose" is pictured in Figure 1.88. In this example, the sensor is based on the competitive binding of a fluorescent anionic polymer (e.g., poly(*p*-phenylene ethynylene) (PPE)) or the anionic green fluorescent protein (GFP with p*I* 5.92) and four analytes (A, B, C, and D) to cationic gold NP–TNH_2^+R complexes. The cationic tail groups are additionally functionalized with different short terminal groups making a "chemical nose" sensor array. (The six different $R_1, \ldots, R_6$ result in the six sensing systems $S_1, \ldots, S_6$.) The fluorescence of PPE (or GFP) is quenched when PPE (or GFP) is bound at the gold complex and is switched on when PPE (or GFP) is released. Depending on the size of terminal group R_i, the extent of quenching for a given bound fluorescent anion varies among the sensing systems. The evaluation of the patterns of fluorescence response of the sensing systems $S_1, \ldots, S_6$ for known concentrations of the individual proteins (A, B, C, and D) provides the information for identification of proteins in mixtures with unknown composition.

Tasks T1

Task 1.1: Calculate the strain u of a semiflexible elastic polymer chain loaded with a tensile force f in thermal equilibrium. Which condition has to be fulfilled in order that the polymer can be described as inextensible rod? Consider a polymer chain

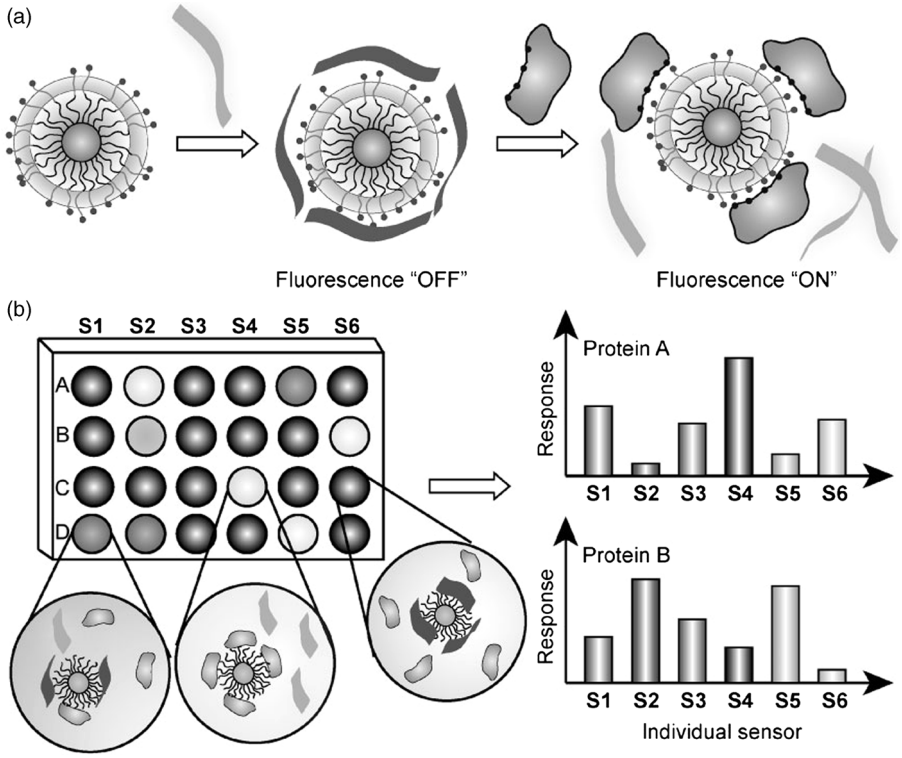

Figure 1.88 Schematic drawing of a "chemical nose" sensor array based on nanoparticles and fluorescence assay. (a) The competitive binding between protein and quenched PPE or GFP leads to the fluorescence light-up. (b) The combination of an sensor array generates fingerprint response patterns for individual proteins. (Reproduced with permission from De, Ghosh, and Rotello (2008). Copyright 2008, Wiley-VCH Verlag GmbH.)

with Young's modulus of 1 GPa and circular cross section. Estimate its minimum diameter so that this condition is fulfilled at tensile loads of up to $f = 10\,\mathrm{pN}$ under the assumption that the coupling between strain u and twist density ω can be neglected in the balance of the total elastic energy.

Task 1.2: Calculate the elastic energy stored in a short bent DNA segment of length l_0 when the radius of curvature equals a constant value R along the segment.

Task 1.3: Calculate the Young's moduli of the four biopolymers listed in Table 1.6 by using the experimentally determined values of the bend persistence length A and a continuum approximation for the second moment of inertia I of the polymer chains. From Eq. (1.5) second moments of inertia are obtained for the different filament geometries as summarized in Figure 1.89. Note that the actin filament forms a helical fiber with an elliptical cross section.

Task 1.4: Calculate the coil diameter of λ-DNA in thermal equilibrium. λ-DNA consists of 48 502 base pairs.

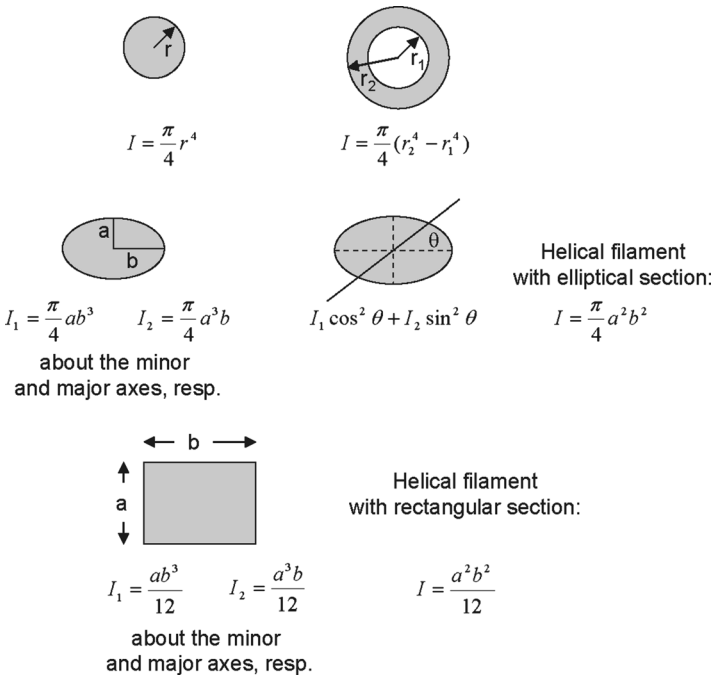

Figure 1.89 Second moments of inertia *I* of filaments. (Adapted from Howard (2001).)

Task 1.5: How long has an uncatalyzed first-order reaction to run in order that 1% of a substrate is transformed? For the activation energies of the uncatalyzed reaction ΔG_{uncat}, we assume values between 80 and 100 kJ/mol.

References

Aich, P., Labiuk, S.L. *et al.* (1999) M-DNA: a complex between divalent metal ions and DNA which behaves as a molecular wire. *Journal of Molecular Biology*, **294** (2), 477–485.

Aldaye, F.A. and Sleiman, H.F. (2007) Modular access to structurally switchable 3D discrete DNA assemblies. *Journal of the American Chemical Society*, **129** (44), 13376–13377.

Alivisatos, A.P., Johnsson, K.P. *et al.* (1996) Organization of 'nanocrystal molecules' using DNA. *Nature*, **382** (6592), 609–611.

Banavar, J.R., Hoang, T.X. *et al.* (2004) Unified perspective on proteins: a physics approach. *Physical Review E: Statistical, Nonlinear, and Soft Matter Physics*, **70** (4 Pt 1), 041905.

Benke, A. (2007) Aufbau nanoskopischer Netzwerke aus DNA und Bindeproteinen. Ph.D. thesis, Technische Universität Dresden.

Benke, A., Mertig, M. *et al.* (2011) pH- and salt-dependent molecular combing of DNA: experiments and phenomenological model. *Nanotechnology*, **22** (3), 035304.

Berti, L., Alessandrini, A. *et al.* (2005) DNA-templated photoinduced silver deposition. *Journal of the American Chemical Society*, **127** (32), 11216–11217.

Blüher, A. (2008) S-Schichtproteine als molekulare Bausteine zur Funktionalisierung mikroelektronischer Sensorstrukturen. Ph.D. thesis, Technische Universität Dresden.

Bockelmann, U., Thomen, P. *et al.* (2002) Unzipping DNA with optical tweezers: high sequence sensitivity and force flips. *Biophysical Journal*, **82** (3), 1537–1553.

Bosaeus, N., El-Sagheer, A.H. *et al.* (2012) Tension induces a base-paired overstretched DNA conformation. *Proceedings of the National Academy of Sciences of the United States of America*, **109** (38), 15179–15184.

Braun, E., Eichen, Y. *et al.* (1998) DNA-templated assembly and electrode attachment of a conducting silver wire. *Nature*, **391** (6669), 775–778.

Brochard-Wyart, F. (1995) Polymer chains under strong flows: Stem and flowers. *Europhysics Letters*, **30** (7), 387.

Bustamante, C., Marko, J.F. *et al.* (1994) Entropic elasticity of lambda-phage DNA. *Science*, **265** (5178), 1599–1600.

Cao, Y.C., Jin, R. *et al.* (2002) Nanoparticles with Raman spectroscopic fingerprints for DNA and RNA detection. *Science*, **297** (5586), 1536–1540.

Chen, J.H. and Seeman, N.C. (1991) Synthesis from DNA of a molecule with the connectivity of a cube. *Nature*, **350** (6319), 631–633.

Chen, Y., Liu, H., Ye, T., Kim, J., and Mao, C. (2007) DNA-directed assembly of single-wall carbon nanotubes. *Journal of the American Chemical Society*, **129** (28), 8696–8697.

Clausen-Schaumann, H., Rief, M. *et al.* (2000) Mechanical stability of single DNA molecules. *Biophysical Journal*, **78** (4), 1997–2007.

Cluzel, P., Lebrun, A. *et al.* (1996) DNA: an extensible molecule. *Science*, **271** (5250), 792–794.

Coffer, L., Bigham, S., and Li, X. (1996) Dictation of the shape of mesoscale semiconductor nanoparticle assemblies by plasmid DNA. *Applied Physics Letters*, **69** (25), 3851.

Colombi Ciacchi, L.C. (2002) Growth of platinum clusters in solution and on biopolymers: the microscopic mechanisms. Ph.D. thesis, Technische Universität Dresden.

De, M., Ghosh, P.S., and Rotello, V.M. (2008) Applications of nanoparticles in biology. *Advanced Materials*, **20**, 4225–4241.

Douglas, S.M., Bachelet, I., and Church, G. M. (2012) A logic-gated nanorobot for targeted transport of molecular payloads. *Science*, **335**, 831–834.

Douglas, T. and Young, M. (1999) Virus particles as templates for materials synthesis. *Advanced Materials*, **11** (8), 679–681.

Erler, C. (2010) Synthesis of metallic nanowires using integrated DNA molecules as templates. Ph.D. thesis, Technische Universität Dresden.

Erler, C., Guenther, K., and Mertig, M. (2009) Photo-induced synthesis of DNA-templated metallic nanowires and their integration into micro-fabricated contact arrays. *Applied Surface Science*, **255**, 9647–9651.

Ferrari, M. (2005) Cancer nanotechnology: opportunities and challenges. *Nature Reviews. Cancer*, **5**, 161–171.

Festag, G., Klenz, U., Henkel, T., Csáki, A., and Fritzsche, W. (2005) Biofunctionalization of metallic nanoparticles and microarrays for biomolecular detection, in *Biofunctionalization of Nanomaterials* (ed. C. Kumar), Wiley-VCH Verlag GmbH, Weinheim.

Freeman, R., Finder, T. *et al.* (2009) Multiplexed analysis of Hg^{2+} and Ag^{+} ions by nucleic acid functionalized CdSe/ZnS quantum dots and their use for logic gate operations. *Angewandte Chemie – International Edition*, **48** (42), 7818–7821.

Goddard, J.M. and Erickson, D. (2009) Bioconjugation techniques for microfluidic biosensors. *Analytical and Bioanalytical Chemistry*, **394** (2), 469–479.

Günther, K., Mertig, M. *et al.* (2010) Mechanical and structural properties of YOYO-1 complexed DNA. *Nucleic Acids Research*, **38** (19), 6526–6532.

Guo, X., Gorodetsky, A.A. *et al.* (2008) Conductivity of a single DNA duplex bridging a carbon nanotube gap. *Nature Nanotechnology*, **3** (3), 163–167.

Haldane, J.B.S. (1930) *Enzymes*, MIT Press edition 1965; ISBN 0-262-58003-9.

Harnack, O., Ford, W.E., Yasuda, A., and Wessels, J.M. (2002) Tris(hydroxymethyl) phosphine-capped gold particles templated by DNA as nanowire precursors. *Nano Letters*, **2** (9), 919.

He, Y., Ye, T. *et al.* (2008) Hierarchical self-assembly of DNA into symmetric supramolecular polyhedra. *Nature*, **452** (7184), 198–201.

Hendrickson, E.R., Truby, T.M. *et al.* (1995) High sensitivity multianalyte immunoassay using covalent DNA-labeled antibodies and polymerase chain reaction. *Nucleic Acids Research*, **23** (3), 522–529.

Hoang, T., Trovato, A., Seno, F., Banavar, J.R., and Maritan, A. (2006) Marginal compactness of protein native structures. *Journal of Physics: Condensed Matter*, **18**, S297–S306.

Howard, J. (2001) *Mechanics of Motor Proteins and the Cytoskeleton*, Sinauer Associates, Inc. Publishers, Sunderland, MA.

Hunter, R.J. (1992) *Foundations of Colloidal Science*, vol. **1**, Clarendon Press, Oxford.

Jin, R.C., Wu, G.S. *et al.* (2003) What controls the melting properties of DNA-linked gold nanoparticle assemblies? *Journal of the American Chemical Society*, **125** (6), 1643–1654.

Jonkheijm, P., Weinrich, D. *et al.* (2008) Chemical strategies for generating protein biochips. *Angewandte Chemie – International Edition*, **47** (50), 9618–9647.

Kauert, D.J., Kurth, T. *et al.* (2011) Direct mechanical measurements reveal the material properties of three-dimensional DNA origami. *Nano Letters*, **11** (12), 5558–5563.

Keren, K., Berman, R.S., and Braun, E. (2004) Patterned DNA metallization by sequence-specific localization of a reducing agent. *Nano Letters*, **4** (2), 323–326.

Keren, K., Krueger, M. *et al.* (2002) Sequence-specific molecular lithography on single DNA molecules. *Science*, **297** (5578), 72–75.

Knez, M., Sumser, M., Bittner, A.M., Wege, Ch., Jeske, H., Martin, T.P., and Kern, K. (2004) Spatially selective nucleation of metal clusters on the tobacco mosaic virus. *Advanced Functional Materials*, **14**, 116–124.

Kuklenyik, Z. and Marzilli, L.G. (1996) Mercury(II) site-selective binding to a DNA hairpin. Relationship of sequence-dependent intra- and interstrand cross-linking to the hairpin–duplex conformational transition. *Inorganic Chemistry*, **35** (19), 5654–5662.

Kumar, A., Pattarkine, M., Bhadbhade, M., Mandale, A.B., Ganesh, K.N., Datar, S.S., Dharmadhikari, C.V., and Sastry, M. (2001) Linear superclusters of colloidal gold particles by electrostatic assembly on DNA templates. *Advanced Materials*, **13** (5), 341–344.

Lakatos, M. (2013) Aufbau colorimetrischer Sensoren mit Goldnanopartikeln für unterschiedliche Analytgrößen. Ph.D. thesis, Technische Universität Dresden.

Lee, J.S., Latimer, L.J. *et al.* (1993) A cooperative conformational change in duplex DNA induced by Zn^{2+} and other divalent metal ions. *Biochemistry and Cell Biology*, **71** (3–4), 162–168.

Lemanov, V.V. (2000) Piezoelectric and pyroelectric properties of protein amino acids as basic materials of soft state physics. *Ferroelectrics*, **238** (1), 211–218.

Lezon, T.R., Banavar, J.R., and Maritan, A. (2006) The origami of life. *Journal of Physics: Condensed Matter*, **18**, 847–888.

Lippert, B. (ed.) (1999) *Cisplatin: Chemistry and Biochemistry of a Leading Anticancer Drug*, Wiley-VCH Verlag GmbH, Weinheim.

Liu, D., Park, S.H. *et al.* (2004) DNA nanotubes self-assembled from triple-crossover tiles as templates for conductive nanowires. *Proceedings of the National Academy of Sciences of the United States of America*, **101** (3), 717–722.

Liu, H., Chen, Y., He, Y., Ribbe, A.E., and Mao, Ch. (2006) Approaching the limit: can one DNA oligonucleotide assemble into large nanostructures? *Angewandte Chemie – International Edition*, **45**, 1942–1945.

Liu, J. and Lu, Y. (2006) Fast colorimetric sensing of adenosine and cocaine based on a general sensor design involving aptamers and nanoparticles. *Angewandte Chemie – International Edition*, **45**, 90–94.

Liu, Y., Lin, C., Li, H., and Yan, H. (2005) Aptamer-directed self-assembly of protein arrays on a DNA nanostructure. *Angewandte Chemie – International Edition*, **44** (28), 4333.

Marko, J.F. and Siggia, E.D. (1995) Stretching DNA. *Macromolecules*, **28**, 8759–8770.

Mertig, M., Ciacchi, L.C., Seidel, R., Pompe, W., and De Vita, A. (2002) DNA as a selective metallization template. *Nano Letters*, **2**, 841–844.

Mertig, M. and Pompe, W. (2004) Biomimetic fabrication of DNA-based metallic nanowires and networks, in *Nanobiotechnology* (eds C. Niemeyer and Ch. Mirkin), Wiley-VCH Verlag GmbH, Weinheim.

Michael, J., Schönzart, L. *et al.* (2009) Oligonucleotide–RGD peptide conjugates for surface modification of titanium implants and improvement of osteoblast adhesion. *Bioconjugate Chemistry*, **20** (4), 710–718.

Mirkin, C.A., Letsinger, R.L. *et al.* (1996) A DNA-based method for rationally assembling nanoparticles into macroscopic materials. *Nature*, **382** (6592), 607–609.

Moyano, D.F. and Rotello, V.M. (2011) Nano meets biology: structure and function at the nanoparticle interface. *Langmuir*, **27** (17), 10376–10385.

Mrksich, M. and Whitesides, G.M. (1996) Using self-assembled monolayers to understand the interactions of man-made surfaces with proteins and cells. *Annual Review of Biophysics and Biomolecular Structure*, **25**, 55–78.

Nam, J.M., Park, S.J. *et al.* (2002) Bio-barcodes based on oligonucleotide-modified nanoparticles. *Journal of the American Chemical Society*, **124** (15), 3820–3821.

Nam, J.M., Stoeva, S.I. *et al.* (2004) Bio-bar-code-based DNA detection with PCR-like sensitivity. *Journal of the American Chemical Society*, **126** (19), 5932–5933.

Nelson, D.L. and Cox, M.M. (2008) *Lehninger – Principles of Biochemistry*, W. H. Freeman and Company, New York.

Nelson, P. (ed.) (2008) *Biological Physics – Energy, Information, Life*, W.H. Freeman and Company, New York.

Niemeyer, C.M. (2002) The development of semisynthetic DNA–protein conjugates. *Trends in Biotechnology*, **20** (9), 395–401.

Niemeyer, C.M., Adler, M. *et al.* (2002a) Supramolecular DNA–streptavidin nanocircles with a covalently attached oligonucleotide moiety. *Journal of Biomolecular Structure and Dynamics*, **20** (2), 223–230.

Niemeyer, C.M., Koehler, J. *et al.* (2002b) DNA-directed assembly of bienzymic complexes from *in vivo* biotinylated NAD(P)H:FMN oxidoreductase and luciferase. *ChemBioChem: A European Journal of Chemical Biology*, **3** (2–3), 242–245.

Niemeyer, C.M. and Mirkin, C.A. (eds) (2004) *Nanobiotechnology*, Wiley-VCH Verlag GmbH, Weinheim.

Odijk, T. (1995) Stiff chains and filaments under tension. *Macromolecules*, **28**, 7016–7018.

Park, S.J., Taton, T.A. *et al.* (2002) Array-based electrical detection of DNA with nanoparticle probes. *Science*, **295** (5559), 1503–1506.

Patolsky, F., Weizmann, Y. *et al.* (2002) Au-nanoparticle nanowires based on DNA and polylysine templates. *Angewandte Chemie – International Edition*, **41** (13), 2323–2327.

Pauling, L. and Corey, R.B. (1951) Configurations of polypeptide chains with favored orientations around single bonds: two new pleated sheets. *Proceedings of the National Academy of Sciences of the United States of America*, **37** (11), 729–740.

Rakitin, A., Aich, P. *et al.* (2001) Metallic conduction through engineered DNA: DNA nanoelectronic building blocks. *Physical Review Letters*, **86** (16), 3670–3673.

Richter, J., Mertig, M., Pompe, W., and Vinzelberg, H. (2002) Low-temperature resistance of DNA-templated nanowires. *Applied Physics A*, **74** (6), 725.

Rosi, N.L. and Mirkin, C.A. (2005) Nanostructures in biodiagnostics. *Chemical Reviews*, **105** (4), 1547–1562.

Rothemund, P.W. (2006) Folding DNA to create nanoscale shapes and patterns. *Nature*, **440** (7082), 297–302.

Roy, S., Vedala, H. *et al.* (2008) Direct electrical measurements on

single-molecule genomic DNA using single-walled carbon nanotubes. *Nano Letters*, **8** (1), 26–30.
Rusmini, F., Zhong, Z. *et al.* (2007) Protein immobilization strategies for protein biochips. *Biomacromolecules*, **8** (6), 1775–1789.
Sastry, M., Kumar, A., Datar, S., Dharmadhikari, C.V., and Ganesh, K.N. (2001) DNA-mediated electrostatic assembly of gold nanoparticles into linear arrays by simple drop-coating procedure. *Applied Physics Letters*, **78** (19), 2943.
Scholtz, J.M., Qian, H. *et al.* (1991) Parameters of helix–coil transition theory for alanine-based peptides of varying chain lengths in water. *Biopolymers*, **31** (13), 1463–1470.
Seeman, N.C. (1982) Nucleic acid junctions and lattices. *Journal of Theoretical Biology*, **99** (2), 237–247.
Seeman, N.C. (2003) DNA in a material world. *Nature*, **421**, 427–431.
Seeman, N.C. and Belcher, A.M. (2002) Emulating biology: building nanostructures from the bottom up. *Proceedings of the National Academy of Sciences of the United States of America*, **99** (Suppl. 2), 6451–6455.
Seidel, R., Ciacchi, L.C. *et al.* (2004) Synthesis of platinum cluster chains on DNA templates: conditions for a template-controlled cluster growth. *Journal of Physical Chemistry B*, **108** (30), 10801–10811.
Seidel, R., Mertig, M., and Pompe, W. (2002) Scanning force microscopy of DNA metallization. *Surface and Interface Analysis*, **33**, 151–154.
Shih, W.M., Quispe, J.D. *et al.* (2004) A 1.7-kilobase single-stranded DNA that folds into a nanoscale octahedron. *Nature*, **427** (6975), 618–621.
Smith, S.B., Cui, Y. *et al.* (1996) Overstretching B-DNA: the elastic response of individual double-stranded and single-stranded DNA molecules. *Science*, **271** (5250), 795–799.
Smith, S.B., Finzi, L. *et al.* (1992) Direct mechanical measurements of the elasticity of single DNA molecules by using magnetic beads. *Science*, **258** (5085), 1122–1126.
Tanaka, K., Clever, G.H. *et al.* (2006) Programmable self-assembly of metal ions inside artificial DNA duplexes. *Nature Nanotechnology*, **1** (3), 190–194.
Taton, T.A., Mirkin, C.A. *et al.* (2000) Scanometric DNA array detection with nanoparticle probes. *Science*, **289** (5485), 1757–1760.
Thaxton, C.S. and Mirkin, C.A. (2004) DNA–gold nanoparticle conjugates, in *Nanobiotechnology* (eds C.M. Niemeyer and C.A. Mirkin), Wiley-VCH Verlag GmbH, Weinheim.
Tomkins, J.M., Nabbs, B.K. *et al.* (2001) Preparation of symmetrical and unsymmetrical DNA–protein conjugates with DNA as a molecular scaffold. *ChemBioChem: A European Journal of Chemical Biology*, **2** (5), 375–378.
Wang, M.D., Yin, H. *et al.* (1997) Stretching DNA with optical tweezers. *Biophysical Journal*, **72** (3), 1335–1346.
Watson, J.D. and Crick, F.H. (1953) Molecular structure of nucleic acids: a structure for deoxyribose nucleic acid. *Nature*, **171** (4356), 737–738.
Wirtz, D. (1995) Direct measurement of the transport properties of a single DNA molecule. *Physical Review Letters*, **75** (12), 2436–2439.
Yoo, K.H., Ha, D.H. *et al.* (2001) Electrical conduction through poly (dA)–poly(dT) and poly(dG)–poly(dC) DNA molecules. *Physical Review Letters*, **87** (19), 198102.
Zhang, Y. and Seeman, N.C. (1994) Construction of a DNA-truncated octahedron. *Journal of the American Chemical Society*, **116** (5), 1661.
Zheng, M., Jagota, A. *et al.* (2003) Structure-based carbon nanotube sorting by sequence-dependent DNA assembly. *Science*, **302** (5650), 1545–1548.
Zimmermann, R., Freudenberg, U., Schweiß, R., Küttner, D., and Werner, C. (2010) Hydroxide and hydronium ion adsorption – a survey. *Current Opinion in Colloid & Interface Science*, **15**, 196–202.